Electronic Spectroscopy

of some

Metal-Containing Free-Radicals

Thesis submitted for the degree of

Doctor of Philosophy

at the University of Leicester

by

Simon Jonathan Pooley B.Sc. (Leicester)

Department of Chemistry

University of Leicester

October 1998

ProQuest LLC
789 East Eisenhower Parkway
P.O. Box 1346
Ann Arbor, MI 48106-1346

TITLE **Electronic spectroscopy of some metal-containing free-radicals**

AUTHOR **Simon Pooley**

ABSTRACT

Laser-induced fluorescence (LIF) spectroscopy has been used to probe the properties of some metal-containing free-radicals. These radicals were formed using three different techniques; fragmentation through electric discharge, laser ablation and laser photolysis and were studied in a supersonic jet expansion.

A dispersed fluorescence spectroscopic study of the zinc-monoethyl free radical was performed. From this work vibrational frequencies, particularly of the Zn-C stretching and the Zn-C-C bending modes, have determined for both the $\tilde{X}$ and $\tilde{A}$ states. In addition several peaks in the excitation spectrum reported by Povey *et al.* (22500-24000 cm^{-1}) have been assigned.

Recently Professor T.A. Miller and co-workers at Ohio State University recorded rotationally-resolved LIF spectra of ZnC_2H_5 in the 22500-23100 cm^{-1} region. This study complemented the dispersed fluorescence work described above, so the author was asked to generate a model and interpret this spectra.

A Hamiltonian model to simulate rotational structure of asymmetric top molecules which includes spin-rotation terms has been written by the author to form part of a spectral simulation program. This program was used to simulate the rotationally resolved LIF spectra of ZnC_2H_5 detailed above. Unfortunately a complete analysis has not been possible but values for the *A*, *B*, and *C* rotational constants for many of the bands are presented here along with a analysis of the observed values of spin-rotation constants.

Finally, LIF spectra of a new electronic transition of BaOH, the $\tilde{D}^2\Sigma^+ - \tilde{X}^2\Sigma^+$ system has been observed. Also, the $\tilde{C} - \tilde{X}$ system was reinvestigated. The $\tilde{C} - \tilde{X}$ system is particularly interesting because it shows much more complexity than might be expected from previous studies. Vibrationally and partially rotationally resolved spectra are reported for both systems and the $\tilde{C} - \tilde{X}$ region offers some evidence that the molecule may be bent in the excited state with a large spin-rotation interaction coupling.

STATEMENT OF ORIGINALITY

The work presented in this thesis was carried out by the author in the Department of Chemistry of the University of Leicester during the period October 1994 and April 1998 and is original unless otherwise acknowledged in the text or references.

The work presented in Chapter 6 on BaOH was performed in conjunction with Mr Matthew Beardah. This aside, none of the work has been or will be submitted for another degree at this or any other university.

Signed S J Peeden Date 18/3/99

Contents page

Chapter One

Introduction

1.1 Introduction

The fundamental role of chemical intermediates has long been recognized in all areas of chemistry. However, until recently little work had been done to characterise these species. Their highly reactive nature and short life-times make them difficult compounds to study, often requiring specialized spectroscopic techniques, particularly to cope with low concentrations. Consequently, the development of highly sensitive gas-phase spectroscopic methods such as laser induced fluorescence (LIF) and resonance-enhanced multiphoton ionisation (REMPI) has had a dramatic effect of the characterisation of transient molecules.

Most of the early spectroscopic studies on the species were directed towards simple organic intermediates and summary of these can be found in reference 1. Metal-containing intermediates, with the exception of metal clusters, have been less well studied. This is a serious omission considering the important role metal containing intermediates play in a wide variety of processes.

1.2 Importance of metal containing intermediates

1.2.1 Catalysis

One of the more obvious places where metal-containing intermediates are likely to be encountered are in homogeneous and heterogeneous catalysis. The catalytic properties of many metals, particularly those of group 8, 9 and 10, are utilized in numerous industrial applications. A complete discussion of these is beyond the scope of this thesis. However, as an example huge quantities of ammonia are produced each year through the Haber process in which atmospheric nitrogen is combined with hydrogen over an iron catalyst. Iron-containing intermediates proved a lower energy pathway, thus playing an important role in making the Haber process economically feasible. Nature too profits from the catalytic properties of metals; magnesium can be found in chlorophyll and iron in haemoglobin.

1.2.2 Semiconductor deposition

Another large scale industrial application where metal containing intermediates play a crucial role is in the fabrication of semiconductors. Teal *et al.*[2] prepared the first semiconductor based photo-cells and rectifiers in 1947 and, like in most early semiconductors, they used silicon or germanium to build their devices from. In subsequent years, as the complexity of integrated electric circuits increased, the demand for better and more efficient materials has spiraled very rapidly. The first alternative semiconductor substrate used was GaAs, which could be more easily engineered, and devices made from it were considerably faster.

In recent years, there has been a considerable increase in the number of semiconducting materials available. Most of these materials are derived from elements from groups IIB, IIIB, VB, and VIB of the periodic table. Some common examples that are widely used include GaAs, InP, AlGaAs, ZnS, CdTe, and CdHgTe. Many books, such as reference 3, have been written on semiconductor growth so the reader is directed to these for an in depth discussion of growth processes, reactor design, etc. However, simple consideration of some of the processes involved in semiconductor growth is considered here.

The traditional route to semiconductor materials is through the thermal decomposition of suitable precursor molecules followed by the recombination of fragments. An example of one of these processes is the deposition of gallium arsenide:

$$Ga(CH_3)_{3(g)} + 3AsH_{3(g)} \xrightarrow{\Delta} GaAs_{(s)} + 3CH_{4(g)}. \qquad (1)$$

More recently sources other than heat, have been used to provide the energy necessary to decompose precursor molecules. One that is particularly relevant to the work described within this thesis is UV photolysis. It has been shown that light (often laser light) can induce deposition through localised heating of the substrate or more usefully through photolysis of precursors. The localised nature of both of these processes makes them, potentially very useful, allowing patterned films for electronic circuitary to be grown *in*

situ. Another advantage of photolysis is that the wavelength of light can be chosen (usually UV) so that selective bond homolysis takes place, thus limiting the number of reaction pathways, which is often a problem in semiconductor growth.

As most semiconductor deposition processes involve the decomposition of precursors followed by recombination the potential for unwanted by-products and, in particular, impurities in fabricated material, is large. For long-established materials such as GaAs, much work has been done on optimising temperature, pressure, flow rates and reactor designs[3] to minimise film impurities. However, little work has been carried out to characterise the mechanism through which deposition occurs. As this mechanism is expected to be complex, involving a number of possible reaction pathways and chemical intermediates, elucidation could lead to the development of improved precursor molecules.

Most of the research carried out up until now to investigate decomposition mechanisms has relied upon the analysis of the end products from simple decomposition reactions.[4,5] These studies provide useful clues on mechanisms but rarely provide any direct evidence. More confidence could be placed in a study in which a reaction intermediate is observed directly. Butler and co-workers adopted this approach to investigate the decomposition of the trimethyls of gallium, indium and aluminum.[6] They use IR diode laser spectroscopy to detect methyl radicals as the thermal decomposition proceeded. Methyl radicals were detected in the decomposition of $Ga(CH_3)_3$ and $In(CH_3)_3$ but not for $Al(CH_3)_3$; the absence of CH_3 radicals for $Al(CH_3)_3$ decomposition was attributed to a low methyl concentration rather than a different mechanism.

This example illustrates perfectly a prime problem in studying reaction intermediates, namely, the low concentrations of the species involved. As a result, a technique with very high detection sensitivity is desirable if one is to successfully observe a wide range of intermediates. As indicated, one technique with sufficient detection sensitivity (10^5-10^6 molecules/cm^3 being detectable under 'best case' conditions) is laser induced fluorescence (LIF) spectroscopy. However, LIF spectroscopy does have some

disadvantages, in that the target molecule must have an electronic transition at a wavelength that can easily be obtained by commercial available lasers; and the excited state must then fluoresce (or at least decay to a state that does) in order to be detected. Unfortunately, this is not the case for simple alkyl radicals such as methyl or ethyl. However, an alternative approach is to study the metal containing intermediate rather than the simple alkyl radicals. This approach has the advantage that it is known that some metal-containing intermediates can be detected by LIF.

1.2.3 Atmospheric Chemistry

In recent years the chemistry of the Earth's atmosphere has become of great interest due to concerns about stratospheric ozone depletion and 'the greenhouse effect'. The troposphere and stratosphere act as sinks for metal atoms from layers of metals in the upper atmosphere. Daily, 170 tonnes of a variety of metals enter the earth's atmosphere through meteoric ablation. The major metallic constituents of meteorites are magnesium (12.5%), iron (11.5%), aluminum (1.7%), nickel (1.5%), calcium (1.0%), and sodium (0.6%).[7] These metals are ablated by frictional heating and form thin layers of metal atoms in the mesosphere and thermosphere (80-110 km).

Currently, the chemistry of sodium layer has received most attention mainly because it is the easiest to monitor using the lidar technique.[8] In addition atomic sodium and sodium-oxygen intermediates play an important role in the Chapman cycle (equation 2).[9]

$$\begin{aligned} Na + O_3 &\rightarrow NaO + O_2 \\ NaO + O &\rightarrow Na(^2P, ^2S) + O_2 \end{aligned} \qquad (2)$$

Despite the apparent simplicity of the Chapman cycle, it is not fully understood and a tool (such as LIF) that could be used to monitor the concentration of NaO would be beneficial. As well their role in the chemistry of the Earth's atmosphere, metal-containing species have also been detected in the atmospheres of other planets in the solar system. As on Earth, these presumably arise from meteoric ablation.[10]

1.2.4 Interstellar medium (ISM) Chemistry

The observation of the magnesium-containing free-radical MgNC in the ISM[11-13] has provoked increased interest in laboratory-based studies of metal-containing species. The ISM is the vast expanse of space between stars. The very low density of molecules, coupled to the low temperatures provide ideal conditions for the survival of radical intermediates. The possibility of detecting many other metal-containing radicals is high and laboratory-based studies of these species could lead to a better understanding of the chemistry in the ISM.

1.2.5 Flames

The brightly coloured flames resulting from the inclusion of a metal salt, particularly alkaline earth metal salts, in combustion has been known for a very long time. Calcium (brick red), strontium (red) and barium (green) are the basis of many firework compositions and flares. Originally these colourations were though to be due to bands of the appropriate metal oxides, but James and Sugden[14] suggested that the monohydroxides, CaOH, SrOH and BaOH, were responsible. In addition, many of these species (particularly CaOH) are persistent impurities in the spectra of all flames and explosions and so they cannot be ignored when considering the chemistry of flames.

The study of these species goes back to the 1950's. As stated above James and Sugden[14] first suggested that the flame colours caused by alkaline earth metal salts was due to the metal monohydroxides. Shortly afterwards, studies using the isotope shifts caused by introducing deuterium confirmed this was the case. The interest in these molecules then waned slightly, and until quite recently little more was known about these species than that deduced from the early studies. Recently the development of new techniques has meant that these species can be studied outside of flames, and the groups of Harris and Bernath (see later in this chapter for detail), in particular have dramatically increased the understanding of the geometries and electronic structure of many of these molecules.

1.3 Previous studies of metal containing intermediates

The metal-containing species that are of most interest to the Leicester laser spectroscopy group are binary complexes of the type M-L, where M is a metal and L is a ligand of some description. These molecules are often highly reactive intermediates where either the metal *e.g.* in MgCCH[15], or the ligand *e.g.* in LiO,[16] does not possess a full co-ordination shell. The simplest species of this type are diatomic molecules and large amount of information on these molecules exists in this literature. Although much is known about diatomic molecules, there is still plenty awaiting discovery. Gas-phase studies of diatomic metal containing radicals have employed a number of techniques including conventional absorption and emission, IR diode laser absorption, microwave absorption, photoelectron, LIF and REMPI spectroscopies. Although no single review covers the vast amount of work in this field, the book by Huber and Herzberg[17] summarises the work up until 1977, and provides appropriate references. A commercial database produced by Bernath[18] covers more recent studies.

In comparison to the amount of data on diatomic metal-containing intermediates their polyatomic equivalents have received relatively little attention. This may be because the expected vibrational and rotational structure of polyatomic species is more congested, thus making spectra more difficult to interpret. However, the study of polyatomic radicals should not be neglected, for a number of reasons. First of all, many are important chemical intermediates. Second: studies of molecules of the form M-L allows the metal-ligand bond to be investigated free from any perturbations caused by other ligands. Multi-ligated metal centres in coordination compounds are the norm and mono-ligated metals are the exception. Thus the study of mono-ligated metals in the gas phase allows the role of ligand cooprativity to be accessed, at least in principle.

An important development in the study of metal-containing polyatomic molecules was the discovery that alkaline earth metal-containing monohydroxide radicals (MOH, M=Mg, Ca, Sr, and Ba) [19-22] and the isoelectronic alkaline earth monoamides[21,22] (MNH_2, M=Ca, Sr, and Ba) could be prepared in a Broida oven. The advantages of the

Broida oven technique over flame studies is that the molecules are cooler than in flames (about room temperature compared to several hundred degrees in flames) and in flames many possible species exist, while in the Broida oven the numbers of species should be significatly less. In the Broida oven technique, the metal of interest is thermally evaporated using resistive heating and then mixed with a suitable precursor gas to produce the desired species. There are however, two serious limitations of the Broida oven method. Firstly, it is difficult to apply to metals with high boiling points. Secondly, and often of more spectroscopic importance, the species are formed from hot metal atoms and so have quite high internal energies (although significantly lower than flames), making spectra highly congested. This is particularly a problem when trying to record rotationally resolved spectra.

Bernath and co-workers continued the work of Harris, described above, again using a Broida oven, and studied an extensive range of polyatomic mono-ligated alkaline earth metal compounds. The volume of work performed by Bernath and co-workers is extensive and has been summarised in two reviews written by Bernath. The first describes the early work on strontium and calcium derivatives up until ~1991.[23] The second reviews the significant progress in the study of alkaline earth derivatives from 1991 to 1997.[24] An important improvement Bernath made to the Broida oven method was to use a laser to excite the metal atoms. As in the original technique the metal atoms were evaporated, but then a tunable laser was used to promote them to the first excited metastable $^3P_1$ electronic state. This served to dramatically increase the concentration of product molecules as collisions between metal atoms and precursor molecules now contained enough energy to break bonds within the precursor and form the desired molecules. The extent of the improvement in the technique was demonstrated by the fact that Bernath and co-workers could not prepare several spesies unless the laser-driven enhancement was employed. Another advance introduced by Bernath and co-workers to the Broida oven method was in the use of LIF spectroscopy.

Recently, laser ablation has been used as an alternate source of metal atoms. Ablation has the advantage over a Broida oven that it can be combined with a supersonic jet

expansion to give relatively cold gas phase molecules. For high-resolution work another advantage using a supersonic jet is that the Doppler linewidth is reduced allowing small effects such as hyperfine splitting to be studied. Smalley and co-workers[26] first demonstrated that metal atoms could be ablated when they accidentally produced Al_x-acetyl and Al_x-acetone clusters following ablation of an aluminum target (the organic molecules in the clusters arose from acetone impurities in the helium carrier gas). Whitham *et al.*[27] first showed that laser ablation coupled to a supersonic jet expansion provides an excellent source of metal containing intermediates. They recorded jet cooled excitation spectra of CaL where L=OH, CCH, NH_2, or CN by ablation of Ca with a Nd:YAG laser (second harmonic 352 nm) in the presence of H_2O, HCCH, NH_3, and CH_3CN, respectively.

Miller and co-workers have improved the ablation/supersonic jet technique further. They noticed that the concentration of metal containing radicals of the form M-L could be significantly increased by using a UV excimer laser rather than a Nd:YAG laser to ablate metal atoms. In addition to ablating metal atoms the UV laser can simultaneously photolyse precursor molecules which can then react with nearby metal atoms. Miller and co-workers have demonstrated the effectiveness of this technique in recent studies of various organometallic radicals of zinc, cadmium, calcium, and magnesium.[29-37] Another technique utalised by Miller and co-workers was photolysis of organometallic molecules (*e.g.* $Zn(CH_3)_2$ to give $ZnCH_3$). This technique is simpler in principle, but limited by the number of precursor molecules that are commercially available. The advantages of this approach are (i) a higher concentration of radicals can be generated and (ii) cooler spectra can be achieved which is a point that is discussed further in Chapter 2.

Although UV photolysis and ablation are excellent techniques for the generation of metal containing intermediates in a supersonic jet expansion the cost of a UV laser is prohibitive for many researchers. Recently, Ellis and co-workers have investigated using electrical discharge as a cheaper alternative to laser photolysis. Povey *et al.*[38] used an electrical discharge to fragment relevant organometallic precursors in his study of the

$ZnCH_3$ and ZnC_2H_5 free-radicals. The work of Povey is the starting point for much of the work described within this thesis so details of this study are give in later sections. Another innovation by Ellis and co-workers was to use electrical discharge as an alternative to ablation/photolysis. Bezant *et al.*[39] demonstrated the technique by sputtering cadmium atoms from an electrode and reacting them with an organic radical source to produce CdC_2H_5.

Almost all the spectroscopic studies of organometallic intermediates in the gas phase carried out up until now contain metals from either group 2 (Mg, Ca, Sr or Ba) or group 12 (Cd or Zn). The only real exception to this is the work of Merer and co-workers. The lack of studies of transition metal organometallic species prompted them to begin a systematic spectroscopic investigation of the early transition metal methylidynes (MCH) and they currently have observed LIF spectra for M=Ti, V, Nb, Ta, and W.[40-43]

In addition to all these LIF studies, the observation of metal-containing species in the ISM by millimetre/submillimetre spectroscopy has lead to an increase in related Earth-based studies. Ziurys and co-workers have used a Broida oven technique to record pure rotational spectra of alkaline earth containing hydroxide,[44-47] cyanides and isocyanides,[52,53] monoacetalydes,[54-56] and monomethyls.[57-59] This work has enabled more precise rotational constants to be determined in the ground electronic states of all of these molecules.

1.4 This work

The work presented in this thesis is principally concerned with the identification, through spectroscopic analysis, of the binary metal-containing radical intermediates zinc monoethyl (ZnC_2H_5) and barium monohydroxide (BaOH). The general experimental methods for the generation of the radicals, and a brief description of the spectroscopic technique is given in Chapter 2.

The first observation of the ZnC_2H_5 free-radical was reported in 1994 by Povey *et al.* from the Leicester spectroscopy group.[38] They reported a strong vibrationally resolved LIF excitation spectrum in the range 22500-24000 cm^{-1}, but could only assign a single band, the $\tilde{A}-\tilde{X}\,0_0^0$ electronic origin with any certainty. At that time a dispersed fluorescence study was not undertaken. This is unfortunate because the assignment of vibrational structure in excitation spectra can be greatly assisted by recording complementary dispersed fluorescence spectra. It is also pertinent to note that Povey *et al.* carried out *ab initio* calculations of vibrational frequencies of the ground electronic state of ZnC_2H_5. Comparison of this theoretical data with dispersed fluorescence spectra is clearly more meaningful than excitation spectra since the former lead directly to ground state frequencies. Consequently Chapter 3 of this thesis describes a dispersed fluorescence study of ZnC_2H_5. Through this work a more complete analysis of the vibrational structure of the excitation spectrum of ZnC_2H_5 has been made.

A study that would compliment both the vibrationally resolved LIF study reported by Povey *et al.* and the DF work reported in Chapter 3, would be a rotationally resolved LIF study of ZnC_2H_5. Recently Professor T. A. Miller and his group at Ohio State University recorded rotationally-resolved excitation spectra of a number of the peaks previously studied at vibrational resolution. The analysis of these spectra have been carried out by the author at Leicester. Early in the analysis it became apparent that a new computer model which included a complete treatment of spin-rotation interactions, was need to simulate the rotationally-resolved spectra of ZnC_2H_5.

Chapter 4 details the development and testing of this model. The model, called ASYMSR, runs as part of the SpecSim program that was written by S. Panov at Ohio State University. The chapter details the Hamiltonian used in the model, the algorithm used to construct the Hamiltonian matrix and the theory necessary to calculated the intensities of transitions. The model is then tested against real and simulated spectra from the literature.

The analysis of the rotationally-resolved spectra of ZnC_2H_5 performed by the author is described in Chapter 5. Initially, analysis of the zinc isotope shift is discussed, which provides useful information on the vibrational structure, thus complimenting the work in Chapter 3. The latter part of the chapter deals with the use of the ASYMSR model to perform a preliminary analysis of the observed rotational and spin-rotation structure.

The final chapter, Chapter 6, contains an investigation of some electronic transitions of BaOH. The initial part of the chapter reports the first observation of the $\widetilde{D}^2\Sigma^+ - \widetilde{X}^2\Sigma^+$ system of this free-radical and discusses the vibrational and, to a lesser extent the rotational structure. The second half of this chapter describes the first jet-cooled investigation of the $\widetilde{C} - \widetilde{X}$ region.[14,60] The spectra reported here are significantly different from those reported previously under flame conditions.[14,60] One interesting feature reported here is the spectral region appears to contain two electronic transitions rather than just the one reported previously.

1.5 References

1. S.C. Foster and T.A. Miller, *J. Phys. Chem.*, **93**, 5986 (1989)
2. G.K. Teal, J.R. Fisher and A.W. Treptow, *J. Appl. Phys.*, **17**, 879 (1946)
3. M.L. Hitchman and K.F. Jensen, *Chemical Vapour Deposition: Principles and Applications*, Academic Press, London (1993)
4. A.C. Jones, *J. Cryst. Growth*, **55**, 129 (1981)
5. D.K. Russell, *Coord. Chem. Rev.*, **112**, 131 (1992)
6. J.E. Butler, N. Bottka, R.S. Sillmon and D.K. Gaskill, *J. Cryst. Growth*, **77**, 163 (1986)
7. J.M.C. Plane, *Int. Rev. Phys. Chem.*, **10**, 55 (1991)
8. T.J. Beatty, R.L. Collins, C.S. Gardner, C.A. Hostetler, C.F. Sechrist and C.A. Tepley, *Geophys, Res. Lett.*, **16**, 1019 (1989)
9. S. Chapman, *Astrophys. J.*, **90**, 309 (1939)
10. M. Guelin, J. Cernicharo, C. Kahane, and J. Gomez-Gonzales, *Astron. Astrophys*, **157**, L17 (1986)
11. K. Kawaguchi, E. Kagi, T. Hirano, S. Takano and S. Satio, *Astrophys. J.*, **406**, L39 (1994)
12. M.A. Anderson and L.M. Ziurys, *Chem. Phys. Lett.*, **231**, 164 (1994)
13. E.W. Weisstein and E. Serabyn, *Icarus*, **123**, 23 (1996)
14. C.G. James and T.M. Sugden, *Nature*, **175**, 133 (1955)
15. G.K. Corlett, A.M. Little and A.M. Ellis, *Chem. Phys. Lett.*, **249**, 53 (1996)
16. G.K. Corlett, A.M. Little and A.M. Ellis, *Chem. Phys. Lett.*,
17. K.P. Huber and G. Herzberg, *Spectra of Diatomic Molecules*, Van Nostrand, New York (1950)
18. P.F. Bernath, *Spectroscopic References for Diatomic Molecules*, Northern Spectronics Inc., Waterloo, Ontario, Canada (1996)
19. J. Hakagawa, R.F. Wormsbecher, and D.O. Harris, *J. Mol. Spectrosc.*, **97**, 73, (1983)
20. R.C. Hilborn, Q. Zhu, and D.O. Harris, *J. Mol. Spectrosc.*, **97**, 73 (1983)
21. R.F. Wormsbecher, R.E. Penn and D.O. Harris, *J. Mol. Spectrsc.*, **97**, 65 (1983)

22. R.F. Wormsbecher, M. Trkula, C. Martner, R.E. Penn and D.O. Harris, *J. Mol, Spectrosc.*, **97**, 29 (1983)
23. P.F. Bernath, *Science,* **254**, 665 (1991)
24. P.F. Bernath, *Adv. Photochem.*, in press
25. S. Kinsey-Nielson, C.R. Braizier and P.F. Bernath, *J. Chem. Phys.*, **84**, 698 (1986)
26. T.G. Diaz, M.A. Duncan, D.E. Powers, and R.E. Smalley, *J. Chem. Phys.*, **74**, 6511 (1981)
27. C.J. Whitham, B. Soep, J-P. Visticot and A. Keller, *J. Chem. Phys.*, **93**, 991 (1991)
28. Z. Morbi, C. Zhao, and P.F. Bernath, *J. Chem. Phys.*, **108**, 8891, (1997)
29. A.M. Ellis, E.S.J Robles and T.A. Miller, *J. Chem. Phys.*, **94**, 1752 (1991)
30. E.S.J Robles, A.M. Ellis and T.A. Miller, *Chem. Phys. Lett.*, **178**, 185 (1991)
31. A.M. Ellis, E.S.J Robles and T.A. Miller, *Chem. Phys. Lett.*, **190**, 599 (1992)
32. E.S.J Robles, A.M. Ellis and T.A. Miller, *J. Chem. Phys.*, **96**, 3247 (1992)
33. E.S.J Robles, A.M. Ellis and T.A. Miller, *J. Chem. Phys.*, **96**, 3258 (1992)
34. E.S.J Robles, A.M. Ellis and T.A. Miller, *J. Chem. Soc. Faraday Trans.*, **88**, 1927 (1992)
35. E.S.J Robles, A.M. Ellis and T.A. Miller, *J. Am. Chem. Soc.*, **114**, 7171 (1992)
36. E.S.J Robles, A.M. Ellis and T.A. Miller, *J. Phys. Chem.*, **96**, 8791 (1992)
37. R. Rubino, J.M. Williamson and T.A. Miller, *J. Chem. Phys.*, **103**, 5964 (1995)
38. I.M. Povey, G.K. Corlett, A.J. Bezant and A.M. Ellis, *J. Phys. Chem.*, **98**, 10427 (1994)
39. A.J. Bezant and A.M. Ellis, *J. Mol. Spec.*, **185**, 54 (1997)
40. M. Barnes, P.G. Hajigeorgiou, R. Kasrai, A.J. Merer and G.F. Metha, *J. Am. Chem. Soc.*, **117**, 2096 (1995)
41. M. Barnes, D.A. Gillet, A.J. Merer and G.F. Metha, Unpublished observations.
42. M. Barnes, D.A. Gillet, A.J. Merer and G.F. Metha, *J. Chem. Phys.*, **105**, 6168 (1996)
43. M. Barnes, A.J. Merer and G.F. Metha, *J. Mol. Spectrosc.*, **181**, 168 (1997)
44. L.M. Ziurys, W.L. Barclay and M.A. Anderson, *Astrophys. J.*, **384**, L63 (1992)

45. M.A. Anderson, W.L. Barclay and L.M. Ziurys, *Chem. Phys. Lett.*, **196**, 166 (1992)

46. W.L. Barclay, M.A. Anderson and L.M. Ziurys, *Chem. Phys. Lett.*, **196**, 225 (1992)

47. M.A. Anderson, M.D. Allen, W.L. Barclay and L.M. Ziurys, *Chem. Phys. Lett.*, **205**, 415 (1993)

48. D.A. Fletcher, M.A. Anderson, W.L. Barclay and L.M. Ziurys, *J. Chem. Phys.*, **102**, 4334 (1995)

49. P.R. Bunker, M. Kolbuszewski, P. Jensen, M. Brumm, M.A. Anderson, W.L. Barclay, L.M. Ziurys, Y. Ni and D.O. Harris, *Chem. Phys. Lett.*, **239**, 217 (1995)

50. B.P. Nuccio, A.J. Apponi, and L.M. Ziurys, *J. Chem. Phys.*, **103**, 9193 (1995)

51. L.M. Ziurys, D.A. Fletcher, M.A. Anderson and W.L. Barclay, *Astrophys. J. Supp. Series*, **102**, 425 (1996)

52. M.A. Anderson, T.C. Steimle and L.M. Ziurys, *Astrophys. J.*, **429**, L41 (1994)

53. M.A. Anderson and L.M. Ziurys, *Chem. Phys. Lett.*, **231**, 164 (1994)

54. M.A. Anderson and L.M. Ziurys, *Astrophys. J.*, **439**, L25 (1995)

55. M.A. Anderson and L.M. Ziurys, *Astrophys. J.*, **444**, L57 (1995)

56. B.P. Nuccio, A.J. Apponi and L.M. Ziurys, *Chem. Phys. Lett.*, **247**, 283 (1995)

57. M.A. Anderson and L.M. Ziurys, *Astrophys. J.*, **452**, L157 (1995)

58. M.A. Anderson and L.M. Ziurys, *Astrophys. J.*, **460**, L77 (1996)

59. M.A. Anderson, J.S. Robinson and L.M. Ziurys, *Chem. Phys. Lett.*, **257**, 471 (1996)

60 H. Haraguchi, S.J. Weeks and J.D. Winefordner, Spectrochim. Acta A, **35** 391 (1979)

Chapter Two

Experimental

2.1 Introduction

The focus of the experiments described within this thesis is the study of radical intermediates generated using one of several techniques and probed with laser induced fluorescence (LIF) spectroscopy. This chapter contains a description of the experimental details common to all of the experiments while details specific to individual experiments are given within appropriate results chapters. Figure 2.1 shows a schematic diagram showing the main features of the apparatus and gives an idea of how they are all interlinked. The colours in the diagram illustrate the principal functions of the apparatus, namely generation of gas sample, the laser systems, the detection of fluorescence and the control electronics. Each will now be described in detail.

2.2 Supersonic jet expansion

Supersonic jet expansions have had a profound influence on the field of molecular spectroscopy over the last twenty years and several good reviews of the principles and properties have been written.[1-3] In this section only a brief account of supersonic jets is given. Among the advantages a supersonic jet holds for the spectroscopist are (i) that molecules within it are rotationally, and to some extent vibrationally, cold and thus their spectra are simplified, and (ii) the collision-free environment is conducive to studying highly reactive open-shell molecules.

The key feature of the supersonic free jet expansion is a small orifice, sometimes also refered to as a nozzle, which separates a region of high pressure from one kept at low pressure using vacuum pumps. To maintain this pressure difference high pumping speeds are required or, as in our system, a pulsed valve is used to give a pulsed expansion. As the molecules escape from the region of high pressure collisions occur which transform the random velocity of molecular motion into a stream of atoms/molecules moving away from the nozzle at almost constant velocity (see Figure 2.2).

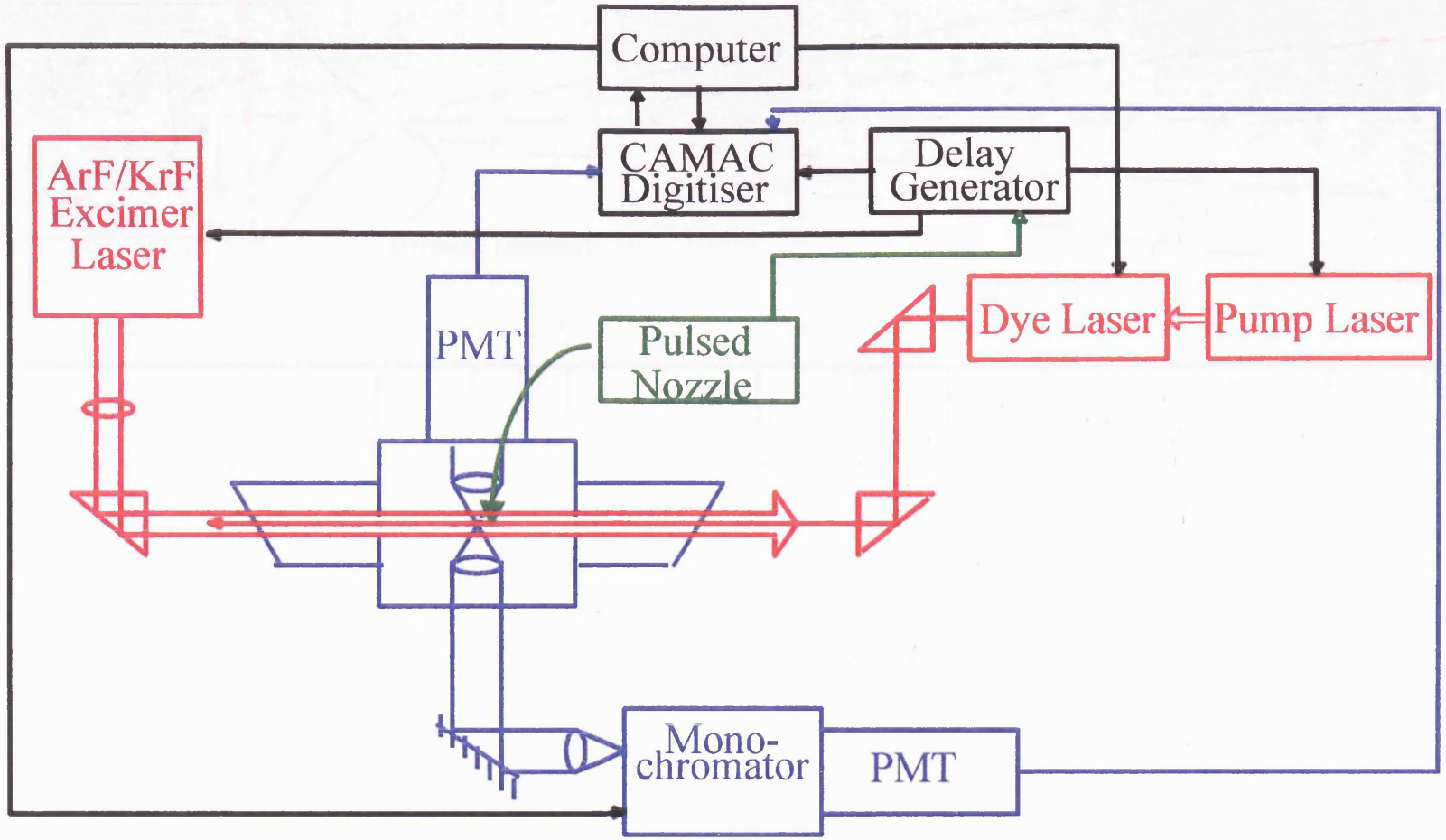

Figure 2.1: Schematic diagram of experimental apparatus

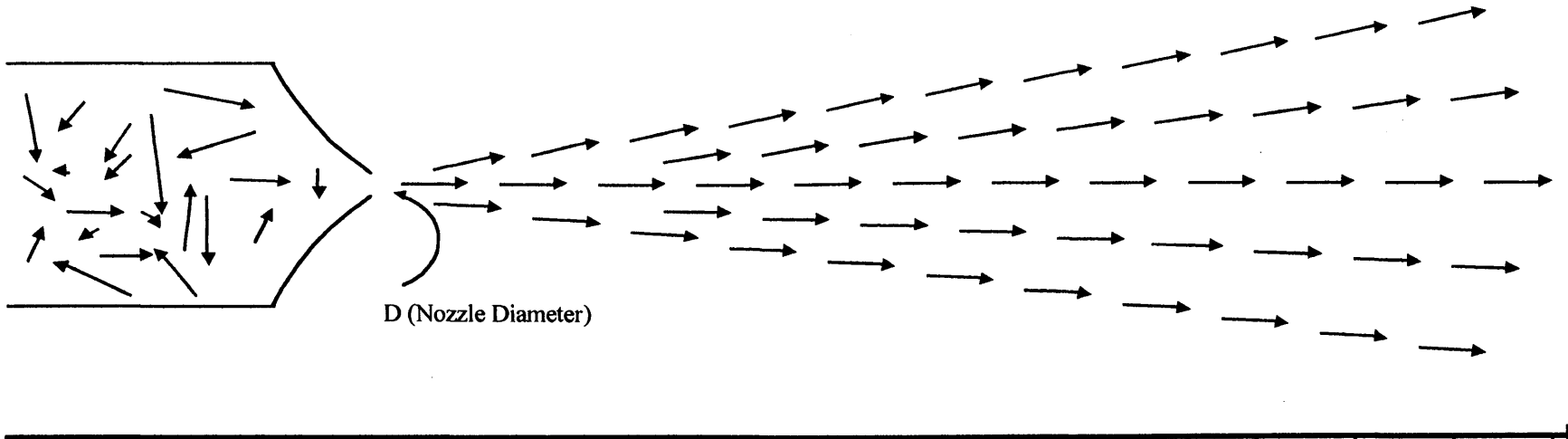

Distance (X/D)	10	20	30	40	50	60
Translational Temperature (K)	4.0	1.6	0.9	0.6	0.5	0.4
Pressure (mtorr)	150	15	3.5	1.5	0.7	0.4
Collisions (5→X)	80	106	112	115	117	119

Figure 2.2: Schematic diagram of a free jet expansion (adapted from reference 2). The parameters shown above are for a helium expansion at a stagnation pressure of 10 barr

The translational temperature of the molecules within a jet expansion is proportional to the width of the velocity distribution and this can be so narrow that temperatures of < 1 K are easily achieved. Collisions occurring within the early stages of expansion can also cool the internal degrees of freedom, vibrations and rotations, by transferring energy to the cold translational bath. As the expansion proceeds the density of gas and the number of collisions decreases, preventing the internal energy levels reaching an equilibrium temperature. Typically, rotational→translational energy transfer is rapid, and the rotational temperature may approach the translational temperature. Vibrational→translational cooling is much slower and may be strongly mode dependent. Substantial vibrational cooling may sometimes be observed, but vibrational temperatures of <50 K are rarely achieved.

Supersonic jet expansions of the molecular precursor of interest are not used in experiments described within this thesis because (i) the species of interest are unstable radicals and are therefore likely to undergo reactions with the precursor or other free radicals, and (ii) extensive condensation is a problem with molecular expansions. Hence, molecular species are seeded at low concentration (<2%) into a supersonic expansion of an inert carrier gas, usually argon or helium.

2.2.1 The sample delivery system

All of the experiments described required a gaseous precursor, be it an organometallic molecule for fragmentation or some reagent for reacting with metal atoms. As stated above, these precursor molecules were seeded in low concentration into an inert carrier gas. The sample delivery system, shown in Figure 2.3, mixes the precursor and carrier gas and delivers them, through a pulsed valve, to a fixture where fragmentation or reaction occurs (see later sections).

All of the tubing in the sample delivery system has a diameter of 0.25″. Those parts in which solely carrier gas flow (A on the diagram) are copper while the remainder is stainless steel. The tubing is joined using Swagelock elbows and t-pieces and the valves shown in the diagram are a mixture of Nupro bellows and Whitey regulating valves. Tube E on the diagram leads to the vacuum chamber (see section 2.4) for evacuation of

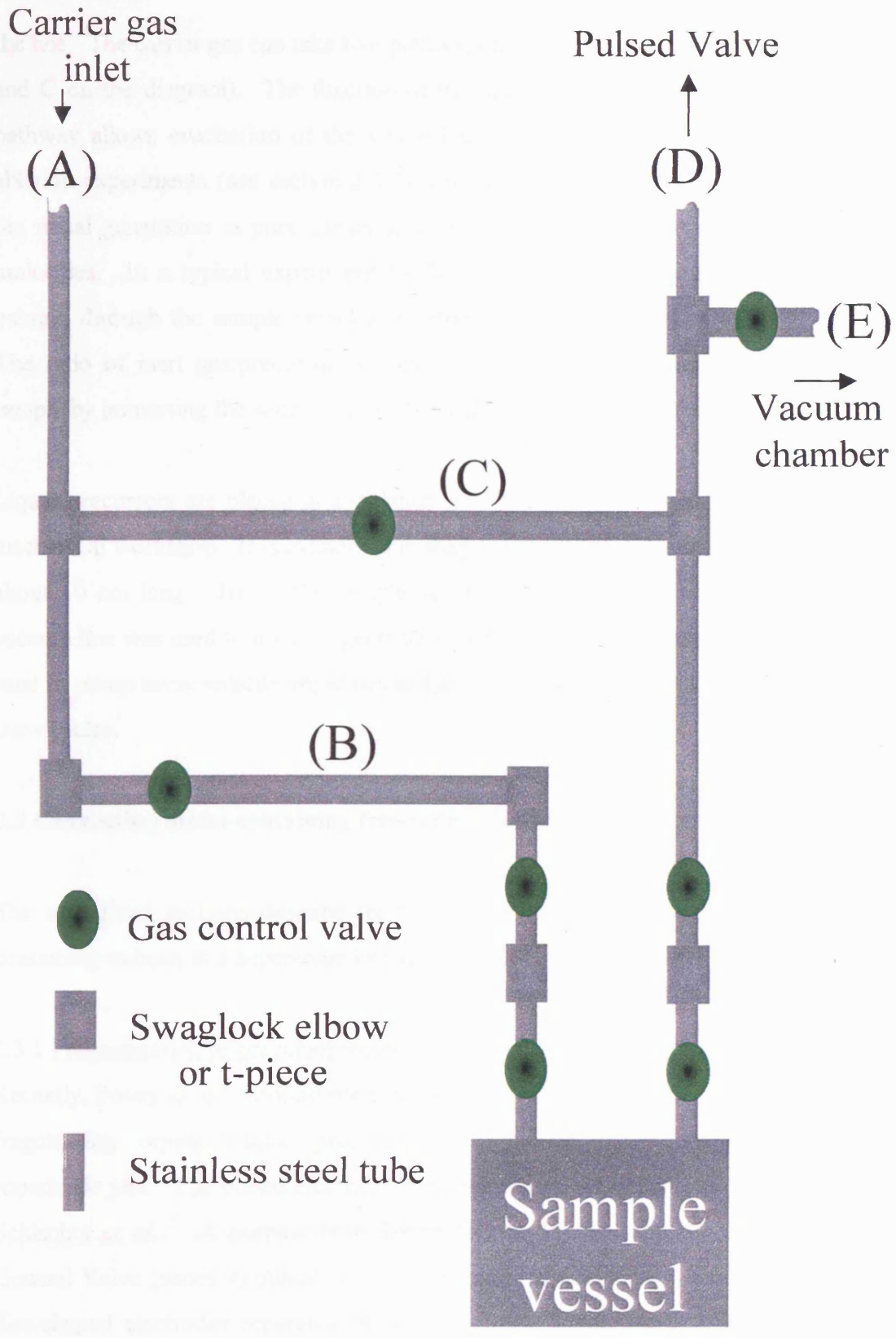

Figure 2.3 Schematic diagram showing the gas delivery system

the line. The carrier gas can take two pathways through the gas delivery system (tubes B and C on the diagram). The function of the upper pathway is two-fold: (i) using this pathway allows evacuation of the whole line apart from the sample; and (ii) in laser ablation experiments (see section 2.3.3) it is often favourable to observe the quality of the metal generation in pure carrier gas before attempting to introduce the precursor molecules. In a typical experiment the lower path (path B) is used, the carrier gas passing through the sample vessel and entraining sample molecules into the gas flow. The ratio of inert gas:precursor is controlled by varying the vapour pressure of the sample by immersing the sample vessel in constant temperature baths.

Liquid precursors are placed in a stainless steel sample vessel built by the departmental mechanical workshop. It is cylindrical in shape with an internal volume of 21 cm^3 and is about 10 cm long. To fill the sample vessel with air-sensitive precursors, a separate vacuum line was used to distil reagents into the vessel. The gas delivery system was also used to pump away volatile impurities and air from samples using standard freeze-pump-thaw cycles.

2.3 Generating metal-containing free-radicals in supersonic jets

The next three sections describe the techniques used in this work to produce metal containing radicals in a supersonic jet expansion.

2.3.1 Fragmentation of precursor molecules using an electrical discharge

Recently, Povey *et al.*[4] demonstrated that an electrical discharge was a successful way of fragmenting organometallic precursors to generate metal-containing radicals in supersonic jets. The pulsed electrical discharge nozzle was similar to that described by Schlachta *et al.*.[5] A purpose-built Teflon fixture was attached to the faceplate of a General Valve (series 9) pulsed valve. The fixture consisted of a Teflon base with two disc-shaped electrodes separated by a 2 mm thick Teflon spacer. The length of the fixture could be altered by attaching Teflon end-pieces of various lengths (2-5 mm). A 2 mm diameter hole down the centre allowed gas to flow from the pulsed valve through to the vacuum chamber on opening of the pulse valve.

Figure 2.4(a) gives a clearer picture of how the fixture is constructed. The choice of electrode material appeared to have no major significance, with either copper or zinc electrodes being used in the experiments described within this thesis. The electrodes were connected via insulated wire and vacuum feedthroughs to a home-made high voltage dc power supply. The high voltage was constantly applied across the electrodes but while gas was not present in the fixture (while the pulsed value was closed) no discharge could occur. Only when the pulsed valve fires and fills the fixture with gas can discharge take place. Voltages of > 500 V caused discharge ignition. Emission of light by the discharge was detected by a photomultiplier tube (PMT) and this provided vital diagnostic information on the discharge. A digital oscilloscope (Tektronix, TDS320) was used to display the real-time PMT signal and this was essential in the optimisation of discharge parameters. A large glow was observed in the initial stages of discharge so in a typical experiment the dye laser pulse was delayed until the glow subsided to reduce background noise.

2.3.2 Fragmentation by UV laser photolysis

The rotationally resolved electronic spectra of ZnC_2H_5 described in Chapter 5 were recorded at the Ohio State University by Professor T. A. Miller and co-workers. Diethyl zinc vapour was seeded into a helium carrier gas and expanded in a supersonic jet. ZnC_2H_5 radicals were produced by UV laser photolysis just beyond the exit of the pulsed valve and were detected further downstream using laser induced flourescence (LIF) spectroscopy (for more details see Chapter 5).

2.3.3 Laser ablation

The focused beam from a pulsed laser, if sufficiently powerful, can be used to ablate any metal. Laser ablation has been widely used to generate metal atoms and clusters in a supersonic jet expansion.[6] More recently the use of the technique has been extended to ablating metal atoms and further reacting them with a precursor molecule to make new metal-containing species.[7] Laser ablation was used in the work on BaOH described in Chapter 6.

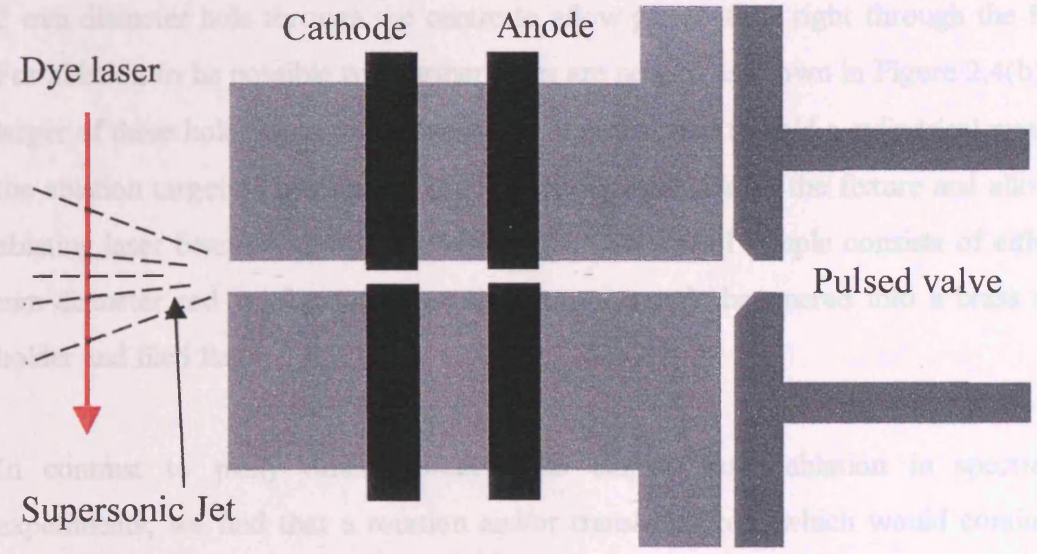

Figure 2.4 (a): Schematic diagram of the electrical discharge fragmentation nozzle

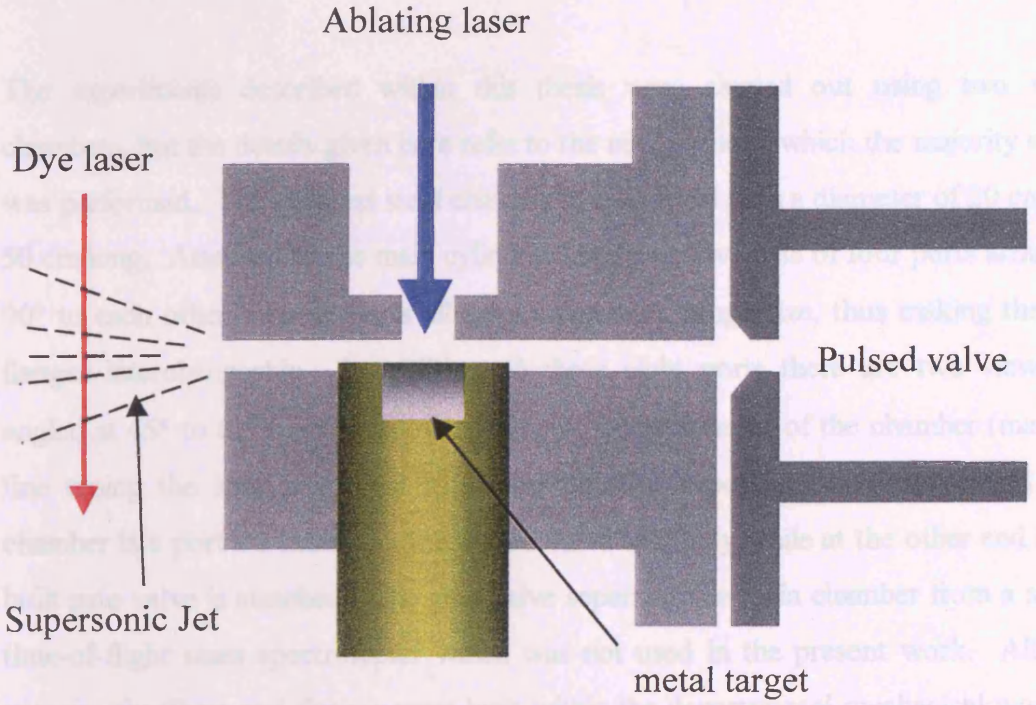

Figure 2.4 (b): Schematic diagram of the laser ablation nozzle

To carry out an ablation experiment within our laboratory an ablation fixture (Figure 2.4 (b)) is attached to the faceplate of a General Valve series 9 pulsed valve. The fixture was machined from a block of aluminium in the departmental mechanical workshop. It has a 2 mm diameter hole through the centre to allow gas to flow right through the fixture. For ablation to be possible two further holes are needed as shown in Figure 2.4(b). The larger of these holes has a 0.25" diameter and is designed to hold a cylindrical metal rod, the ablation target. The other hole is on the opposite side of the fixture and allows the ablating laser beam to strike the metal target. The metal sample consists of either a 6 mm diameter rod or, for softer metals, a metal sample hammered into a brass sample holder and filed flat.

In contrast to many other workers who employ laser ablation in spectroscopy experiments, we find that a rotation and/or translating rod, which would continuously expose fresh metal surface to the ablating laser beam, to be quite unnecessary. The experiments described in Chapter 6 used a static beam target.

2.4 The vacuum chamber

The experiments described within this thesis were carried out using two vacuum chambers, but the details given here refer to the newer one in which the majority of work was performed. The stainless steel chamber is cylindrical with a diameter of 20 cm and is 50 cm long. Attached to the main cylindrical body are two sets of four ports arranged at 90° to each other. These ports all have a common flange size, thus making the added flanges interchangeable. In addition, to these eight ports there are two view ports, angled at 45° to the vertical, allowing viewing of the interior of the chamber (mainly for fine tuning the laser alignment in a laser ablation experiment). On one end of the chamber is a port for mounting the pulsed valve assembly while at the other end a home built gate valve is attached. The gate valve separates the main chamber from a separate time-of-flight mass spectrometer which was not used in the present work. All of the vacuum chambers and flanges were built within the departmental mechanical workshop. Figure 2.5 shows a schematic diagram of the chamber.

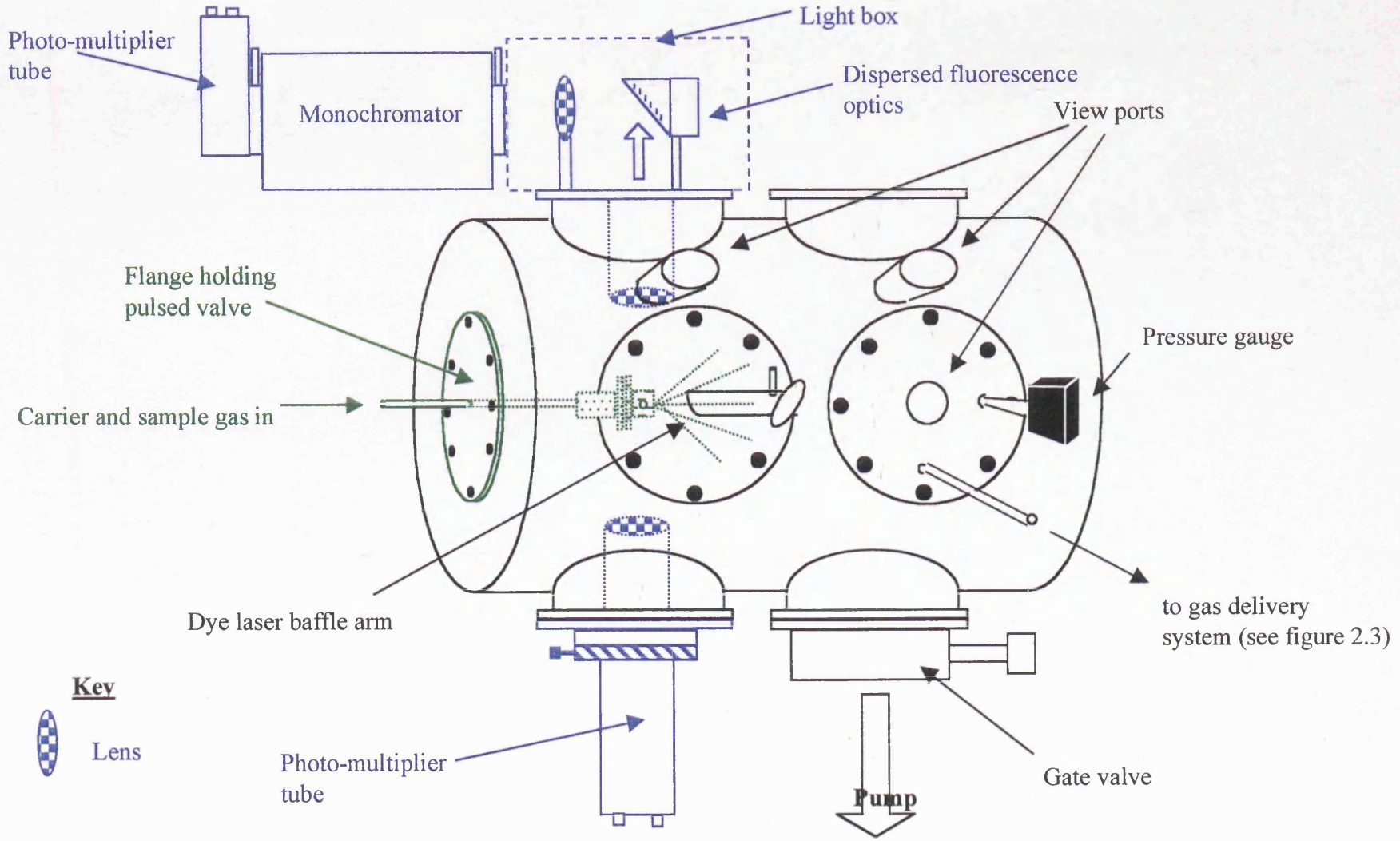

Figure 2.5: Schematic diagram of the vacuum chamber

The pulsed valve is connected to 0.25″ stainless steel tubing which passes into the chamber via a Cajon compression fitting located on the outside of the end flange. This flange also contains electrical feedthroughs for supplying power to the pulsed valve; in addition to these there are a further two electrical feedthroughs for discharge experiments. Two of the horizontal ports on opposite sides of the chamber are used to attach baffle arms, through which the excimer and dye laser beams enter the chamber. Above and below the baffle arms are two ports used for collecting fluorescence. The lower port holds an f/1.3 lens for imaging fluorescence onto a photomultiplier tube (PMT), while the upper port leads to a simple optical arrangement for dispersed fluorescence experiments (see section 2.6.2). Of the other four ports only two are normally used in LIF experiments. A 500 m^3/h roots pump (Leybold WAU501) backed by a 40 m^3/h rotary pump (Leybold D40B) is connected to the bottom flange via a gate valve. In addition, one of the side ports is used to attach a Pirani vacuum gauge and chamber venting valve.

2.5 The laser systems

The schematic diagram of the experimental apparatus (Figure 2.1) shows two laser systems; a Nd:YAG pumped dye laser as the tunable source employed for laser spectroscopy, and an excimer laser for generation of radicals through laser ablation or photolysis. In actual fact two dye laser systems were used for recording the spectra discussed in later chapters. Early experiments, namely those reported in Chapter 3, were carried out using a Quanta-Ray GCR-11 Nd:YAG laser to pump a Spectra Physics PDL-3 dye laser; this system was on loan from the Laser Loan Facility at the Rutherford-Appleton laboratory. The results reported in Chapter 3 were obtained with a Lambda Physik Scanmate 2E dye laser pumped by a Continuum Surelite II Nd:YAG laser. As the Scanmate 2E was used more frequently the section on dye lasers below focuses mainly focus on this particular system.

2.5.1 Excimer lasers

Excimer is a contraction of the words **excited dimer,** which is the medium for laser action within an excimer laser. An excited dimer, or more generally an exciplex (**excited**

complex), is a molecule that is bound in an upper electronic state yet is unbound in its ground electronic state. Exciplexes are excellent candidates to form the active medium in a laser since, if significant numbers are formed, an automatic population inversion is obtained with respect to the dissociative ground state (see Figure 2.6). The wavelength of emitted light is dependent upon the exciplex created and Table 2.1 shows the wavelengths of common excimer lasers.

Table 2.1

Laser medium	ArF	KrCl	KrF	XeCl	XeF
Wavelength (nm)	193	222	248	308	357

The method employed within excimer lasers to generate exciplexes such as ArF is usually a fast transverse electrical discharge across a gaseous medium containing rare gas atoms and halogen molecules. A typical gas fill for the Lambda Physik Compex 100, the excimer laser system in the Leicester laser spectroscopy laboratory, is 15% He, 4.8% Ar, 0.15% F_2, with the remainder being Ne.

The mechanism through which the exciplexes are formed is not completely understood but it is thought that they may be generated through a pathway similar to the following (for ArF):

$$Ar+e^- \text{------} > Ar^*+e^- \quad (1)$$

$$Ar+e^- \text{------} > Ar^+ +2e^- \quad (2)$$

$$F_2+e^- \text{----} > F+F^- \quad (3)$$

$$Ar^*+F_2 \text{----} > ArF^*+F \quad (4)$$

$$Ar^+ +F^-+M \text{----} > ArF^*+M \quad (5)$$

The output beam from an excimer laser is pulsed and has a pulse duration of typically 5-20 ns. The pulsed nature makes it particularly suitable for use in conjunction with a pulsed supersonic jet and the high energy UV photons are excellent for the photolytic generation of radicals.

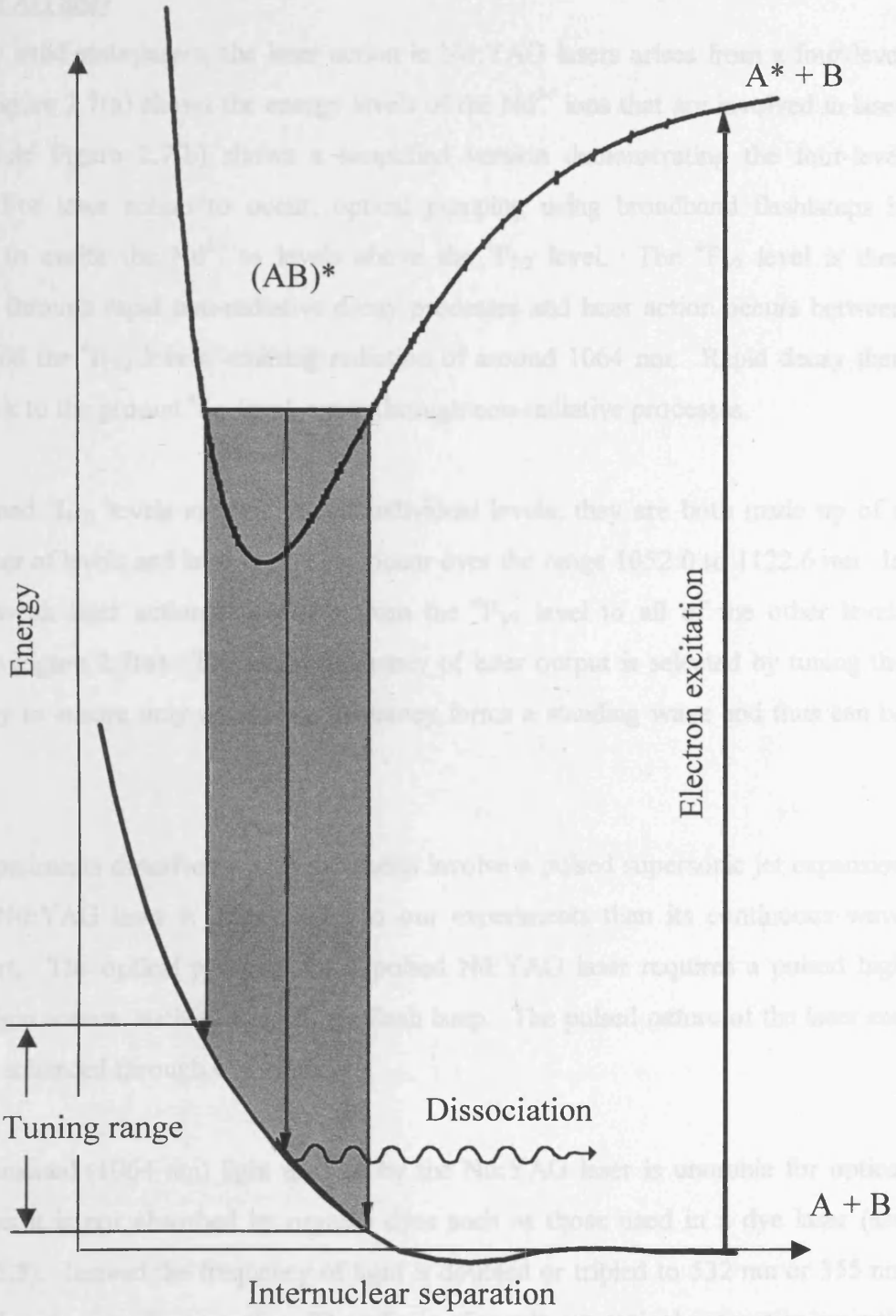

Figure 2.6: Schematic potential energy diagram for an excimer laser

2.5.2 Nd:YAG laser

Like many solid state lasers, the laser action in Nd:YAG lasers arises from a four-level system. Figure 2.7(a) shows the energy levels of the Nd^{3+} ions that are involved in laser action, while Figure 2.7(b) shows a simplified version demonstrating the four-level scheme. For laser action to occur, optical pumping using broadband flashlamps is necessary to excite the Nd^{3+} to levels above the $^4F_{3/2}$ level. The $^4F_{3/2}$ level is then populated through rapid non-radiative decay processes and laser action occurs between the $^4F_{3/2}$ and the $^4I_{11/2}$ levels, emitting radiation of around 1064 nm. Rapid decay then occurs back to the ground $^4I_{9/2}$ level, again through non-radiative processes.

The $^4F_{3/2}$ and $^4I_{11/2}$ levels are not in fact individual levels; they are both made up of a small cluster of levels and laser action can occur over the range 1052.0 to 1122.6 nm. In addition, weak laser action is possible from the $^4F_{3/2}$ level to all of the other levels marked on Figure 2.7(a). The exact frequency of laser output is selected by tuning the laser cavity to ensure only one lasing frequency forms a standing wave and thus can be amplified.

As the experiments described within this thesis involve a pulsed supersonic jet expansion a pulsed Nd:YAG laser is more suited to our experiments than its continuous wave counterpart. The optical pumping for a pulsed Nd:YAG laser requires a pulsed high intensity light source, such as an inert gas flash lamp. The pulsed nature of the laser can be further enhanced through Q-switching.

The fundamental (1064 nm) light emitted by the Nd:YAG laser is unusable for optical pumping as it is not absorbed by organic dyes such as those used in a dye laser (see section 2.5.3). Instead the frequency of light is doubled or tripled to 532 nm or 355 nm respectively using non-linear optics. The effects of non-linear optical properties are only observed with very high light intensities, such as that generated by lasers. For light sources of moderate intensity the electric field associated with the light induces polarisation through an oscillating dipole moment, which essentially represents the changes in separation of the positive and negative charges within the medium. The oscillating dipole moment, and thus the polarisation, is linearly proportional to the electric field, E, and related to the intensity of light, I, by

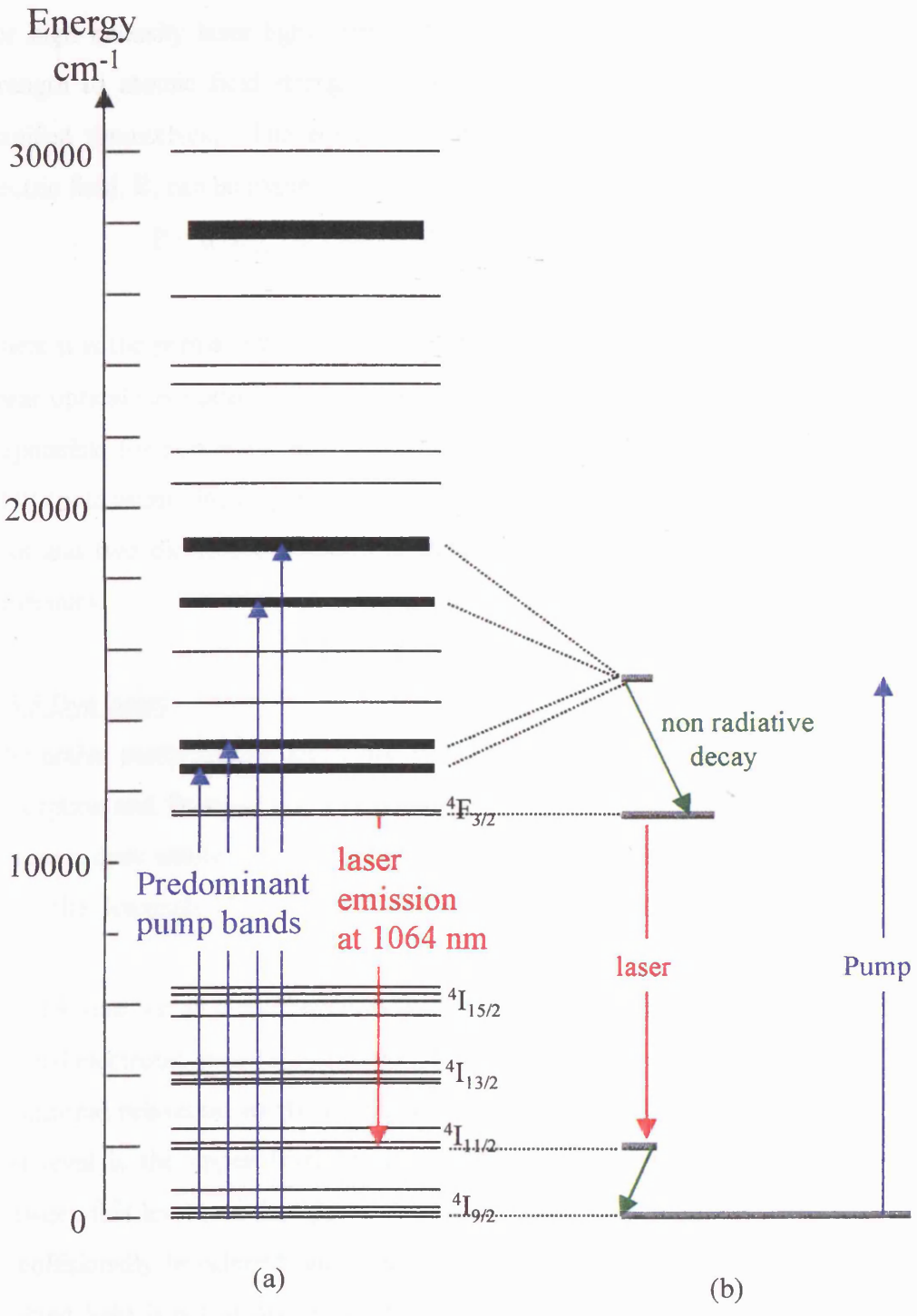

Figure 2.7: Energy levels of Nd^{3+} in a YAG crystal (a) in detail and (b) idealised showing the four-level nature of the laser system. (Adapted from reference 9)

$$I=1/2\varepsilon_0 cE^2 \qquad (6)$$

For high intensity laser light sources the induced electric field may be of comparable strength to atomic field strengths which may in turn cause non-linear phenomena to manifest themselves. The equation relating the instantaneous polarisation, **P**, in an electric field, **E**, can be expressed as

$$\mathbf{P} = \mu+\varepsilon_0\chi^{(1)}\mathbf{E} + \varepsilon_0(\chi^{(2)}\mathbf{E}^2 + \varepsilon_0\chi^{(3)}\mathbf{E}^3+.....) = \mathbf{P}_{\text{Linear}} + \mathbf{P}_{\text{Non-Linear}} \qquad (7)$$

where μ is the permanent electric dipole moment of the material along **E**, and $\chi^{(1)}$ is the linear optical susceptibility. The second- and third- order susceptibilities $\chi^{(2)}$ and $\chi^{(3)}$ are responsible for non-linear effects of the respective order. The Surelite II is fitted with KDP (potassium dihydrogen phosphate) crystals to generate second and third harmonic light and two dichroic separators to separate the 532 or 355 nm radiation from lower harmonics.

2.5.3 Dye lasers

The active media in dye lasers are solutions of organic dyes, which show broadband absorption and fluorescence on excitation with ultraviolet or visible light. With various different dyes tunable laser radiation over the spectral range 415-875 nm is achievable using the Scanmate 2E; this can be further extended through the use of non-linear optics.

Laser action within a dye begins with optical pumping which excites molecules from the ground electronic state (S_o) to some vibrational level of the first excited singlet state (S_1). Collisional relaxation to the zero point energy level of S_1 then occurs very rapidly and this level is the upper level for the population inversion. Laser action then occurs between this level and the upper vibrational levels of the S_0 state. Each rovibronic level is collisionally broadened, and this coupled with the high density of states means the emitted light is not at discrete wavelengths but instead, in the absence of a wavelength selection device (see below) forms a broad continuum. Optical pumping can be achieved using a number of light sources such as flash lamps or another laser. The Scanmate 2E

dye laser is pumped by the second or third harmonic of a Nd:YAG laser (see previous section)

Figure 2.8 shows the optical arrangement within the Scanmate 2E. One of the principal features is that the dye cell is transversely pumped by the Nd:YAG laser. Another is the dye laser beam is expanded onto a grating, as in the classic Hänsch-type of dye laser.[10] The output wavelength is determined by the angle the grating makes with the optical axis of the cavity. Amplification of broadband fluorescence (amplified spontaneous emission, ASE) is a problem that is often encountered with dye laser systems and the Scanmate 2E has an unusual means to reduce this; the beam expander spatially separates out the ASE, which follows the purple pathway on the diagram, from the laser radiation, thus drastically reducing the amount of outputted ASE. The linewidth of the laser light is ~0.2 cm^{-1}, but this can be reduced to ~0.02-0.03 cm^{-1} through the use of an intra-cavity Fabry-Perot étalon. A fraction of the pump beam, in our case a Nd:YAG laser, is split to pump the oscillator cell. The laser light from the oscillator is then amplified by a preamplifier and a main amplifier which are pumped using the remainder of the Nd:YAG light . As can be seen from the diagram the pre-amplifier and oscillator are housed within the same optical cell.

The Scanmate 2E also has the facility to frequency double the laser light to extend the tuning range into the ultraviolet. Phase-matched BBO crystals are used for this purpose.

2.6 Fluorescence detection

Laser induced fluorescence (LIF) spectroscopy is a simple technique in principle. It involves directing monochromatic light from a tunable laser into a sample. If the wavelength of light is resonant with a transition in the molecule it will be absorbed, thus promoting the molecule to an excited state. From this excited state a number of processes can occur including internal conversion, intersystem crossing, and fluorescence. In LIF spectroscopy, the sole desirable process (ordinarily) is fluorescence; if the others are prevalent then LIF is not a suitable technique for the study of that molecule as the fluorescence quantum yield will be low.

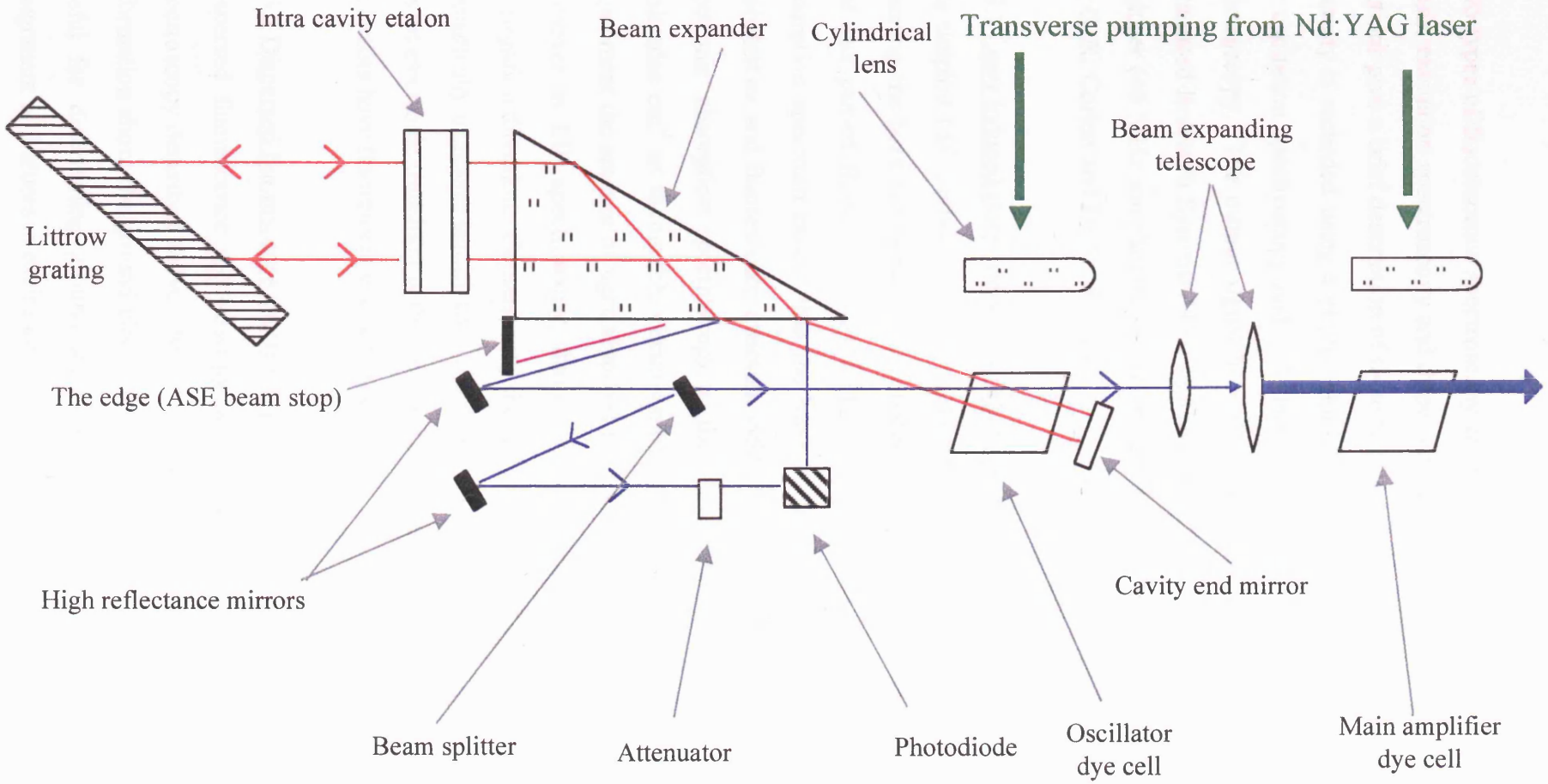

Figure 2.8: Schematic diagram showing the optical path through the Scanmate 2E dye laser

Two types of fluorescence spectroscopy were used in experiments described within this thesis, excitation spectroscopy and dispersed fluorescence spectroscopy. The next two sections give a brief description of these two techniques. In both cases the fluorescence intensity is recorded using a photomultiplier tube (PMT), a Hammamatsu R562 PMT, for excitation spectroscopy and a Hammanatsu R268 PMT for dispersed fluorescence spectroscopy. The output signal from the PMT was then amplified by a preamplifier (Stamford Research Systems 445), digitised by a CAMAC-based LeCroy 2262 transient digitiser (40 MHz sampling rate), and integrated using programs written by the author, Dr G. K. Corlett and Dr A. M. Ellis.

2.6.1 Laser induced fluorescence excitation spectroscopy

The simplest LIF method is excitation spectroscopy, in which a spectrum is obtained by scanning the laser wavelength and collecting either the total fluorescence or a portion that has passed through a cut-off filter. This is akin to recording a conventional absorption spectrum except that the band intensities are a convolution of absorption probabilities and fluorescence quantum yield. The advantage of LIF over conventional electronic absorption spectroscopy is the far greater sensitivity, as good as $\sim 10^5$ molecules cm^{-3} in favourable circumstances, that can be obtained. In an absorption experiment the amount of light absorbed is measured against a large background signal. However in LIF spectroscopy, fluorescence is measured at 90° to the laser beam propagation direction. Consequently the (ideally) small off-resonance background signal dramatically increases sensitivity. The disadvantages of LIF are that not every molecule has an electronic transition within the range of a tunable laser, and more seriously not all molecules have fluorescent excited states.

2.6.2 Dispersed fluorescence spectroscopy

Dispersed fluorescence spectroscopy is a technique that compliments the excitation spectroscopy described above. At the resolution we have employed, it gives vibrational information about the ground electronic state in particular. This information is not only useful for determining ground state vibrational frequencies but also helps in the assignment of features in excitation spectra.

In dispersed fluorescence spectroscopy, the tunable laser is fixed at a frequency that corresponds to a peak in the excitation spectrum. This will produce emission from a single vibronic (or even rovibronic) level. The fluorescence produced is passed through a monochromator and the fluorescence intensity at the given wavelength is recorded with a PMT. The grating in the monochromator is then moved to allow transmission of a new wavelength and the process repeated. Just as an excitation spectrum can be considered akin to a conventional absorption spectrum, a dispersed fluorescence spectrum is effectively an emission spectrum originating from a particular excited energy level.

The optical arrangement employed is shown in Figure 2.5. Briefly, the fluorescence is collected and made parallel using an f/1.5 lens, turned through 90° using a mirror, and is then focused upon the entrance slits of the monochromator with an f/2.0 lens. The 0.275 m monochromator (Acton Research SpectraPro 275) has two blazed holographic gratings mounted upon a rotating turret which is stepped by a computer-controlled motor. The grating used in a typical experiment can be operated over the range 190-800 nm. This grating has 1200 grooves/mm giving a potential maximum resolution of ±0.05 nm. As mentioned earlier, fluorescence is detected by PMT and is digitised and integrated using home written software. The additional subroutines for monochromator control and dispersed fluorescence data collection were written by the author.

2.7 References

1 D.H. Levy, *Science,* **214**, 263 (1981)

2 T.A. Miller, *Science,* **223**, 545 (1984)

3 P.C. Engleking, *Chem. Rev.,* **91**, 399 (1991)

4 I.M. Povey, A.J. Bezant, G.K. Corlett and A.M. Ellis, *J. Phys. Chem.*, **98**, 10427 (1994)

5 R. Schlacta, G. Lask, S.H. Tsay and V.E. Bondybey, *Chem. Phys.*, **155**, 267 (1991)

6 J.L. Gole, J.H. English and V.E. Bondybay, *J. Phys. Chem.*, **86**, 2560 (1982)

7 G.K. Corlett, A.M. Little and A.M. Ellis, *Chem. Phys. Lett.*, **249**, 53 (1996)

8 C.J. Whittam, B. Soep, J-P Viscot and A. Keller, *J. Chem. Phys.,* **93**, 991 (1990)

9 A.E. Siegman, *Lasers*, University Science Books, Mill Valley, California (1986)

10 T.W. Hänsch, *Appl. Opt.*, **11**, 895 (1972)

Chapter Three

Dispersed fluorescence spectroscopy of ZnC_2H_5

3.1 Introduction

Thin layers of group 12 metals are important in the semiconductor industry in the production of materials like ZnSe. These materials have traditionally been grown using CVD (chemical vapour deposition). Gaseous precursor molecules, usually organometallics, are heated in a reaction vessel and undergo thermal decomposition to deposit a thin layer on substrate surfaces. The high temperature of CVD can cause a lack of selectivity which leads to impurities (*e.g.* carbon) being incorporated into the film. UV photodissociation is an alternative to CVD with greater selectivity but until quite recently very little was known of the photodissociation mechanisms of group 12 dialkyls. One of the aims of the present work is to provide information which could give further understanding of the UV photodissociation of diethyl zinc.

On a more fundamental level, the monoalkyls of zinc and cadmium are, by the standards of organometallic chemistry, relatively simple molecules which might serve as useful models of metal-ligand bonding in more complex systems. The monomethyls of cadmium and zinc have been extensively studied recently,[1-5] and another aim of the work described within this chapter is to extend the previous work carried out on the monomethyls to larger species.

3.1.1 Review of recent work into $ZnCH_3$ and $CdCH_3$

It has been established for a number of years that photodissociation of the monomethyls of cadmium and zinc in the gas phase yields a metal atom and two methyl radicals. Bersohn and co-workers provided the first indirect evidence that the mechanism was a stepwise loss of alkyl radicals rather than a concerted loss of both methyl groups.[1] Confirmation was provided by Young *et al.*[2] who observed a new UV/visible spectrum on photodissociation of the dimethyls of zinc and cadmium: they assigned the new spectrum to the metal monomethyl radical intermediate.

More recently Jackson[3] recorded dispersed fluorescence spectra of $ZnCH_3$ by pumping the $\tilde{A}^2E\text{-}\tilde{X}^2A_1$ 0_0^0 and $2^1{}_0$ transitions. Vibrational structure arising from

the CH_3 umbrella (ν_2) and the Zn-C stretching (ν_3) modes were observed giving frequencies of 1060 cm^{-1} and 445 cm^{-1}, respectively, in the $\tilde{X}^2A_1$ ground state.

The time-dependent and pressure-dependent dispersed fluorescence spectra recorded by laser excitation to the $\tilde{A}^2E\text{-}\tilde{X}^2A_1\ 2_0^1$ level provided upper state information. Jackson[7] found that if the fluorescence measurement was delayed, typically 10 ns, after excitation then collisional redistribution of energy within the $\tilde{A}^2E$ state occurs. He found that v=1 of ν_3 in the upper spin-orbit component was populated and from the dispersed fluorescence spectra ν_3 was reported to have a vibrational frequency of 545 cm^{-1} in the $\tilde{A}^2E$ state. As the upper spin-orbit component was populated Jackson[7] was also able to report the spin-orbit splitting constant of 255 cm^{-1} for the $\tilde{A}^2E$ state. A disadvantage of Jackson's work is that an excitation spectrum was not recorded and so all conclusions about the of the $\tilde{A}^2E$ state are inferred.

Robles *et al.*[4] recorded the first jet cooled LIF spectra of $ZnCH_3$ and $CdCH_3$.[4] Like the earlier studies of $ZnCH_3$ by Young[2] and Jackson,[3] Robles *et al.* focused on the $\tilde{A}^2E\text{-}\tilde{X}^2A_1$ transition and both excitation and dispersed fluorescence spectra were obtained. Vibrational frequencies for ν_2 and ν_3 in the ground $\tilde{X}^2A_1$ state were, within experimental error, the same as that of Jackson[5] (1064 and 545 cm^{-1}). In addition, Robles *et al.* tentatively assigned ν_6, the CH_3 rock, to have a frequency of ~315 cm^{-1}. The upper state ($\tilde{A}^2E$) vibrational frequencies deduced by Robles *et al.* disagreed with those of Jackson. Robles reported a frequency of 460 cm^{-1} for ν_3 and observed no bands at 545 cm^{-1} (the frequency of ν_3 according to Jackson) to the blue of 0_0^0 position in the excitation spectrum.

Rotationally resolved LIF spectra of $ZnCH_3$ and $CdCH_3$ have also been reported.[5] Since it is more relevent to work described in Chapter 5, a review of the rotationally resolved work is defered until then. To close this section, the known vibrational frequencies of $ZnCH_3$ are summerised in Table 3.1.

Table 3.1: Vibrational frequencies in $ZnCH_3$ (from reference 4)

Mode	$\tilde{X}^2A_1$	$\tilde{A}^2E_{1/2}$	$\tilde{A}^2E_{3/2}$
ν_2	1000	902	
ν_3	356	400	413

3.1.2 Previous work on ZnC_2H_5

Jackson studied the photodissociation of dimethyl, diethyl and dipropyl zinc at 248 nm.[7] The intensity of the $4s6s\,^1S \rightarrow 4s4p\,^1P^0$ transition (19292.2 cm^{-1}) of atomic zinc was measured by LIF as a function of the total pressure of helium buffer gas. For $Zn(CH_3)_2$ the $ZnCH_3$ LIF intensity was also measured ($\tilde{A}^2E_{1/2} - \tilde{X}^2A_1\ 0_0^0$ transition at 23956 cm^{-1}), but for the other zinc dialkyls no fluorescence attributable to zinc monoalkyl radicals could be observed. From these experiments it was surmised that UV photodissociation of dialkyl zinc compounds involves absorption of one photon to break a Zn-R bond leaving behind a vibrationally hot zinc monoalkyl radical. At low pressures the hot monoalkyl zinc dissociates but at higher buffer gas pressures collisional cooling competes with spontaneous dissociation. In the photodissociation of $Zn(C_2H_5)_2$ and $Zn(n\text{-}C_3H_7)_2$ Jackson attributed, incorrectly as it turns out (at least for $Zn(C_2H_5)_2$),[8] the lack of observation of fluorescence from ZnC_2H_5 and ZnC_3H_7 to rapid non-radiative decay of the excited electronic state.

Observation of some of the 193 nm photoproducts of diethyl zinc was first made by Seider, who carried out infrared absorption experiments.[9] From an end product analysis it was also concluded that UV photodissociation occurred via a stepwise radical elimination mechanism.

Povey *et al.*[8] reported the first observation of the LIF spectrum of zinc monoethyl. A number of strong, relatively broad (FWHM ~10 cm^{-1}) bands in the range 22515 to 23600 cm^{-1} region where assigned to the ZnC_2H_5. As previously mentioned Jackson found no evidence of fluorescence from the zinc monoethyl radical.[7] However, it should be noted that Jackson limited his search to transitions above 23470 cm^{-1}. The spectrum recorded by Povey does show some features assigned to zinc monoethyl in

this region but they are relatively weak, thus providing a possible explanation for their nonobservation in Jackson's work. Unlike previous zinc monoalkyl studies,[1-6] including that of Jackson,[7] the technique used to generate ZnC_2H_5 was not UV photolysis but fragmentation of diethyl zinc with an electrical discharge. The different method of radical generation can be ruled out as a reason for Jackson's nonobservation of fluorescence as, subsequently, LIF spectra of ZnC_2H_5 have also been observed on photolysis of diethyl zinc (see Chapter 5).

Although the vibrationally-resolved excitation spectrum that was observed by Povey had an excellent signal/noise ratio none of the apparent vibrational structure could be confidently assigned. Among other potential complications, the lower equilibrium symmetry of zinc monoethyl compared to zinc monomethyl adds considerable spectral complexity.

The work of Povey *et al.* also included *ab initio* calculations at the Hartree-Fock level (double-ζ plus polarisation basis set) on the ground electronic state of ZnC_2H_5.[8] The aim of these calculations was to obtain an approximate structure of ZnC_2H_5 which is summarised diagramatically in Figure 3.1, and to predict vibrational frequencies. Since the structure observed in the excitation spectrum reflects excited rather than ground state vibrational intervals, the *ab initio* vibrational frequencies were necessarily of limited assistance in the assignment of the excitation spectrum. It would clearly be more appropriate to make comparisons with ground state vibrational observations and this is possible using dispersed fluorescence data.

In this chapter, the first dispersed fluorescence spectra of ZnC_2H_5 have been recorded. These have allowed us to probe some of the vibrational structure in the electronic ground state, particularly the skeletal Zn-C stretching and Zn-C-C bending modes. The dispersed fluorescence spectra have also provided important evidence that can be used to make some assignments of bands in the excitation spectrum. These new assignments are also presented here.

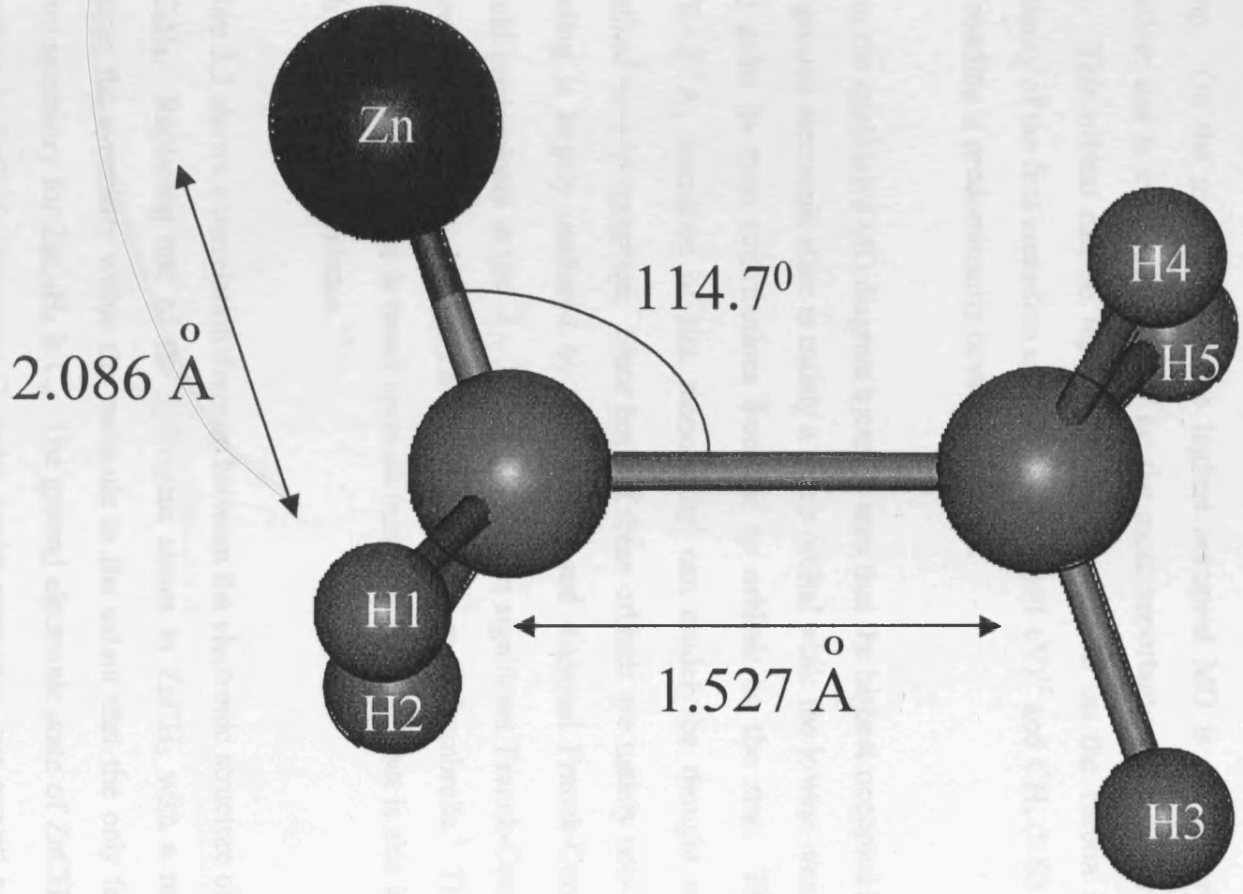

Figure 3.1 Diagramatic representation of the ZnC_2H_5 free-radical (the geometric parameters are taken from reference 8)

3.2 Electronic structure of monoalkyl zincs

A simple MO approach[11] (see Figure 3.2) to the electronic structure of zinc monomethyl can provide important information that is a useful aid in spectral assignment. Monomethyl zinc has an equilibrium geometry that has C_{3v} symmetry, *i.e.* it consists of a pyramidal CH_3 group with a zinc atom bonded to the carbon along the C_3 axis. The only valence orbitals upon the zinc atom that need consideration are the 4*s*, 4*p* and 5*s* as the 3*d* orbitals are completely filled and, to a first approximation, it is thought that they will have little overlap with the valence orbitals of the methyl group. On the methyl group the highest occupied MO is the a_2'' orbital in D_{3h} notation: this is expected to be by far the most important orbital in the bonding to zinc. This orbital can be represented as a p_z orbital on the carbon atom. The similarity of the first ionisation energies of Zn (9.391 eV)[12] and CH_3 (9.82 eV)[13] imply the bonding is predominantly covalent in nature.

From the qualitative MO diagram it can be seen that the highest occupied MO ($2a_1$) in the ground electronic state is mainly a zinc *s* orbital while the lowest unoccupied MO (1e) gains its main contributions from the 4*p* orbitals on the zinc. Therefore the $\tilde{A}^2E\text{-}\tilde{X}^2A_1$ transition of zinc monomethyl can crudely be thought of as a zinc localised 4*s*→4*p* transition. Since both of these orbitals are mainly non-bonding the bonding is largely unaltered by this process and diagonal Franck-Condon factors should predominate in the $\tilde{A}-\tilde{X}$ system. In fact significant Franck-Condon activity is seen in only two modes, the Zn-C stretch and the methyl umbrella.[4] The electronic structure presented here is based upon *ab initio* calculations[10] but is also in agreement with spectroscopic evidence.[1-5]

Figure 3.3 shows a correlation diagram between the electronic structure of $ZnCH_3$ and ZnC_2H_5. Replacing one of the hydrogens atoms in $ZnCH_3$ with a methyl group reduces the symmetry within the molecule to the extent that the only feasible point group symmetry for ZnC_2H_5 is C_s. The ground electronic state of $ZnCH_3$ is $^2A_1$ and therefore in ZnC_2H_5, assuming C_s point group symmetry, we expect a $^2A'$ ground state. The upper state in the strong LIF transitions of $ZnCH_3$, a ^2E state, will split

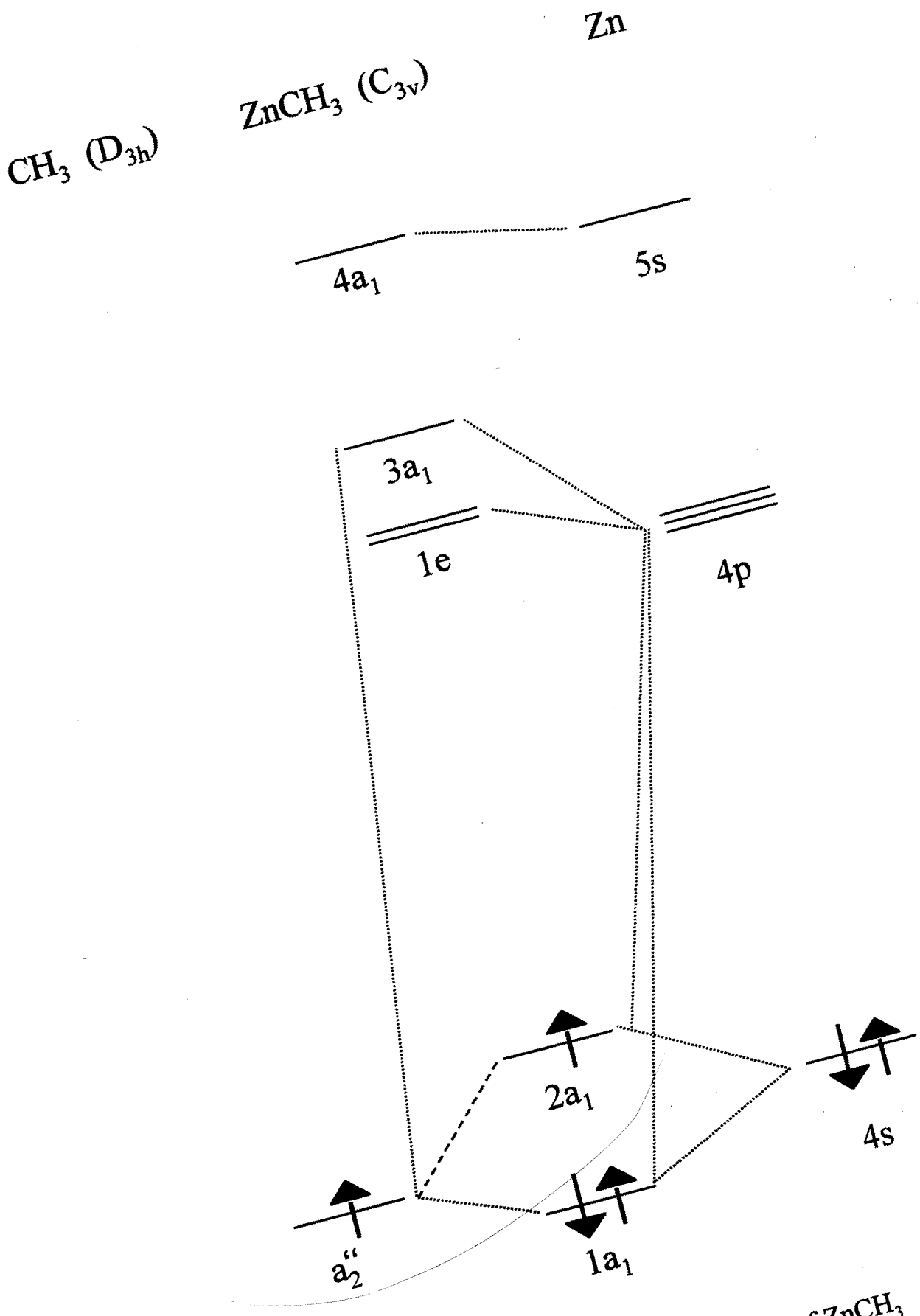

Figure 3.2 Schematic MO diagram of $ZnCH_3$

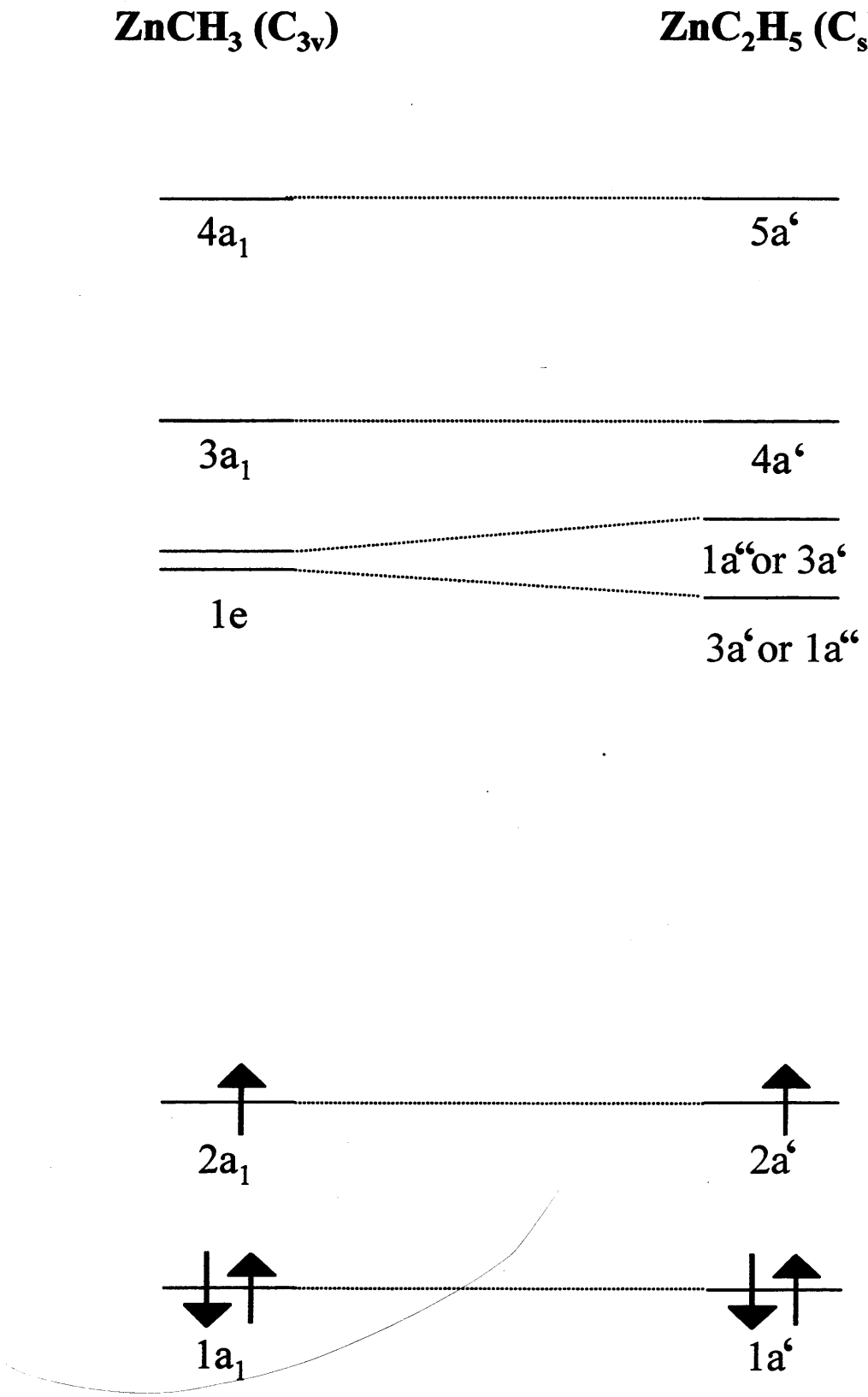

Figure 3.3 Correlation Diagram showing the correlation between the electronic structures of $ZnCH_3$ and ZnC_2H_5.

into $^2A'$ and $^2A''$ states in ZnC_2H_5. Transitions to both of these excited states from the ground state are optically allowed but there was no evidence from the LIF study of Povey *et al.*[8] to determine which has the lower energy.

3.3 Experimental

The experimental apparatus and procedure employed was similar to that described in detail in Chapter 2. ZnC_2H_5 was prepared by discharge fragmentation of diethyl zinc (Aldrich). The precursor was subjected to freeze-pump-thaw cycles before each experiment to ensure that no volatile impurities were present. In order to obtain a jet-cooled spectrum, the discharge of diethyl zinc, seeded in argon carrier gas, took place in a single-channel discharge nozzle prior to expansion into a vacuum chamber. About 2 cm downstream of the nozzle the expanding gas was crossed by the beam from a Nd:YAG laser pumped dye laser.

Fluorescence detection was as described in Chapter 2. One important point to note is that the resolution in the dispersed fluorescence spectra was approximately 20 cm^{-1} and the estimated accuracy in the quoted band positions is ±5 cm^{-1}.

3.4 Results and discussion

Figure 3.4 shows a broad survey of the laser excitation spectrum of ZnC_2H_5.[8] In addition to the relatively broad bands due to ZnC_2H_5, sharp lines from ZnH are clearly identifiable in the spectrum. The strong band at 22515 cm^{-1} is the lowest energy transition seen for ZnC_2H_5 and was therefore assigned to the $\tilde{A}-\tilde{X}$ 0_0^0 transition by Povey *et al.*.[8]

3.4.1 Dispersed fluorescence spectrum from pumping $\tilde{A}-\tilde{X}$ 0_0^0 transition

The dispersed fluorescence spectrum obtained on laser pumping the $\tilde{A}-\tilde{X}$ origin transition at 22515 cm^{-1} is shown in Figure 3.5. Several medium and low intensity bands are seen in addition to emission (and some scattering of laser light) at the excitation wavelength. Given that, by analogy with $ZnCH_3$, we expect no other

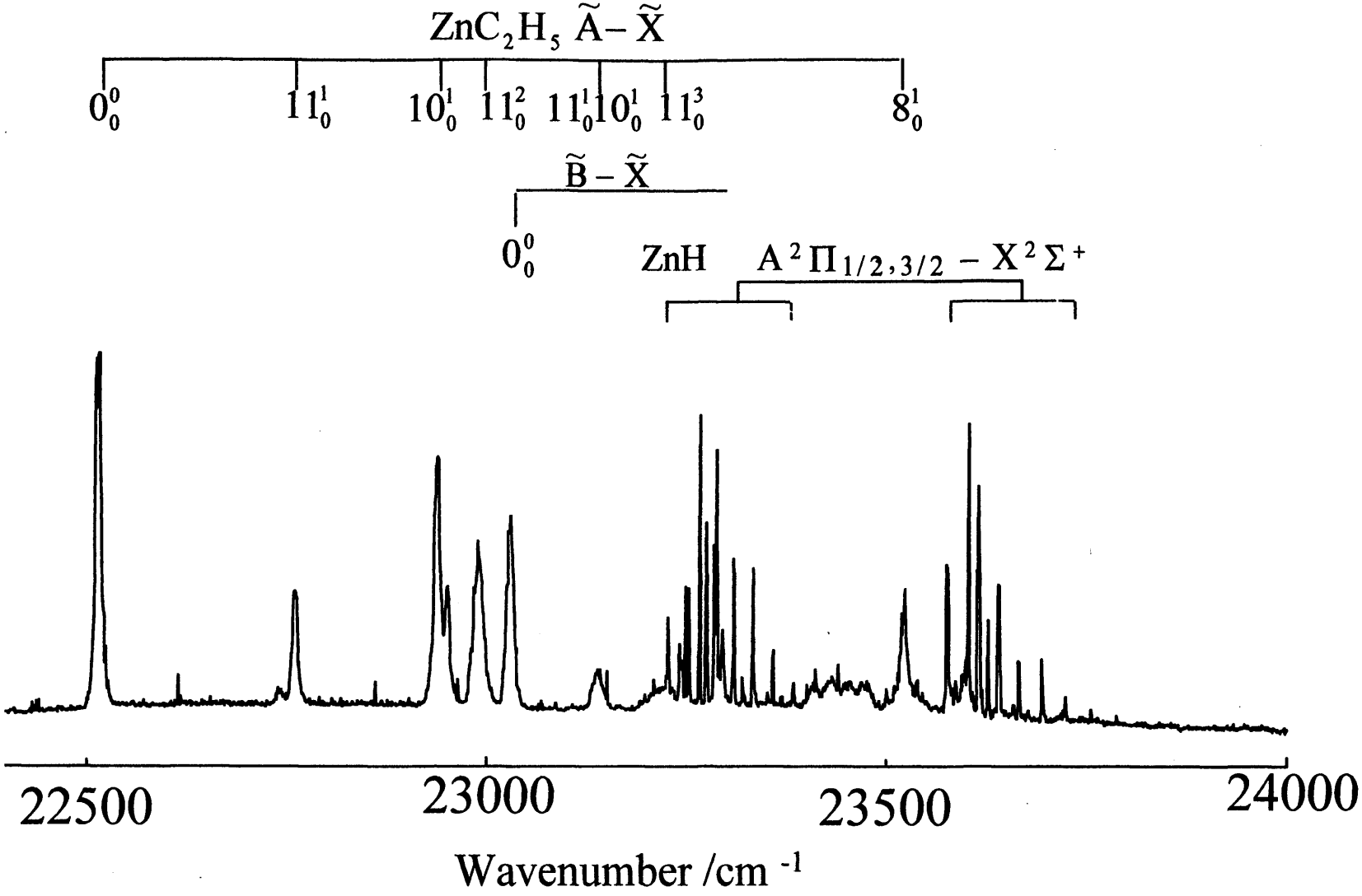

Figure 3.4 ZnC_2H_5 excitation spectrum

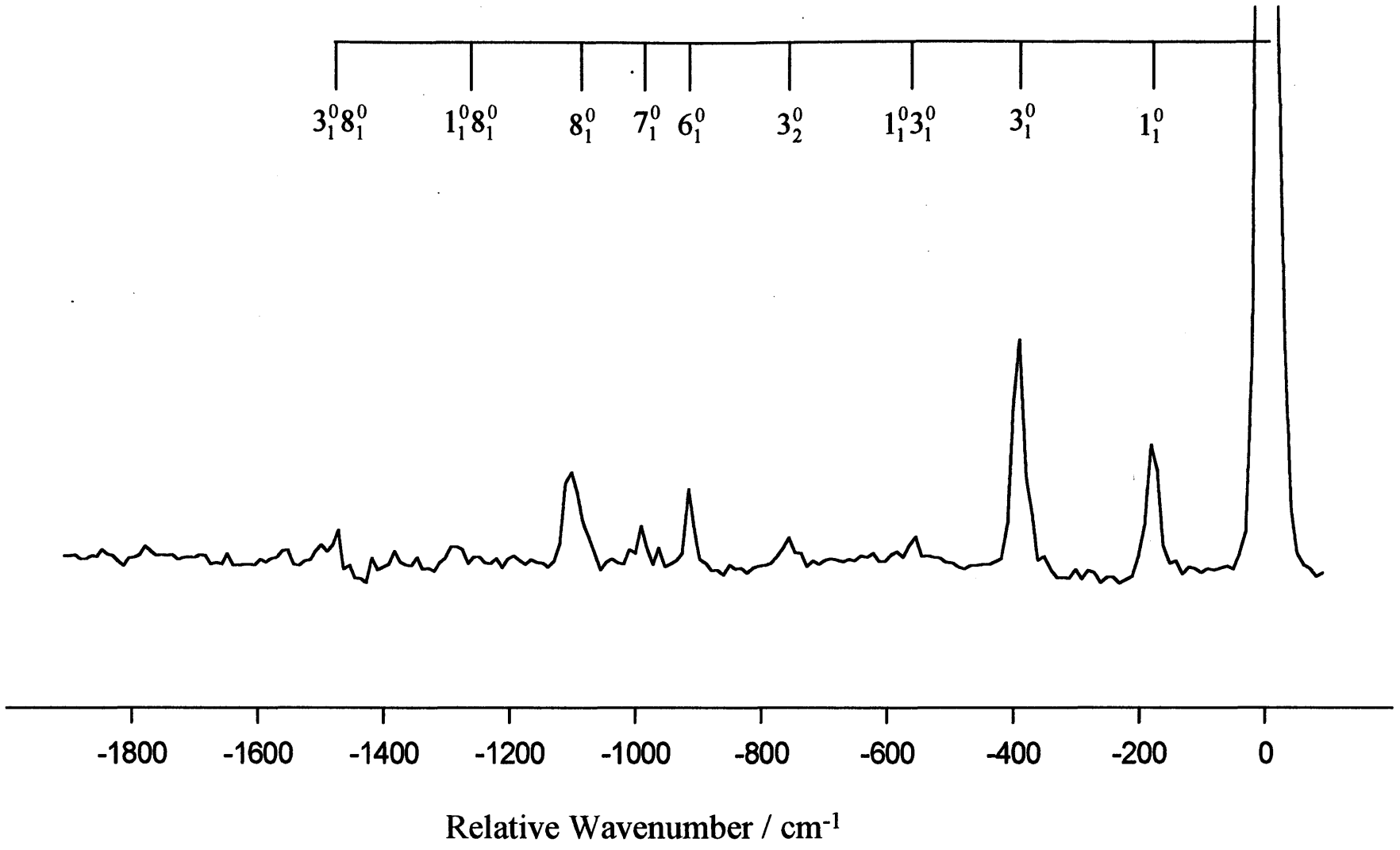

Figure 3.5 Dispersed fluorescence obtained by pumping the $\tilde{A}$ - $\tilde{X}$ 0_0^0 transition at 22515 cm^{-1}.

optically accessible electronic states lying close to the $\tilde{X}\,^2A'$ ground state, the additional structure can be attributed to vibrational excitation in the $\tilde{X}$ state. To assign this vibrational structure two sources are drawn upon for assistance, (i) comparison with $ZnCH_3$, and (ii) comparison with the *ab initio* predictions of Povey *et al.*[8]

If we make the reasonable assumption that the ZnC_2H_5 spectrum, like that of $ZnCH_3$, arises from a mainly metal-localised transition, then as a first approximation we need only consider those modes, particularly totally symmetric modes, for which the vibrational potential is significantly altered by this process. Thus, there would certainly be some activity in the Zn-C stretching mode expected and also possibly some in the Zn-C-C bend. Other modes, such as the C-C stretch, should play a lesser role in the vibrational structure because of their remoteness from the chromophore. Of course the description of the normal modes in terms of simple motions such as a C-C stretch is only meant to convey the dominant character of a vibration and should not be taken too literally.

Comparison with the *ab initio* data from reference 8 allows us to make some specific assignments. Table 3.2 and Figure 3.6 summarises the calculated harmonic vibrational frequencies of the ground electronic state of ZnC_2H_5. For reasons that will become clear later, interest is mainly in the low frequency modes in the molecule. Notice that the three lowest frequency modes are the Zn-C-C bend (ν_{11}), the methyl torsion (ν_{18}), and the Zn-C stretch (ν_{10}); of these ν_{11} and ν_{10} are totally symmetric.

The two bands immediately to the red of the laser wavelength in Figure 3.5 correspond to excitation of two relatively low frequency modes in the ground electronic state and the most obvious assignment is they arise from the Zn-C stretch (ν_{10}) and the Zn-C-C bend (ν_{11}). According to the *ab initio* results in Table 3.2, ν_{11} will have by far the lower frequency of these two modes. Consequently, the lowest frequency band in the dispersed fluorescence spectrum, which is 180 cm^{-1} to the red of the laser frequency, is most likely due to the Zn-C-C bending mode. The *ab initio* calculations predict a harmonic frequency of 196 cm^{-1} for this mode, a value

Table 5.2 Calculated[a] and observed vibrational frequencies of ZnC_2H_5.

Mode	Description[c]	Symmetry	Vibrational Frequencies[b] /cm^{-1}		
			$\tilde{X}$ state (*ab initio*)	$\tilde{X}$ state (expt)	$\tilde{A}$ state (expt)
ν_1	CH_3 stretch	a′	3203		
ν_2	CH_2 stretch	a′	3160		
ν_3	CH_3 stretch	a′	3145		
ν_4	CH_3 def.	a′	1595		
ν_5	CH_2 def.	a′	1559		
ν_6	CH_3 def.	a′	1515		
ν_7	CH_2/CH_3 wag (ip)	a′	1207	1109[d]	
ν_8	C-C stretch	a′	1058	987[d]	1011[d]
ν_9	CH_2/CH_3 wag (ap)	a′	992	915[d]	
ν_{10}	Zn-C stretch	a′	381	387	424
ν_{11}	Zn-C-C bend	a′	196	180	245
ν_{12}	CH_3 stretch	a″	3230		
ν_{13}	CH_2 stretch	a″	3201		
ν_{14}	CH_3 def.	a″	1604		
ν_{15}	CH_2/CH_3 twist (ap)	a″	1343		
ν_{16}	CH_2/CH_3 twist (ip)	a″	960		
ν_{17}	CH_2 rock	a″	600		
ν_{18}	CH_3 torsion	a″	231		

a) The *ab initio* calculations employed were at the Hartree-Fock UHF level using a DZP basis set. For more details see ref. 16.

b) Calculated vibrational frequencies are harmonic frequencies for the $\tilde{X}\,^2A'$ state. The experimental values for the $\tilde{X}$ and $\tilde{A}$ states are fundamentals.

c) The mode descriptions are approximate and are based on calculated atomic displacement vectors. According to the *ab initio* calculations the wagging, rocking and twisting motions of the CH_2 and CH_3 groups are heavily mixed. The abbreviations ip and ap refer to in-phase and anti-phase motions of the CH_2 and CH_3 groups.

d) Based on tentative assignments.

remarkably close to the observed interval. The only other mode expected to possess such a low frequency is the methyl torsion (ν_{18}). However, this can be eliminated from consideration for several reasons. First of all, since the methyl torsion has a'' symmetry, we would only expect transitions with Δv=even for this mode, making the effective vibrational interval of the order 500 cm^{-1}. This argument rests, of course, on the assumption that the 18_1^0 transition has not gained intensity by vibronic coupling. There are two further arguments that can be invoked. The first is the substantial difference between the *ab initio* frequency for ν_{18} and the observed vibrational interval. Secondly, we re-iterate the point made earlier, namely that because of the metal-localised nature of the electronic transition we would in any case expect some Franck-Condon activity in the Zn-C-C bend and there are no alternative candidates in the spectrum. Thus we can confidently assign the -180 cm^{-1} band to the Zn-C-C bending fundamental.

The more intense of the two low frequency bands, that at -387 cm^{-1}, is assigned to one quantum in the Zn-C stretch. The second member of the stretching progression, although quite weak, can also be identified in the spectrum, as shown in Figure 3.5. As in the case of the skeletal bend, the experimental frequency for the Zn-C stretch is quite close to the *ab initio* prediction (see Table 3.2).

There are other, weaker, bands in Figure 3.5 which cannot be attributed to either the Zn-C stretch or Zn-C-C bend or their combinations. In particular, there is a trio of bands covering the 900-1100 cm^{-1} range. Of the modes listed in Table 2, ν_7, ν_8, and ν_9 are all totally symmetric and may be responsible for these bands. Firm assignment of these is difficult, but very tentative assignments are shown in Figure 3.4 and in Table 2 based solely on the frequency order predicted from the *ab initio* calculations.

3.4.2 Implications for the assignment of the excitation spectrum

Dispersed fluorescence spectra have been recorded by laser excitation of a number of other vibronic transitions in addition to the origin. These data, which are collected together in Figures 3.6 and 3.7 confirm the assignment of the Zn-C stretching and Zn-C-C bending vibrational frequencies. They also provide valuable evidence which can

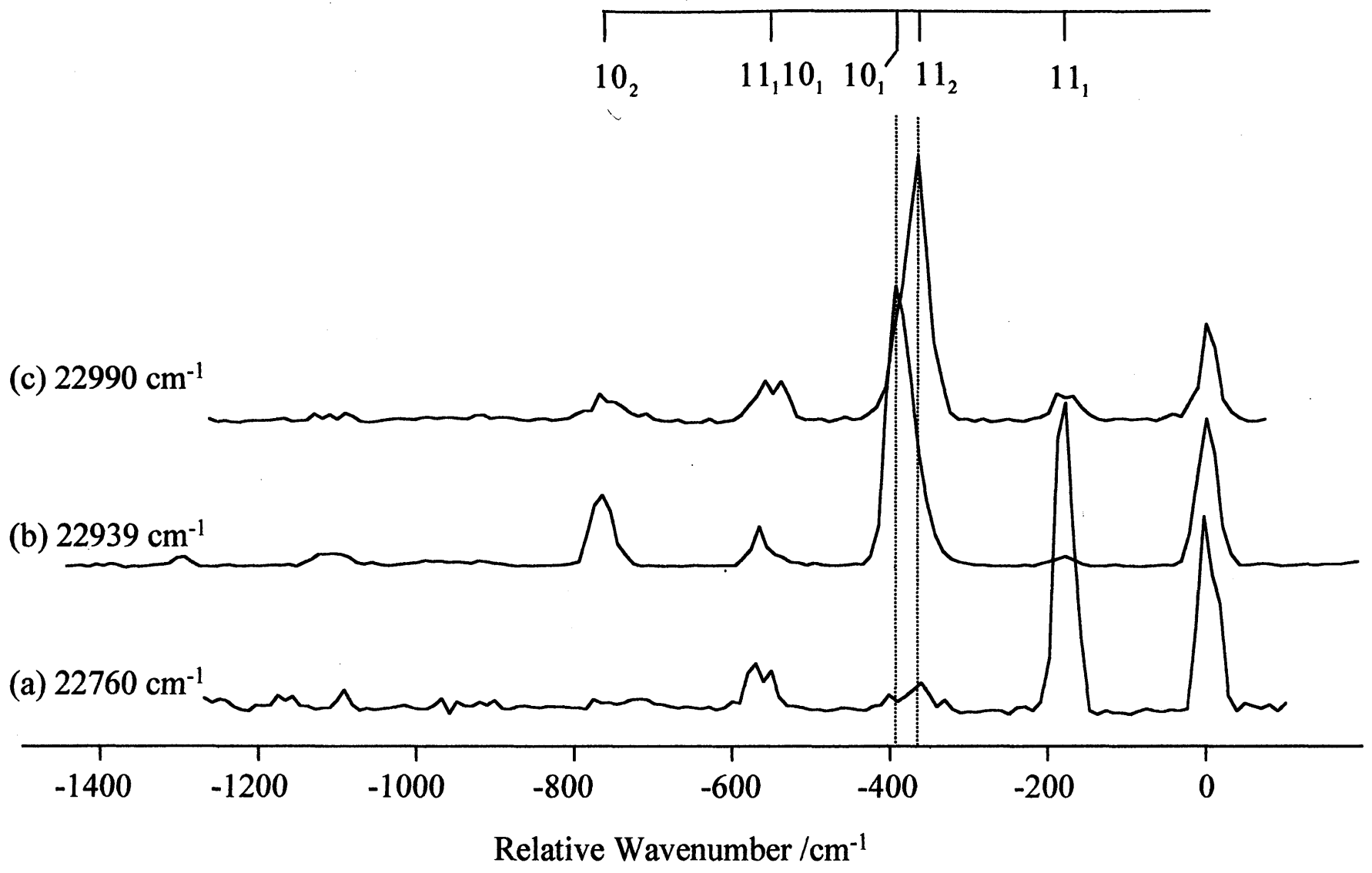

Figure 3.6 Dispersed fluorescence spectra recorded by pumping a number several different ZnC_2H_5 transsitions

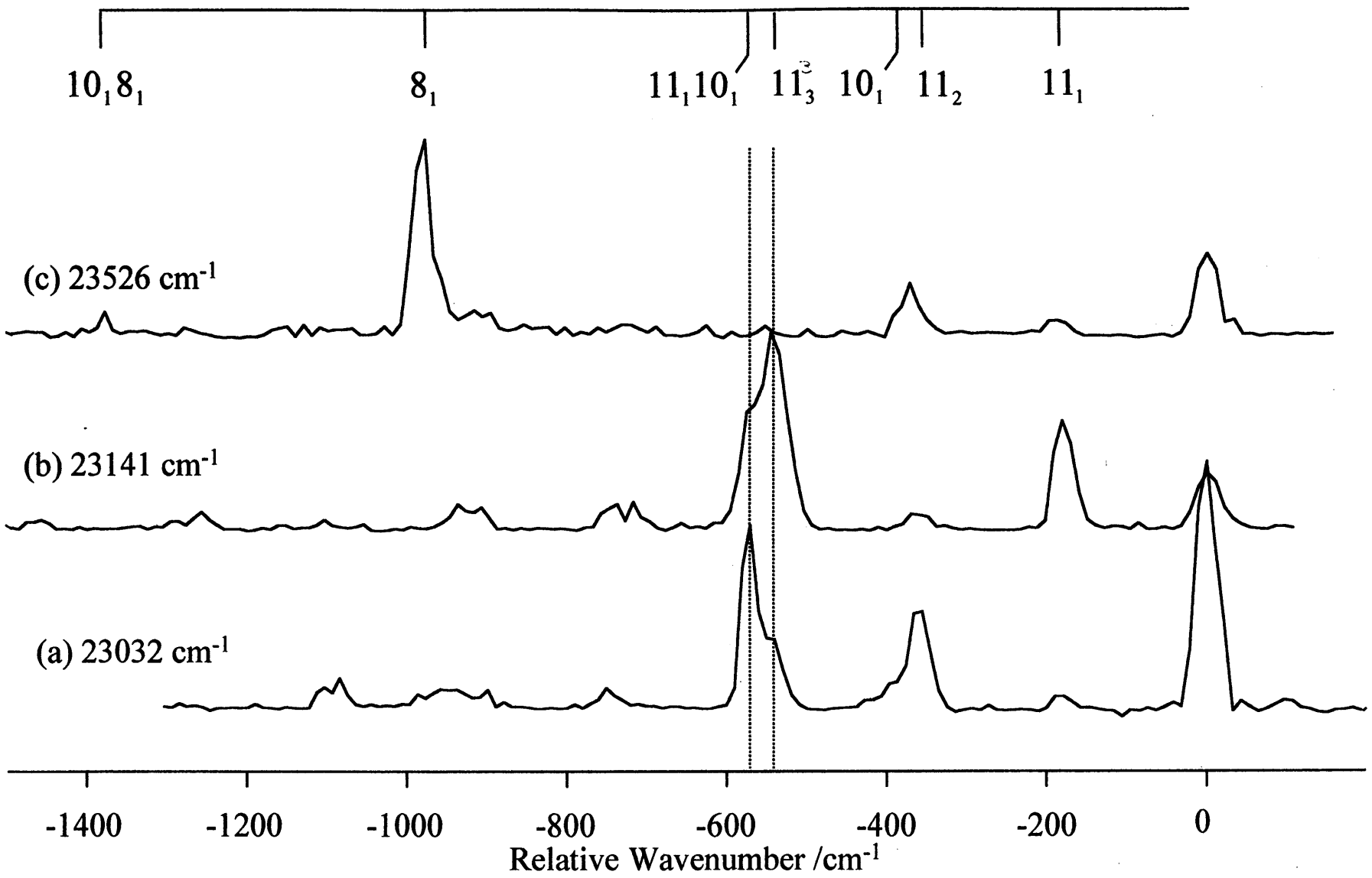

Figure 3.7 Dispersed fluorescence spectra recorded by pumping several different ZnC_2H_5 transitions

be used to assign several bands in the excitation spectrum. Before considering these, it should be borne in mind, particularly when dealing with bands in close proximity, that substantial vibronic interactions are likely especially in the upper vibronic states. The limited resolution of our experiments forces adoption of what may sometimes be simplistic assignments in terms of the dominant vibronic component. Each band will now be dealt with in turn.

3.4.3 22760 cm^{-1}

Figure 3.6(a) shows the dispersed fluorescence spectrum obtained by pumping the transition at 22760 cm^{-1} in the excitation spectrum. Two possible assignments for this transition were suggested by Povey,[8] namely that it is due either to the origin transition of a second ($\tilde{B}-\tilde{X}$) system, or it is due to excitation of the Zn-C-C bend in the $\tilde{A}$ state. The dispersed fluorescence spectrum in Figure 3.6(a) shows that the latter assignment is the correct one since a dramatic enhancement in one quantum of the bend in the ground electronic state is seen. The 11^1 level can therefore be located at 245 cm^{-1} above the zero point level in the $\tilde{A}$ state.

3.4.4 22939 and 22951 cm^{-1}

The strong transition at 22939 cm^{-1} yields a dispersed fluorescence spectrum (Figure 3.6(b)) which appears to be dominated by a progression in ν_{10}. The strongest band, which has been assigned to 10_1^1, could alternatively be due to 11_2^2. However, the latter assignment is unlikely given the substantial intensity of a second band at -758 cm^{-1}, which nicely fits as the second member in the stretching progression. Consequently, the 22939 cm^{-1} transition is assigned to excitation of one quantum of the Zn-C stretch in the $\tilde{A}-\tilde{X}$ manifold.

The transition slightly further to the blue in the excitation spectrum, that at 22951 cm^{-1}, appears almost as a shoulder on the stronger 22939 cm^{-1} band. The dispersed fluorescence spectrum obtained by pumping this band is indistinguishable from that shown in Figure 3.6(b) and so is not shown. Presumably, the similarity is caused by virtually complete collisional depopulation of the excited vibronic level to the nearby 10^1 level. Consequently the 22951 cm^{-1} band can not currently be assigned.

3.4.5 22990 cm^{-1}

The dispersed fluorescence spectrum shown in Figure 3.6(c) was obtained by exciting the 22990 cm^{-1} transition. At first sight it appears to be similar to that in 3.6(b), but in fact there are two important differences. First, a substantially weaker band is observed in the $2\nu_{10}$ region in Figure 6(b). Even more significantly, the strongest band is shifted some 15 cm^{-1} to the blue of the strongest band in Figure 3.6(b). Both of these factors indicate that the strongest feature in Figure 3.6(c) is not due to excitation of the Zn-C stretch and so we must find an alternative assignment. Using the frequency of the Zn-C-C bend, ν_{11}, in the ground electronic state deduced earlier, $2\nu_{11}$ would be expected at ~360 cm^{-1}, a value very close to the observed shift (-365 cm^{-1}) from the excitation wavelength in Figure (c). Thus the main peak in the dispersed fluorescence spectrum is assigned to excitation of $2\nu_{11}$ and the 22990 cm^{-1} band is assigned to the $\tilde{A}-\tilde{X}\ 11_0^2$ transition. This is consistent with the 11_0^1 assignment made earlier since it would give a 11^2-11^1 separation of 230 cm^{-1}, slightly smaller than the 11^1-11^0 value of 245 cm^{-1}. As shown in Figure 3.4, a plausible extrapolation of the ν_{11} progression in the excitation spectrum to the next member, 11_0^3, is also possible.

Before leaving the 22990 cm^{-1} band, it should be noted that expanded scans show that it is clearly broader than the surrounding bands in the excitation spectrum. Thus while the $\tilde{A}-\tilde{X}\,11_0^2$ transition may be the dominant contributor, there must be at least one further underlying transition, a point expanded upon in Chapter 5. The data in the present chapter is insufficient to assign this additional transition.

3.4.6 23032 cm^{-1}

The dispersed fluorescence spectrum obtained by laser excitation of the 23032 cm^{-1} transition is shown in Figure 3.7(a). The prominent bands are readily assignable in terms of structure in ν_{11} and ν_{10}. Interestingly, the strongest band is at the laser excitation wavelength, more than 85% of which is genuine emission rather than scattered laser light (established by tuning the laser to a nearby off-resonance wavelength and re-recording the spectrum). Given that the most intense emission is

back to the zero point level in the $\tilde{X}$ state, this suggests that the 23032 cm^{-1} transition may not involve a vibrationally excited upper electronic state and might instead be an electronic origin, presumably the $\tilde{B}-\tilde{X}$ origin. However, the observed vibrational structure, which shows apparent excitation of $2\nu_{11}$ and $\nu_{11} + \nu_{10}$, is difficult to explain if the $\tilde{B}-\tilde{X}$ 0_0^0 assignment is correct. Clearly this assignment should be regarded as tentative.

4.4.7 23141 cm^{-1}

The 23141 cm^{-1} band is a fairly weak band in the laser excitation spectrum of ZnC_2H_5. The corresponding dispersed fluorescence spectrum, shown in Figure 3.7(b), is consistent with the 23141 cm^{-1} band arising from a combination transition, the $11_0^1 10_0^1$ transition. The dispersed fluorescence spectrum shows prominent excitation of one quantum of the Zn-C-C bending vibration and its combination with one quantum in the Zn-C stretch.

3.4.8 23526 cm^{-1}

The final dispersed fluorescence spectrum to be considered is that shown in Figure 3.7(c), which was obtained by excitation of the medium intensity feature seen in the excitation spectrum at 23526 cm^{-1}. Excitation of this transition, which is 1011 cm^{-1} above the $\tilde{A}-\tilde{X}$ origin, gives rise to a strong band at -985 cm^{-1} in the dispersed fluorescence spectrum together with weaker features which are easily attributable to excitation of the Zn-C-C bend and Zn-C stretch. The 985 and 1011 cm^{-1} intervals presumably represent ground and excited state fundamentals in a particular mode. Furthermore, because of the considerable intensity of the 23526 cm^{-1} band in the excitation spectrum, there is clear evidence for a significant change in equilibrium geometry in the direction of the normal coordinate. From the *ab initio* calculations there are three totally symmetric modes which are contenders, two of which, the C-C stretch (ν_8) and the CH_2/CH_3 wag (ν_7), have predicted frequencies particularly close to the experimental values. Unfortunately, although the band is labelled as 8_0^1 in Figure 3.4, there is no convincing evidence to favour ν_8 over ν_7. Further work, perhaps using deuterated monoethyl zinc, is necessary to establish a firm assignment.

3.5 Bonding and structure

A number of conclusions can be drawn about the bonding and structure in ZnC_2H_5 from the combination of dispersed fluorescence data and new assignments of excitation transitions obtained in this work. The vibrational frequencies of the Zn-C stretching and Zn-C-C bending modes in both $\tilde{X}$ and $\tilde{A}$ states have now been established. As can be seen from Table 3.2, the stretching frequency increases from 387 to 424 cm^{-1} on excitation from the $\tilde{X}$ to the $\tilde{A}$ state. The same trend has previously been observed for $ZnCH_3$, the frequency rising from 445 cm^{-1} in the $\tilde{X}\,^2A_1$ state to 460 cm^{-1} in the $\tilde{A}\,^2E_{1/2}$ state.[7] The lowering of the Zn-C stretching frequency in moving from $ZnCH_3$ to ZnC_2H_5 is consistent with the increase in reduced mass being the dominant cause (in a crude calculation in which the methyl or ethyl group is treated as a point mass one expects a lowering of about 90 cm^{-1} while the actual lowering observed is 60 cm^{-1}). We are therefore led to the conclusion that the Zn-C force constants must therefore be, not surprisingly, very similar and this ties in with the known similarity in Zn-C bond dissociation enthalpies for $ZnCH_3$ and ZnC_2H_5.[14]

The observation of a progression in ν_{11} indicates that there may be a significant change in the Zn-C-C bond angle on electronic excitation to the $\tilde{A}$ state. However, caution is warranted in drawing this conclusion since there will inevitably be some coupling of the Zn-C stretching and Zn-C-C bending motions. Thus, while the increase in frequency of ν_{11} from 180 to 245 cm^{-1} on electronic excitation does suggest a stiffening in the bending coordinate, part of the frequency increase, and the Franck-Condon activity, may simply result from the inclusion of Zn-C stretching character in the mode. A rotationally-resolved study will be necessary to quantify the effect of electronic excitation on the molecular geometry.

3.6 Conclusions

The dispersed fluorescence spectra recorded in the present work have allowed ground electronic state vibrational frequencies of ZnC_2H_5 to be obtained. In addition, these data have made it possible to make assignments, some firm and others tentative, of

several bands in the excitation spectrum. The vibrational data that is now possessed provides some information on the bonding and structural changes on electronic excitation. However, it should be possible to obtain far more detailed information from rotationally-resolved spectra including an assignment of the upper state symmetry for each band. Such spectra have recently been recorded in the laboratory of T. A. Miller and preliminary analysis of these is detailed in Chapter 5.

3.7 References

1. C.F. Yu, F. Young, K. Tsukiyama, R. Bersohn, and J. Preses, *J. Chem. Phys.* **85**, 1382 (1986)
2. P.J. Young, R.K.Gosavi, J. Connor, O.P. Strausz and H.E. Gunning, *J. Chem. Phys.* **58**, 5280 (1973)
4. E.S.J. Robles, A.M. Ellis, and T.A. Miller, *Chem. Phys. Lett.* **178**, 185 (1991)
5. X.Q. Tan, T.M. Cerny, J.M. Williamson, and T.A. Miller, *J. Chem. Phys.* **101**, 6396 (1994)
6. T. Ibuki, A. Hiraya, and K. Shobatake, *J. Chem. Phys.* **92**, 2797 (1990)
7. R.L. Jackson, *J. Chem. Phys.* **96**, 5938 (1992)
8. I.M. Povey, A.J. Bezant, G.K. Corlett, and A.M. Ellis, *J. Phys. Chem.* **98**, 10427 (1994)
9. P.F. Seidler, *J. Phys. Chem.* **98**, 2095 (1994)
10. A.J. Bezant and A.M. Ellis, *J. Mol. Spec.*, in press
11. C. Jamorski and A. Dargelos, *Chem. Phys.* **164**, 191 (1992)
12. C.E. Moore, Atomic energy levels as derived from analysis of optical spectra, *Natl. Bur. Stand. Circ. US GPO,* Washington DC (1952)
13. T. Koenig, T. Balle andW. Snell, *J. Am. Chem. Soc.*, **97**, 662 (1975)
14 R. L. Jackson, *Chem. Phys. Lett.* **163**, 315 (1989)

Chapter Four

Development of the ASYMSR model

4.1 Introduction

Before considering the model used to simulate the rotationally resolved spectra of the zinc monoethyl radical, a brief reminder of the electronic structure of zinc monoalkyls is pertinent (a more detailed account was given in chapter 3). The lowest optically allowed transitions can be considered, very approximately, as excitation of a zinc 4*s* electron to zinc 4*p* orbitals. For the zinc monomethyl radical, which has C_{3v} point group symmetry, the p_x and p_y orbitals perpendicular to the Zn-C bond are degenerate giving rise a ^{2}E electronic state. In zinc monoethyl the symmetry is lowered to C_s which removes the degeneracy of the p_x and p_y orbitals so that the ^{2}E state in $ZnCH_3$ is resolved into two distinct states, one ^{2}A′ and one ^{2}A″, in ZnC_2H_5. The third 4*p* orbital, the $4p_z$ orbital, will give rise to another state at slightly higher energy. In $ZnCH_3$ this is the $\tilde{B}^2A_1$ state which has, so far, not been observed experimentally. In ZnC_2H_5 the corresponding state is the $\tilde{C}^2A'$ state.

Rotationally resolved LIF spectra of the $\tilde{A}^2E-\tilde{X}^2A_1\,0_0^0$ transitions of zinc and cadmium monomethyl radicals produced in a supersonic jet were recorded by Cerny *et al.*[1] in 1993. These spectra showed clear spin-orbit splitting in the excited electronic state of both molecules and the rotational structure within each spin-orbit component showed the classic '*-3B, -B, +B, +3B* ' structure expected for $^2\Pi$-$^2\Sigma$ or ^{2}E-^{2}A transitions when the orbitally degenerate excited state satisfies Hund's case (a). To deduce molecular constants from the spectra, a spectral simulation was performed. The effective rotational Hamiltonian for a ^{2}E state is

$$\mathcal{H}_{EFF} = \mathcal{H}_{ROT} + \mathcal{H}_{SO} + \mathcal{H}_{COR} + \mathcal{H}_{SR} + \mathcal{H}_{JT} \qquad (1)$$

where $\mathcal{H}_{ROT}$, $\mathcal{H}_{SO}$, $\mathcal{H}_{COR}$, $\mathcal{H}_{SR}$, and $\mathcal{H}_{JT}$ are, respectively, the standard rotational, spin-orbit, Coriolis, spin-rotation, and Jahn-Teller terms.[1] The effective Hamiltonian for the $^2A_1$ state is much simpler because the projection of the total orbital angular momentum, L, upon the z axis, L_z, is zero. Thus the terms $\mathcal{H}_{SO}$, $\mathcal{H}_{COR}$, and $\mathcal{H}_{JT}$ are not present in the Hamiltonian for the ground electronic state.

Zinc-containing radicals might be expected to bear considerable resemblance to calcium-containing radicals: both metals possess an s^2 outer shell electronic configuration. The main difference between zinc- and calcium-containing free radicals is that the 3*d* shell is completely full in the former while completely empty in the latter. Two molecules that have been studied at high resolution and that are useful for comparison to monoethyl zinc are $CaNH_2$ and CaSH.[2-6] In both of these molecules the equilibrium molecular symmetry is too low to allow orbital degeneracies in the excited electronic states. The ground electronic state is predominantly a Ca 4*s* orbital while the first three optically accessible excited states arise from the three different 4*p* orbitals localised primarily upon the calcium atom. Clearly, this is very similar to the situation proposed above for ZnC_2H_5 so the comparison is potentially very useful. $CaNH_2$ has been the most extensively studied, particularly with regard to spin-rotation interactions, while CaSH shares the same molecular point group, C_s, with ZnC_2H_5.

Rotationally-resolved spectra of the $\tilde{A}^2B_2 - \tilde{X}^2A_1$, $\tilde{B}^2B_1 - \tilde{X}^2A_1$ and $\tilde{C}^2A_1 - \tilde{X}^2A_1$ transitions of $CaNH_2$[2-4] and the $\tilde{A}^2A' - \tilde{X}^2A'$ and $\tilde{B}^2A'' - \tilde{X}^2A'$ transitions of CaSH have been recorded.[5,6] These showed that $CaNH_2$ is planar with C_{2v} symmetry in the ground electronic state and its three lowest electronic excited states. Likewise CaSH maintains C_s symmetry in the corresponding electronic states. In both molecules the first three excited electronic states are close in energy and as stated previously arise from the three 4*p* orbitals. Molecular rotation can potentially couple certain of these states together. The resulting spin-rotation interaction could be rather large because the interacting states are close in energy. Experiments have shown this to be the case.[2-6]

This chapter describes the development of a computer program to simulate rotational spectra for asymmetric top molecules which includes a Hamiltonian that describes spin-rotation interactions. Although other research groups have already developed comparable simulation packages the advantage of developing a new program is that it gives the author, or others within the Leicester spectroscopy group, the flexibility to readily modify the program, *e.g.* for the inclusion of extra terms in the Hamiltonian. As will be seen in Chapter 5, where the rotationally resolved spectra of

ZnC_2H_5 are shown and analysed, it will become clear that further modifications to the program will be necessary to accurately simulate some of the spectra.

4.2 The spectral simulation program: SpecSim

Rotationally-resolved spectra of ZnC_2H_5 have been simulated using an asymmetric top model incorporating spin-rotation interactions. The simulation starts by taking an estimated set of spectroscopic constants and a quantum mechanical model and uses this to generate a spectrum. The simulated spectrum is then compared to the real spectrum and, if they differ significantly, a new estimate of the molecular constants is made and the process begins again. This iterative comparison with the real spectrum, which is a standard procedure in spectroscopy,[7] is achieved in an automated manner using a non-linear least squares fitting process.

The overall computer program used for simulating the rotationally resolved spectra is known as SpecSim and was written by S. Panov at the Ohio State University. Within the framework of this program, a model for asymmetric top molecules with spin-rotation was written by the author and incorporated as an option in SpecSim. This sub-program is described in this chapter and is referred to as the ASYMSR model.

4.2.1 SpecSim

Many computer programs have been written for simulating the rotational structure in the spectra of molecules. Some of these have highly specialised applications, *e.g.* for dealing specifically with asymmetric tops, symmetric rotors, etc. Because these are often highly individual programs it can be difficult to adapt them to other applications. However, many of the tasks carried out by spectral simulation programs are not dependent upon the particular model, *e.g.* inputting trial rotational constants, measuring line positions, diagonalising the Hamiltonian matrix, least squares fitting processes, plotting spectra, etc. The SpecSim program was designed to separate essential but spectroscopically uninteresting parts of the program from the parts that are model-dependent. The model-dependent parts, namely defining the basis set, setting up the Hamiltonian matrix, and calculating the intensities of all possible transitions, are defined in a separate part of the program which is then linked

to the main program. Several model-dependent parts can be stored under the SpecSim banner and so it is easy to switch from one model to another.

As well as combining as many functions as possible into a model-independent program, SpecSim was designed to provide a user-friendly platform for spectral simulations. The programme was written in C++, which is an object-orientated language, to run in a Windows environment. Included in the C++ package are important sections of code for the construction of menus, dialogue boxes, and mouse functions which are utilised by SpecSim. The object-orientated nature of C++ means that all of the program functions and related options can be accessed by clicking a mouse on toolbar buttons or through pull-down menu systems. The C++ language is also designed to allow the construction of a Help database that can be accessed by mouse or keyboard. In addition, the Windows environment provides a convenient format for outputting simulated spectra, where the simulations are plotted with the experimental data for ease of comparison. Included as part of the SpecSim program are four graphical manipulation tools, namely zoom, line position measurements, lateral spectral movement and a line assignment tool.

At the time the author started work on the analysis of the rotationally-resolved ZnC_2H_5 spectrum, a basic asymmetric rotor model was available in SpecSim. However this model did not include spin-rotation coupling which, as will be seen later, is vital for ZnC_2H_5. Consequently, a new model needed to be developed and this is detailed in the remainder of this chapter.

4.2.2 The ASYMSR model

As the model is part of the SpecSim program it is essential that the information is in a SpecSim compatible format. The model is compiled as a dynamically-linked library file (*.dll file), that the main SpecSim programme accesses to find all the model-dependent data. The way in which the programme works is as follows. There are 21 functions that make up each model. In order for SpecSim to be compatible with all models each function must exist in each model even if not relevant to that particular model. For many of the functions the code may require trivial, or even no, changes from one model to the next. For example the function 'Name', unsurprisingly, merely requires a suitable model name to be returned. On the other

hand, some functions require extensive reprogramming. The two functions that require the most programming and are the most involved parts of any model are 'Hamilt' and 'Inten'. The 'Hamilt' returns an array which contains all of the elements of the Hamiltonian matrix for a given state. The matrix is then diagonalised by the main programme to give a series of energy levels. These are then read into the 'Inten' function which determines the relative intensities of all possible transitions between energy levels. The next two sections describe the theoretical basis from which the 'Hamilt' and 'Inten' functions have been programmed.

4.3 Hamiltonian

The electronic ground state of ZnC_2H_5 is a $^2A'$ state, while the first two optically accessible excited electronic states are, as discussed earlier, expected to be a $^2A'$ and a $^2A''$ state. As none of these states has net orbital angular momentum the effective rotational Hamiltonian is

$$\mathcal{H} = \mathcal{H}_{ROT} + \mathcal{H}_{SR} \tag{2}$$

The two terms in (2) are now considered in more detail.

4.3.1 Rotational Hamiltonian ($\mathcal{H}_{ROT}$)

The rotational Hamiltonian for an asymmetric top molecule is[7]

$$\mathcal{H}_{ROT} = AN_z^2 + BN_x^2 + CN_y^2 \tag{3}$$

assuming the rigid rotor approximation. A, B and C are rotational constants defined in the usual way. $\boldsymbol{N}$ is the total angular momentum excluding electron spin, *i.e.*

$$\boldsymbol{N}=\boldsymbol{J}-\boldsymbol{S} \tag{4}$$

where $\boldsymbol{J}$ is the total angular momentum (excluding nuclear spin) and $\boldsymbol{S}$ is the electron spin angular momentum. N_x, N_y and N_z are the Cartesian components of $\boldsymbol{N}$.

To account for non-rigidity, centrifugal distortion terms must be added to $\mathcal{H}_{ROT}$, *i.e.*

$$\begin{aligned}\mathcal{H}_{CD} = -\big(&D_N N^4 + D_{NK} N^2 N_z^2 + D_K N_z^4 \\ &+ \partial_N N^2 2\big(N_x^2 - N_y^2\big) + \partial_K \big\{\big(N_x^2 - N_y^2\big)N_z^2 + N_z^2\big(N_x^2 - N_y^2\big)\big\}\big)\end{aligned} \tag{5}$$

4.3.2 Spin-rotation Hamiltonian ($\mathcal{H}_{SR}$)

The first detailed theoretical description of spin-rotation interactions was given by Van Vleck.[9] He derived the form of the quadratic (second-order) spin-rotation Hamiltonian (ignoring centrifugal distortion) to be

$$\mathcal{H}_{SR}^{(2)} = \frac{1}{2}\sum_{\alpha\beta} \varepsilon_{\alpha\beta}\big(N_\alpha S_\beta + S_\beta N_\alpha\big) \tag{6}$$

where α and β run over the molecule-fixed principal inertial axes *a*, *b* and *c*. The spin-rotation constants, $\varepsilon_{\alpha\beta}$, form a second-rank tensor which has six unique components in the general case. Brown and Sears[10] showed that for a molecule with C_s symmetry this reduces to five independent components giving an effective Hamiltonian of

$$\begin{aligned}\mathcal{H}_{SR}^{(2)} = &\varepsilon_{aa} N_a S_a + \varepsilon_{bb} N_b S_b + \varepsilon_{cc} N_c S_c + \\ &\tfrac{1}{2}\big(\varepsilon_{ab} + \varepsilon_{ba}\big)\big(N_a S_c + S_c N_a + N_c S_a + S_a N_c\big).\end{aligned} \tag{7}$$

The above Hamiltonian ignores quartic and higher terms in the spin-rotation coupling; these are expected to be small for the zinc monoethyl radical and are neglected in this model. A detailed description of quartic terms can be found in the paper by Brown and Sears.[10]

4.4 Matrix Elements

The rotational and spin-rotation terms in equations (4), (5), (6) and (7) are cast in a form convenient for diagonalisation in a Hund's case (b) basis set, $|J,N,K,S\rangle$. In Hund's case (b) (see Figure 4.1) there is either no orbital angular momentum or, if there is orbital angular momentum, the spin-orbit coupling is weak. Consequently ***S***

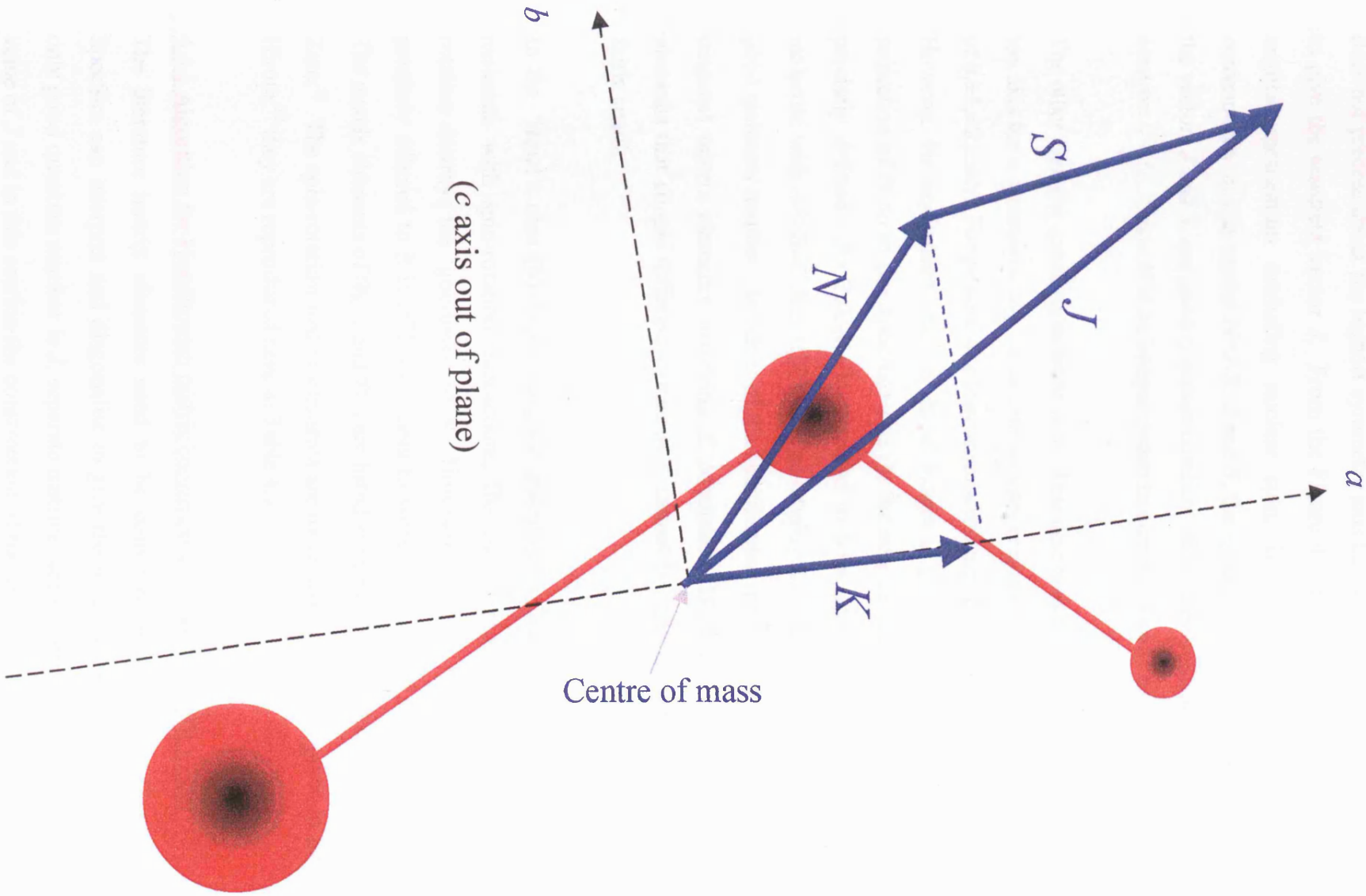

Figure 4.1: Coupling of angular momenta in Hund's case (b) for a hypothetical triatomic molecule

does not precess about the highest symmetry axis but instead is coupled directly to N to give the resultant vector J. From the Figure 4.1 it can be seen that J, the total angular momentum excluding nuclear spin, is defined as $J=N+S$ or more conveniently in this model $N=J-S$. J and S, the quantum numbers corresponding to the vectors J and S, are good quantum numbers. For a free-radical with one unpaired electron $S = ½$. Since N is an integer quantum number, J must be half-integer.

The other case (b) quantum number is K. This describes the projection of N onto the top axis for a symmetric top. K is also an integer quantum number and takes values of $0,\pm1,\pm2....\pm N$. For prolate or oblate symmetric tops K is a good quantum number. However for asymmetric tops K is no longer a good quantum number, *i.e.* the projection of N on to the a-inertial axis (in the near prolate limit) can no longer be precisely defined. As ZnC_2H_5 is expected to be a near-prolate asymmetric rotor molecule with $A>>B\approx C$ it is still useful to employ K even though it is not strictly a good quantum number. In terms of the Hamiltonian matrix of $\mathcal{H}_{ROT}$ this means that diagonal matrix elements involving K dominate. However, off-diagonal matrix elements that couple different values of K cannot be ignored even though they are fairly small.

In the Hund's case (b) limit N a good quantum number. In an asymmetric top molecule with spin-rotation interactions, the coupling of the spin to molecular rotation destroys the 'goodness' of N. However, although Hund's case (b) is not precisely adhered to it is still convenient to work with a Hund's case (b) basis set. The matrix elements of $\mathcal{H}_{ROT}$ and $\mathcal{H}_{CD}$ are listed in many places including the book by Zare.[11] The spin-rotation matrix elements are more involved but are given in full by Hirota;[12] they are reproduced here in Table 4.1.

4.4.1 Algorithm for Hamiltonian matrix construction in the ASYMSR model

The literature matrix elements need to be converted into a matrix format that SpecSim can interpret and diagonalise to give the rotational energy levels. As the only good quantum number is J, separate matrices are constructed for each possible value of J and in this section the construction of the matrix for J = ½ (see Table 4.2) is considered as a simple illustrative example. In general, N can take on the values

SPECIAL NOTE

THIS ITEM IS BOUND IN SUCH A MANNER AND WHILE EVERY EFFORT HAS BEEN MADE TO REPRODUCE THE CENTRES, FORCE WOULD RESULT IN DAMAGE

Table 4.1: The matrix elements included in the asymmetric top with spin-rotation model (from reference 12)

$$\langle KJ|\hat{H}|NKJ\rangle = \left(A-\tfrac{1}{2}(B+C)\right)K^2+\tfrac{1}{2}(B+C)\times N(N+1)\ -D_K K - D_K K^3 - D_K K$$
$$+D_{JK}K^2N(N+1)-D_J N^2(N+1)^2$$
$$-\left[\varepsilon_{aa}K^2+\frac{(\varepsilon_{bb}+\varepsilon_{cc})}{2}\times\left(N(N+1)-K^2\right)\right]\frac{\left[N(N+1)+\tfrac{3}{4}-J(J+1)\right]}{2N(N+1)}$$

$$\langle K+1J|\hat{H}|NKJ\rangle = \tfrac{1}{2}D_x\times\sqrt{(J-K)(J+K+1)}-\frac{\left[N(N+1)+\tfrac{3}{4}-J(J+1)\right](2K+1)}{4N(N+1)}$$
$$\times\sqrt{N(N+1)-K(K+1)}\,\frac{(\varepsilon_{ab}+\varepsilon_{ba})}{2}$$

$$\langle K+2J|\hat{H}|NKJ\rangle^{a} = \left[\tfrac{1}{4}(B-C)-\tfrac{1}{2}K\ K^2(K+2)^2 - SD_J N(N+1)\right.$$
$$\times\sqrt{\left[N(N+1)-(K(K-1)\right]\left[N(N+1)-(K-1)(K-2)\right]}$$
$$-\left\{\frac{N(N+1)+\tfrac{3}{4}-J(J+1)}{4N(N+1)}\times\sqrt{\left[N(N+1)-K(K+1)\right]\left[N(N+1)-(K+1)(K+2)\right]}\right.$$
$$\left.\left.\times\frac{(\varepsilon_{bb}-\varepsilon_{cc})}{2}\right\}\right]$$

$$\langle K-1KJ|\hat{H}|NKJ\rangle = -\left[\varepsilon_{aa}-\frac{(\varepsilon_{bb}+\varepsilon_{cc})}{2}\right]\times\sqrt{N^2-K^2}\times\frac{K}{2N}$$

$$\langle K-1K+1J|\hat{H}|NKJ\rangle = -\left\{\frac{N+2K+1}{4N}\right\}\times\frac{(\varepsilon_{ab}+\varepsilon_{ba})}{2}\times\sqrt{(N-K)(N-K-1)}$$

$$\langle K-1K+2J|\hat{H}|NKJ\rangle = -\frac{1}{4N}\times\sqrt{(N-K-1)(N+K+1)(N-K-2)(N-K)}\times\frac{\varepsilon_{bb}-\varepsilon_{cc}}{2}$$

[a] Element incorrect in reference 12, corrected by author.

Table 4.2 The Hamiltonian matrix for J=1/2 (excluding centrifugal distortion terms).

		N=1		
J=1/2	N=0			
	K=0	K= -1	K=0	K= 1
N=0 K=0	0	0	0	0
K= -1	0	$A+\frac{(B+C)}{2}$ $-\frac{1}{2}\left\{\varepsilon_{aa}+\frac{\varepsilon_{bb}+\varepsilon_{cc}}{2}\right\}$	$-\frac{\sqrt{2}}{8}(\varepsilon_{ab}+\varepsilon_{ba})$	$\frac{1}{2}(B-C)$
N=1 K=0	0	$-\frac{\sqrt{2}}{8}(\varepsilon_{ab}+\varepsilon_{ba})$	$B+C$ $-\frac{1}{2}(\varepsilon_{bb}+\varepsilon_{cc})$	0
K= 1	0	$\frac{1}{2}(B-C)$	0	$A+\frac{(B+C)}{2}$ $-\frac{1}{2}\left\{\varepsilon_{aa}+\frac{\varepsilon_{bb}+\varepsilon_{cc}}{2}\right\}$

J+½ or J-½ for a spin doublet state; for the case where J=½, this means N=0 or 1. As K is the projection of N onto the a-axis its magnitude can not exceed that of N, so the quantum number K can have values of -N. -N+1, ... +N. These possibilities result in a (4J+2)×(4J+2) matrix (4×4 for J=½).

As mentioned earlier, for an asymmetric top with no spin-rotation N is a good quantum number and hence the purely rotational terms are diagonal in N. Also as stated earlier, K is not a good quantum number and matrix elements exist which couple K to K±1 and K to K±2 in the asymmetric non-rigid rotor. The matrix elements involving spin-rotation terms can couple basis functions off-diagonal in N by ΔN=±1, but in addition there are diagonal (ΔN=0) spin-rotation terms.

4.5 Transition Intensities

The intensity of a transition is calculated in the 'inten' section of the model. The formulae used to calculate intensities were derived from those given by Brown, Bowater and Carrington.[13] More recently Tan *et al.*[14] have used a similar approach and their expressions are compared to those derived here. The intensity of a given transition can be factored into two parts, the line strength, which is considered below, and a Boltzmann factor to account for the population of the lower energy level (this will depend heavily upon the rotational temperature).

An expression for the line strength $S_{J'J''}$ can be derived from expressions employed by Brown, Bowater and Carrington[13] for elucidating the Stark effect in an asymmetric rotor. Since symmetries of the Stark and electric dipole operator are formally equivalent, it is trivial to obtain a general expression for the line strength. Brown *et al.*[13] gave their Stark effect expression in terms of an irreducible spherical tensor notation in order to amplify the role of symmetry in their treatment. Accordingly, a spherical tensor notation has also been employed here giving:

$$S_{J'J''} = \left[(-1)^{N'+S+J''+1} \times \left[(2J'+1)(2J''+1)\right]^{1/2} \begin{Bmatrix} N' & J' & S \\ N'' & J'' & 1 \end{Bmatrix} \right. \\ \left. \times \sum_q T_q^1(\mu) (-1)^{N'-K'} \left[(2N'+1)(2N''+1)\right]^{1/2} \begin{pmatrix} N' & 1 & N'' \\ -K' & q & K'' \end{pmatrix} \right]^2 \quad (8)$$

where the term within $\{\ \}$ is a Wigner 6-*j* symbol while the last term is a Wigner 3-*j* symbol (see, for example, Zare[11]). $T_q^1(\mu)$ is the spherical tensor form of the dipole moment operator.

The Wigner 3-*j* and 6-*j* symbols are convenient ways of representing the coupling of two commuting angular momenta. Wigner 3-*j* symbols are closely related to the well-known Clebsch-Gordon coefficients and libraries for calculating both of these quantities are included in SpecSim. Similarly, there is also a routine in SpecSim, for evaluating 6-*j* symbols. The following simple relationship exists between Glebsch-Gordon coefficient and 3-*j* symbols:[11]

$$\begin{pmatrix} j_1 & j_2 & j_3 \\ m_1 & m_2 & m_3 \end{pmatrix} \equiv (-1)^{j_1 - j_2 - m_3} (2j_3 + 1)^{-1/2} \langle j_1 m_1, j_2 m_2 | j_3 - m_3 \rangle \tag{9}$$

where j_i is the magnitude of the vector $\boldsymbol{j}_i$ and m_i is the projection of the vector on space fixed axis.

Using well-known relationships for 3-*j* symbols given by Zare,[11] equation (9) can be rewritten in a form more suitable for comparison with the line strength expression reported by Tan *et al.*,[14] *viz*

$$\begin{pmatrix} j_1 & j_2 & j_3 \\ m_1 & m_2 & m_3 \end{pmatrix} \equiv (-1)^{j_1 + j_2 + j_3} \begin{pmatrix} j_3 & j_2 & j_1 \\ m_3 & m_2 & m_1 \end{pmatrix} \tag{10}$$

Hence the 3-*j* symbol in equation (8) can be rewritten as

$$\begin{pmatrix} N' & 1 & N'' \\ -K' & q & K'' \end{pmatrix} \equiv (-1)^{N' + 1 + N''} \begin{pmatrix} N'' & 1 & N' \\ K'' & q & -K' \end{pmatrix} \tag{11}$$

and this can be used with equation (9) to obtain:

$$\begin{pmatrix} N' & 1 & N'' \\ -K' & q & K'' \end{pmatrix} \equiv (-1)^{N'+1+N''+N''-1+K'} (2N'+1)^{-1/2} \langle N''K'',1q|N'K' \rangle \quad (12)$$

Substituting (12) into equation (8) gives, after a few simple algebraic manipulations,

$$S_{J'J''} = \left[(-1)^{N'+S+J''+1} \left[(2J'+1)(2J''+1) \right]^{1/2} \begin{Bmatrix} N' & J' & S \\ N'' & J'' & 1 \end{Bmatrix} \times \sum_q T_q^1(\mu) (2N''+1)^{1/2} \langle N''K'',1q|N'K' \rangle \right]^2 \quad (13)$$

The asymmetric rotor wavefunctions for the upper and lower electronic states, $|\tau'N'M'\rangle$ and $|\tau''N''M''\rangle$ respectively, where τ labels the electronic state, can be expanded as a linear combination of symmetric rotor basis functions, *i.e.*

$$\begin{aligned} |\tau'' N''M''\rangle &= \sum_{K''} a_{\tau''K''} |N''K''M''\rangle \\ |\tau' N'M'\rangle &= \sum_{K'} a_{\tau'K'} |N'K'M'\rangle \end{aligned} \quad (14)$$

Thus, finally, we obtain the following

$$S_{J'J''} = \left[(-1)^{N'+S+J''+1} \left[(2J'+1)(2J''+1) \right]^{1/2} \begin{Bmatrix} N' & J' & S \\ N'' & J'' & 1 \end{Bmatrix} \times \sum_{K'} \sum_{K'} \sum_q a^*_{\tau'K'} a_{\tau''K''} T_q^1(\mu) (2N''+1)^{1/2} \langle N''K'',1q|N'K' \rangle \right]^2 \quad (15)$$

This line strength expression is now in a form that can used in the intensity part of the asymmetric top with spin-rotation model. A similar expression was derived by Tan *et al.*[14] for their study of the ethoxy radical but there is a phase error in their expression.

The dipole moment operator, $T_q^1(\mu)$, in equation (15) has the components listed in Table 4.3 below:

Table 4.3: Defining the dipole moment operator in terms of components along principal axes

$T_q^1(\mu)$	Cartesian form
$T_0^1(\mu)$	μ_a
$T_1^1(\mu)$	$\frac{-1}{\sqrt{2}}(\mu_b + i\mu_c)$
$T_{-1}^1(\mu)$	$\frac{1}{\sqrt{2}}(\mu_b - i\mu_c)$

For a transition with a dipole moment directed along the *a* axis (a-type transition), only the $T_0^1(\mu)$ operator needs to be considered to calculate transition intensities. As shown in Table 4.3, this is equivalent to the cartesian form μ_a. Transitions of *a*-type are often referred to as 'parallel' transitions. However, *b*-type and *c*-type transitions which are often referred to as 'perpendicular' transitions because the transition moment is approximately orientated perpendicular to the *a* axis in a near-prolate asymmetric top, contain both $T_1^1(\mu)$ and $T_{-1}^1(\mu)$ in the intensity expression. The intensity of a hybrid transition, whose dipole moment is not restricted to any one principal inertial axis, can be calculated from an appropriatly weighted sum of the intensities for each principal component.

In the simple metal-localised picture of the electronic transitions of zinc monoalkyl free radicals, the first two excited states of ZnC_2H_5 correspond to excitation of the unpaired electron from an s-like orbital to p_x and p_y orbitals on the zinc atom. In our choice of axes, the p_y orbital is directed perpendicular to the plane defined by the Zn-C-C framework. A transition to this $^2A''$ state from the $\tilde{X}^2A'$ ground state will be pure *c*-type. The p_x orbital on the other hand will lie in the Zn-C-C plane. The low symmetry of the molecule means that a transition from the $\tilde{X}^2A'$ state to the $4p_x$ orbital, which gives a $^2A'$ excited state, will be an *a/b* hybrid transition. In other words, the transition will have a mixture of parallel and perpendicular character. However, in practice this transition is expected to be mainly *b*-type with a small amount of *a*-type character mixed in, *i.e.* it will be strongly dominated by perpendicular character.

4.5.1 Selection rules

Equation (15) describes the line strength for a transition and for a transition to be allowed the line strength must be non-zero. Equation (15) is a multiplication of a number of factors and if any of these factors are zero then the transition is forbidden. The two factors that give rise two the selection rules are the Wigner 6-*j* symbol, $\begin{Bmatrix} N' & J' & S \\ N'' & J'' & 1 \end{Bmatrix}$, and the Clebsch-Gordon co-efficient $\langle N''K'',1q|N'K'\rangle$ or equvalently the Wigner 3-*j* symbol $\begin{pmatrix} N' & 1 & N'' \\ -K' & q & K'' \end{pmatrix}$. In his book, Zare[7] considers the conditions in which the Wigner 6-*j* and 3-*j* symbol are non-vanishing and determines the selection rule for *J* from the Wigner 6-*j* symbol to be:

$$\Delta J = 0,\pm 1$$

As *N* is defined as *J*+½ and *J*-½ the selection rules for *N* in the general case must be:

$$\Delta N = 0,\pm 1,\pm 2$$

In the limit that *N* is a good quantum number $|\Delta N|>1$ transitions are forbidden (essentially because the line strength reduces to a single 3-*j* symbol). This may appear to cause some difficulties but the problems are circumvented as *N* as a bad quantum number. A state nominally labelled as *J,N* will, through the off-diagonal matrix elements have contributions from the *J,N*-1 or the *J,N*+1 level. Consequently, transitions with $\Delta N=\pm 2$ are possible.

The selection rules for *K* are dictated by the triangulation condition $K'-K''=q$, which must be obeyed for the Clebsch-Gordon coefficient in equation (15) or the Wigner 3-*j* symbol in equation (8) to be non-zero (see Zare[11] p284). This gives selection rules for *K* which can be used to simplify equation (15). As *q* is different for *a*-, *b*-, and *c*-type transitions the selection rules for each are:

a-type transitions	$K'=K''$
b-type transition	$K'=K''-1$ (for $q=-1$) or $K'=K''+1$ (for $q=+1$)
c-type transition	$K'=K''-1$ (for $q=-1$) or $K'=K''+1$ (for $q=+1$)

Equation (15) includes the dipole moment operator, $T_q^1(\mu)$ but as only the relative rather than the absolute intensities of lines are important for the work described in

this thesis the absolute transition moment is of no consequence. μ is therefore assumed to be constant and arbitrarily set at unity. Including this with the selection rules for K into equation (15) gives the specific line strengths for *a*-, *b*-, and *c*-type transitions below:

4.5.1.1 *a*-type

For an *a*-type transition q=0 and $K'=K''$ and so equation (15) simplifies to:

$$S_{J'J''} = [(2J'+1)(2J''+1)](2N''+1)\left[(-1)^{N'+S+J''+1}\begin{Bmatrix} N' & J' & S \\ N'' & J'' & 1 \end{Bmatrix} \times \sum_{K''} a^{*}_{\tau' K'} a_{\tau'' K''} \langle N''K'', 10 | N'K'' \rangle \right]^2 \quad (16)$$

4.5.1.2 *b*-type

For *b*-type transitions only terms for which $q = \pm 1$ exist, giving

$$S_{J'J''} = \frac{(2N''+1)}{2}[(2J'+1)(2J''+1)]\left[(-1)^{N'+S+J''+1}\begin{Bmatrix} N' & J' & S \\ N'' & J'' & 1 \end{Bmatrix} \times \left| \sum_{K'} \sum_{K''} a^{*}_{\tau' K'} a_{\tau'' K''} \langle N''K'', 1-1 | N'K' \rangle - \sum_{K''} \sum_{K'} a^{*}_{\tau' K'} a_{\tau'' K''} \langle N''K'', 11 | N'K' \rangle \right| \right]^2 \quad (17)$$

This can be simplified to a summation over a single variable using the fact that K'-$K''=q$, *i.e.* when q=-1 then $K'=K''$-1, and when q=1 then $K'=K''$+1.

$$S_{J'J''} = \frac{(2N''+1)}{2}[(2J'+1)(2J''+1)]\left[(-1)^{N'+S+J''+1}\begin{Bmatrix} N' & J' & S \\ N'' & J'' & 1 \end{Bmatrix} \times \left| \sum_{K''} a^{*}_{\tau' K''-1} a_{\tau'' K''} \langle N''K'', 1-1 | N'K''-1 \rangle - \sum_{K'} a^{*}_{\tau' K''+1} a_{\tau'' K''} \langle N''K'', 11 | N'K''+1 \rangle \right| \right]^2 \quad (18)$$

4.5.1.3 *c*-type

c-type transitions are very similar to *b*-type as again $q=\pm 1$ and $K'=K''-1$ (for $q=-1$) or $K'=K''+1$ (for $q=+1$) giving

$$S_{J'J''} = \frac{(2N''+1)}{2}[(2J'+1)(2J''+1)]\left[(-1)^{N'+S+J''+1}\begin{Bmatrix} N' & J' & S \\ N'' & J'' & 1 \end{Bmatrix}\right.$$
$$\times\left|\sum_{K''} a^{*}_{\tau' K''-1} a_{\tau'' K''} \langle N''K'',1-1|N'K''-1\rangle\right. \qquad (19)$$
$$\left.\left.+\sum_{K'} a^{*}_{\tau' K''+1} a_{\tau'' K''} \langle N''K'',11|N'K''+1\rangle\right|\right]^2$$

The only difference between (18) and (19) is that in the former the summations over K are subtracted whereas in the latter they are added.

To obtain relative intensities, the line-strengths must be multiplied by the Boltzmann factor $e^{-(E-E_0)/kT}$ which defines the population of the lower state with energy E relative to the state of lowest energy, E_0.

4.5.2 Algorithm for the relative intensity calculations in the ASYMSR model

Using the ASYMSR model, which is programmed in C++, the starting point in a simulation is the calculation of the energy levels. These are then sorted into energy order by the main SpecSim program. For each level, starting with that of lowest energy, the program consideres transitions to all of the calculated energy levels in the excited electronic state, although for most the intensity will be zero. The 'Inten' routine is called to calculate the transition intensity for each possible transition.

Initially, the line strength for each transition is set at zero before the selection rules are considered and as the selection rules, mainly that referring to K, are dependent upon the type of transition, the *a*-type transitions are considered separately from the *b*- and *c*-type transitions. As J is the only good quantum number the first task performed by the 'inten' routine is to deduce all possible combinations of N and K for a given J, *i.e.* $N=J\pm½$ and $K=-N, -N+1,...+N$. This is done for both the upper and lower states for the transition under consideration and then the overall line strength

for a transition calculated. This calculation consists of sum of the line strengths calculated for every posible combination of N and K. All combinations must be considered as both N and K are bad quantum numbers so no single expression will give the correct line strength for a transition. To do this the 'inten' routine contains a series of loops so that transitions between every allowed combination of N and K quantum numbers are considered.

An *a*-type transition is the easiest to deal with since the ΔK=0 selection rule applies and thus equation (15) reduces to a single summation over K, *i.e.* equation (16). The selection rules are considered as a set of nested IF loops; in the outer loop the ΔJ=0, ±1 selection rule is considered, with an inner loop considering the ΔK selection rule. At the centre of each loop is the line strength calculation so for a transition that does not obey any of the selection rules the line strength will remain at zero. Both *b*- and *c*-type transitions are calculated in the same part of the model due to the similarity of equations (17) and (18) and the routine used works in much the same way as that described above for *a*-type transitions, except that now the ΔK selection rules are slightly more complicated as is the line strength expression (see section 4.5.1).

4.6 Model Testing

Before the model was used to simulate the zinc monoethyl spectra discussed in chapter 5 it was first necessary to test the model to ensure that the matrix elements and the intensity formulae were correctly programmed. The model was tested by comparing simulated spectra with real spectra and with published simulations. It is actually more useful to compare with the latter as real spectra may contain perturbations and intensity fluctuations that would not be accounted for in our model. Of course simulated spectra generated by different simulation programs which use exactly the same Hamiltonian, intensity formulae, and molecular constants, should yield exactly the same spectra.

4.6.1 Asymmetric top

The simplest test was to simulate a spectrum with all of the spin-rotation constants set to zero, *i.e.* simulating a pure asymmetric top, and comparing this with the

simulated spectrum generated using the same constants in an existing asymmetric rotor program. The reference asymmetric top model used was that written by Panov and already included as part of the SpecSim package. ZnC_2H_5 as the test molecule was chosen and the rotational constants used for the ground electronic state were taken from a Hartree-Fock *ab initio* calculation reported by Povey *et. al.*[15]; and the excited state constants are an arbitrary set with similar magnitudes. The table below (Table 4.4) lists the constants used in this test:

Table 4.4: Rotational constants (cm^{-1}) used in the asymmetric top test

Constant	Lower state	Upper state
A	1.0250	1.0890
B	0.1225	0.1195
C	0.1134	0.1180

Figure 4.2 shows the simulated spectra from both models for *a*-, *b*- and *c*-type transitions. Excellent agreement is clearly obtained in each case. The slight differences between the two simulations arise from the different way that the maximum value of *J* is calculated. In the asymmetric top model *J* is the principle quantum number so a maxium value of *J* is used to limit mathematical calculations. In the ASYMSR model the principle quantum number is now *N* which is equivilent to *J* in the limit of no spin-rotation interaction but, as it is not a good quantum number it cannot be used to limit the length of calculations. Instead a maxium *J* is used that produces no difficulties in using the model but accounts for the slight differences in Figure 4.2.

4.6.2 $CaNH_2$

$CaNH_2$ is an asymmetric top free radical which may undergo spin-rotation interactions. The similarity of its electronic structure to that of zinc-containing free radicals, discussed much earlier in this chapter, makes $CaNH_2$ a particularly interesting candidate for simulation using the ASYMSR model. There are, of cource, some differences between ZnC_2H_5 and $CaNH_2$. One notable difference is the higher symmetry (C_{2v}) of $CaNH_2$ which means that only the diagonal spin-rotation constants ε_{aa}, ε_{bb}, and ε_{cc}, can be non-zero for $CaNH_2$.[4] Clearly, comparison of the ASYMSR

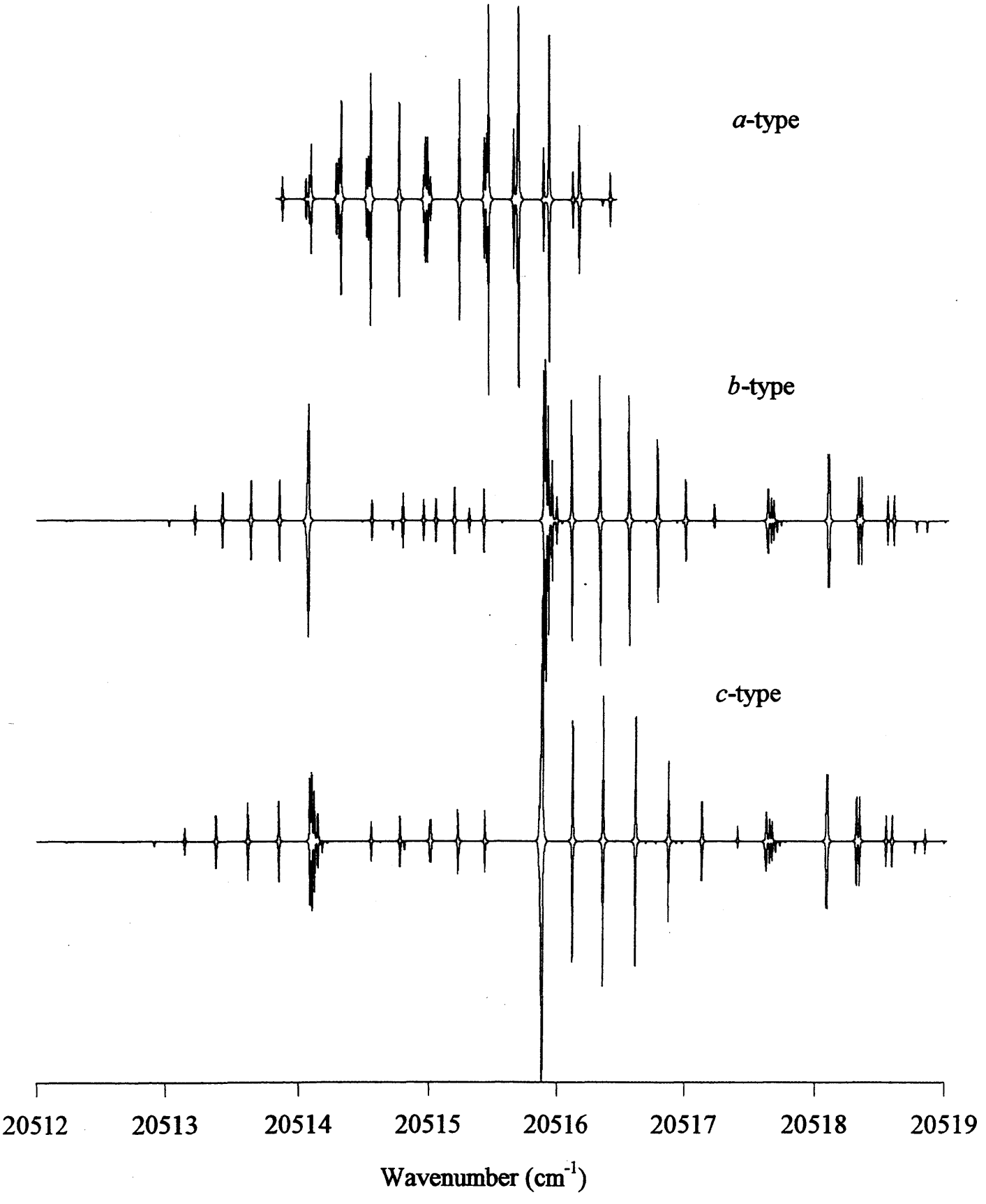

Figure 4.2 : Comparison of simulations for ASYMSR model (lower spectrum) versus pure asymmetric top model (upper)

model with published rotationally-resolved spectra of $CaNH_2$ will provide a good test of those matrix elements involving the diagonal spin-rotation constants, ε_{aa}, ε_{bb}, and ε_{cc}, but not of the matrix elements involving the off-diagonal spin-rotation constants ε_{ab}, and ε_{ba}.

Recently Marr *et. al.*[2] published a portion of the rotationally-resolved spectrum of the K'=0-K''=1 sub-band of the $\tilde{A}^2B_2 - \tilde{X}^2A_1\ 0_0^0$ electronic transition of $CaNH_2$ and performed a successful analysis. The rotational constants determined from their analysis are listed in Table 4.5. As has already been noted earlier in this Chapter, K is not a good asymetric top quantum number. However, it is close to being a good quantum number in $CaNH_2$ and so the labelling of a sub-band as K'=0-K''=1, although not strictly valid, is a useful approximation.

Figure 4.3 shows a comparison of the real and simulated spectra reported by Marr *et. al.*[2] with a simulation generated by the ASYMSR model. As can be seen, the agreement between the two simulations is excellent (the apparent differences in line positions are due to slightly different plotting scales). When comparison is made between the line positions tabulated by Marr[2] and those generated by the ASYMSR model the agreement is within 0.005 cm^{-1} in every case. It should be noted that the extent of the Q_{11} and Q_{22} branches are artificially shortened in both of the simulations to minimise the time taken for matrix diagonalisation.

Table 4.5: Spectroscopic constants (cm^{-1}) of the $\tilde{X}^2A_1$ and the $\tilde{A}^2B_2$ states of $CaNH_2$ (taken from ref 2)

Constant	$\tilde{X}^2A_1$	$\tilde{A}^2B_2$
A	13.0574	11.4487
B	0.30047	0.3071
C	0.29288	0.2992
ε_{aa}	0	8.238
ε_{bb}	0.0011	0.0052
ε_{cc}	0.0011	0.0557

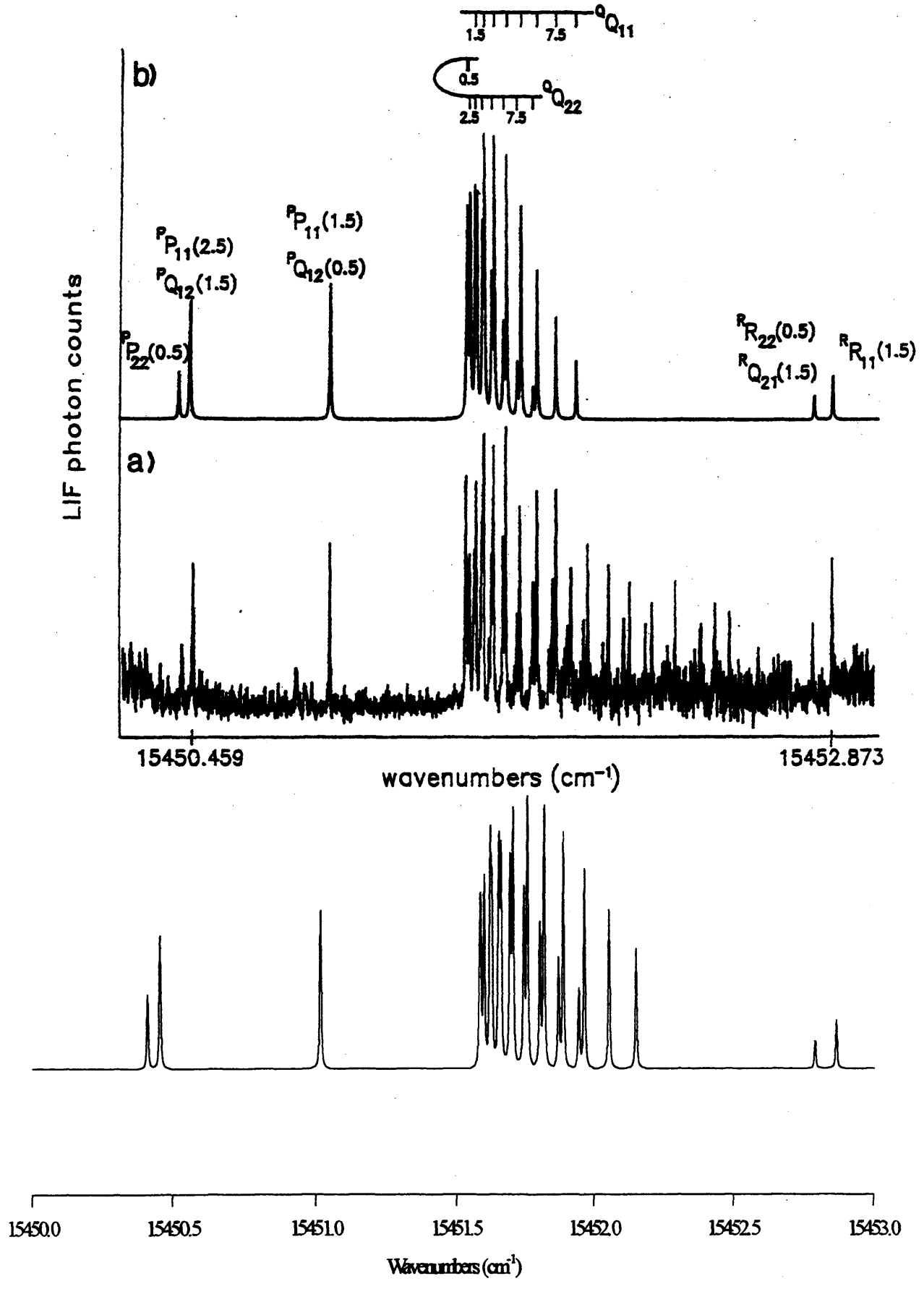

Figure 4.3 Simulated and experimental spectrum of $CaNH_2$ from reference 2 (upper) compared to spectrum simulated using asymmetric top with spin-rotation model (lower)

4.6.3 CaSH

The analysis of rotationally resolved LIF spectra of the $\tilde{A}^2A'-\tilde{X}^2A'$ and $\tilde{B}^2A''-\tilde{X}^2A'$ transitions of CaSH has been reported in the literature.[5,6] CaSH, like ZnC_2H_5, is an asymmetric top free radical with C_s symmetry which can undergo spin-rotation interactions; indeed these have been reported to be quite large. The Hamiltonian employed by both Jarman[5] and Scurlock[6] is the same as that used in the ASYMSR model so comparison between their real and simulated spectra and our own simulation should provide a further useful test. Scurlock *et al.* published portions of the $K'=0$-$K''=1$ and the $K'=1$-$K''=0$ sub-bands of the $\tilde{B}^2A''-\tilde{X}^2A'0_0^0$ transition (*c*-type) of CaSH. The rotational constants reported by Scurlock[6] are listed in Table 4.6. As can be seen the values of ε_{ab} and ε_{ba} were found to be less than the experimental error. Consequently CaSH is a poor test of the matrix elements involving ε_{ab} and ε_{ba}.

Comparison of our simulated spectra with the CaSH spectra reported by Scurlock has two advantages over the previous test on $CaNH_2$. Firstly, the values of ε_{cc} and particularly ε_{bb} are larger for CaSH then $CaNH_2$ (see Table 4.6) so any errors in the matrix elements involving these constants are likely to be magnified. Secondly, Marr only published real and simulated spectra for the $K'=0$-$K''=1$ sub-band of $CaNH_2$ for which no excited state spin-rotation splitting due to ε_{aa} is possible.

The large spin-orbit-like splitting that is observed in some of the sub-bands in rotationally resolved spectra of asymmetric zinc- and calcium- containing free radicals arises due to a spin-rotation interaction that couples the spin of the unpaired electron, to rotation motion about the *a* inertial axis. This phenomenom is discussed in greater detail in Chapter 5. Suffice it to say for the moment that the magnitude of the observed splitting is, to a first approximation equal to $\varepsilon_{aa}K$.

The spectrum of the $K'=1$-$K''=0$ sub-band of CaSH reported by Scurlock *et al.*[6] shows spin-orbit-like spin-rotation splitting of ~6 cm^{-1}. Thus comparison of the real and simulated spectra reported by Scurlock[6] with a simulation generated using the ASYMSR model provides a good test for the Hamiltonian matrix elements involving

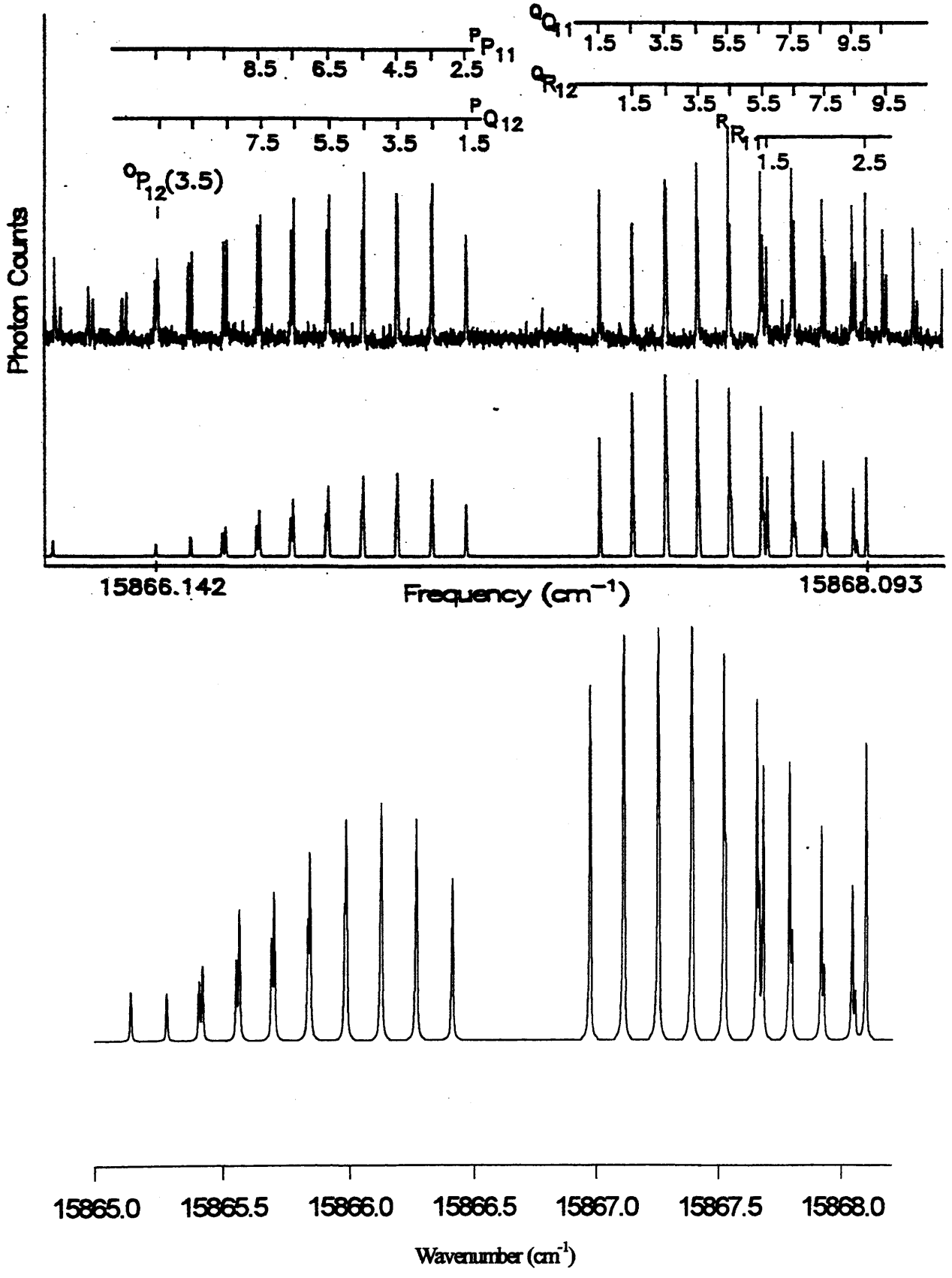

Figure 4.4 The upper two spectra, taken from reference 6, show simulated and experimental LIF spectra of part of the $K'=1$-$K''=0$ subband of the $\tilde{A}$ - $\tilde{X}$ transition of CaSH. The lower spectrum is a simulation using the ASYMSR model.

ε_{aa}. Figure 4.4 shows the simulated spectrum generated by the AYSMSR model (using the constants from Table 4.6) and the real and simulated spectra of CaSH reported by Scurlock.[6] Notice that this shows only one of the spin doublet transitions, the other is some 6 cm^{-1} to the blue. Again there is excellent agreement between Scurlock's spectra and the simulation from this work, with slight differences being due to the different plotting scales.

Table 4.6: Molecular constants(cm^{-1}) for the $\tilde{X}^2A'$ and $\tilde{B}^2A''$ electronic states of CaSH (from ref 4.6)

Constant	$\tilde{X}^2A'$	$\tilde{B}^2A''$
A	9.69322	10.43356
B	0.1411865	0.14343
C	0.1395809	0.14114
ε_{aa}	0	-5.7793
ε_{bb}	0.001593	0.10767
ε_{cc}	0.0011836	0.03270
ε_{ab}	0	0
ε_{ba}	0	0

4.7 Conclusions

A new model, referred to as ASYMSR, has been developed for the spectra simulation program SpecSim for predicting the rotational and spin-rotation structure in the electronic spectra of asymmetrc top free-radicals. Test calculations have been performed on $CaNH_2$ and CaSH to check whether the program is error-free. These tests were carried out successfully and so it now seems that ASYMSR should be suitable for simulating, and fitting, the high resolution LIF spectra of ZNC_2H_5. This is the subject matter of much of the next chapter.

References

1 T.M. Cerny, X.Q. Tan, J.M. Williamson, E.S.J. Robles, A.M. Ellis and T.A. Miller, *J. Chem. Phys.I*, **99**, 12 (1993)

2 A.J. Marr, M. Tanimoto, D. Goodridge, and T.C. Steimle, *J. Mol. Spectrosc.*, **176**, 268 (1996)

3 C.J. Whitham, and C.H. Jungen, *J. Chem. Phys.*, **93**, 2 (1990)

4 C. Zhao, P.G. Hajigeorgiou, P.F. Bernath, and J.W. Hepburn, *J. Mol. Spectosc.*, **176**, 268 (1996)

5 C.N. Jarman, and P.F.Bernath, *J. Chem. Phys.***98**, 9 (1993)

6 C.T. Scurlock, T. Henderson, S. Bosely, K.Y. Jung, and T.C. Steimle, *J. Chem. Phys.*, **100**, 15 (1994)

7 K. Rao, *Molecular spectroscopy Modern Res., Vol II,* 1-65, Academic Press (1969)

8 I. Panov , *Ph.D. thesis,* Ohio State University (1997)

9 J.H. Van Vleck, *Rev. Mod. Phys.*, **23**, 213 (1951)

10 J.M. Brown and T.J. Sears, *J. Mol. Spectrosc.*, **75**, 111 (1979)

11 R.N Zare, *Angular momentum, understanding spaitial aspects in chemistry and physics,* John Wiley and Sons, (1988).

12 E. Hirota, *High-Resolution Spectroscopy of Transient Molecules,* Springer series in Chemical Physics, Springer, Berlin (1985)

13 I.C. Bowater, J.M. Brown, and A. Carrington, *Proc. R. Soc.*, **333**, 265 (1973)

14 X.Q. Tan, T.M. Cerny, J.M. Williamson and T.A. Miller, *J. Chem. Phys.*, **101**, 6396 (1994)

15 I.M. Povey, A.J. Bezant, G.K. Corlett, and A.M. Ellis, *J. Phys. Chem.*, **98**, 10427 (1994)

Chapter Five

High resolution spectroscopy of ZnC_2H_5

5.1 Introduction

The work on zinc monoethyl described in Chapter 3 was at resolution that only allowed determination of electronic and vibrational structure. Furthermore, although some firm and some tentative assignments of this structure were made, the low resolution work raises as many questions as it answers. There is clearly need for further information on ZnC_2H_5; and so in this Chapter we turn to rotationally-resolved LIF spectra.

Rotationally-resolved LIF of the related molecules, $ZnCH_3$ and $CdCH_3$, were recorded by Cerny *et al.*[2] in 1993. The transition observed in both cases was the $\tilde{A}^2E$-$\tilde{X}^2A_1$ transition. In their work Cerny determined a variety of spectroscopic constants, including the *A* and *B* rotational constants and, for the $\tilde{A}^2E$ state the spin-orbit coupling constant. The rotational constants were used to estimate equillibrium geometries of the two radicals.

By analogy with $ZnCH_3$ and $CdCH_3$, it is expected that ZnC_2H_5 will posses two close-lying electronic states, a $^2A'$ and a $^2A''$ state, which correlate with the $\tilde{A}^2E$ state in the metal monomethyls. Rotationally-resolved studies of theses states could provide a number of important pieces of information:

(i) Allow a determination of which excited state has the lower energy, the $^2A'$ or the $^2A''$, since the rotational structure should reveal the symmetry of the excited state.

(ii) Assist in the assignment of the vibronic structure seen in the low resolution spectra reported in Chapter 3.

(iii) Provide information on the equilibrium geometries in the ground and excited electronic states.

(iv) Reveal details of the spin-rotation interactions. This is particularly interesting prospect for the excited states since, in addition to the $^2A'$ and $^2A''$ states correlating with the $\tilde{A}^2E$ state in $ZnCH_3$, the $\tilde{C}^2A'$ state should also be nearby. Interactions between these states are expected to produce some

fascinating behaviour, which, as well as being of interest in its own right, should also provide further insight into the electronic structure of ZnC_2H_5.

5.2 Experimental

The jet-cooled rotationally-resolved LIF spectra of ZnC_2H_5 described in this chapter were recorded by C. Carter and R. Rubino in the laboratory of Professor T. A. Miller at the Ohio State University. Figure 5.1 shows a schematic diagram of the overall experiment set-up in the Miller laboratory. In contrast to the low resolution work described in Chapter 3, for which ZnC_2H_5 was made by an electrical discharge of $Zn(C_2H_5)_2$, the Miller group produced the radical by excimer laser photolysis of $Zn(C_2H_5)_2$. The diethyl zinc precursor, which is commercially available, was seeded in a high pressure (150-200 psig) buffer gas of either helium or a helium/neon mixture (70% Ne and 30% He), before supersonic expansion. A General Valve series 9 pulse valve, with a 0.5 mm orifice was used for the supersonic jet expansion source Photolysis took place just beyond the nozzle exit.

Probing of radicals occurred ~20 mm downstream from the photolysis region. The probe laser was a ring dye laser system operating with coumarin 440 dye(Exciton, Inc.); this was pumped by 5W multiline UV from an Innova 200 Ar^+ laser. The ring dye laser output was typically 100-300 mW, with a manufacturer's stated linewidth of a few MHz. The LIF was collected and collimated by a quartz, 2.5 cm focal length, f/1 lens and the collimated light then passed through a O-ring sealed quartz window and was focused through adjustable optical slits by a 15 cm focal length, f/3 quartz lens. The fluorescence was recorded by a EMI 9659QB photomultiplier tube (PMT) with cut-off filters being used to eliminate scattered laser light. The slits were adjusted so that fluorescence from only a narrow, ~300 μm, central region of the jet was imaged on the PMT to decrease the Doppler-width of the spectra lines. The signal from the PMT was pre-amplified and then sent to a Stanford Research Model 250 Boxcar for integration. The Boxcar output was then acquired with the Coherent Autoscan system for signal processing.

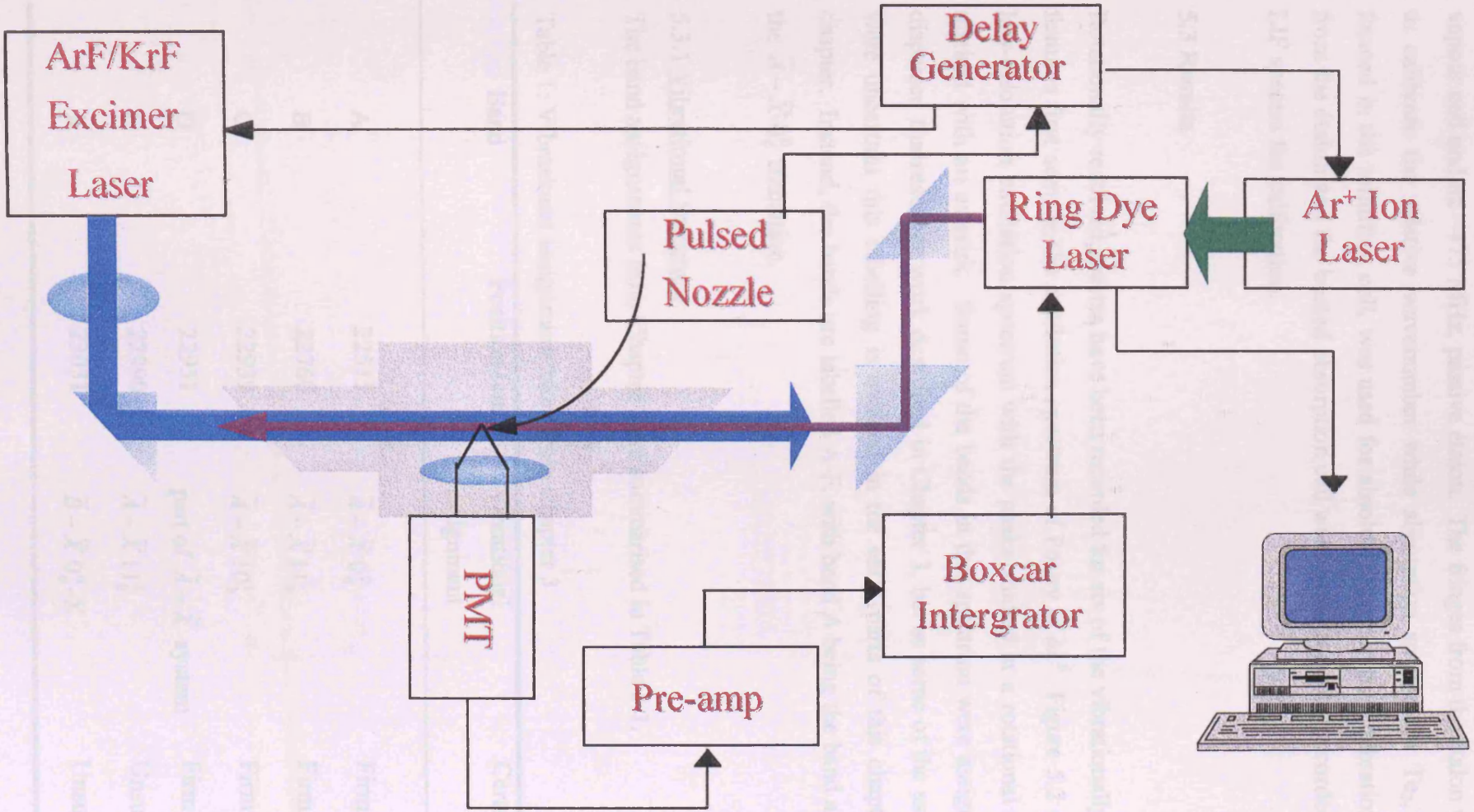

Figure 5.1: Schematic diagram of the experimental apparatus used by the Miller group to record the rotationally resolved spectra of ZnC_2H_5.

Calibration was achieved by directing a portion of the cw probe laser to a tellurium vapour cell and an ~475 MHz, passive étalon. The fringes from the étalon were used to calibrate the relative wavenumber while absorption spectra for Te_2, which is formed in the tellurium cell, was used for absolute wavenumber calibration. Signals from the étalon and the heated absorption cell were simultaneously recorded with the LIF spectra for calibration.

5.3 Results

Rotationally resolved spectra have been recorded for six of the vibrationally-resolved features first seen in the excitation spectrum of Povey *et al.*[5] Figure 5.2 shows the low-resolution excitation spectrum with the peaks studied at a rotational resolution marked with an asterisk. Some of the bands in this spectrum were assigned in the dispersed fluorescence work described in Chapter 3, but as some of the assignments were uncertain this labelling is avoided in the early parts of this chapter in this chapter. Instead, the bands are labelled A-F, with band A being the band assigned to the $\tilde{A}-\tilde{X}\,0_0^0$ transition.

5.3.1 Vibrational Structure

The band assignments from Chapter 3 are summarised in Table 5.1.

Table 1: Vibrational assignment taken from Chapter 3

Band	Position (cm^{-1})	Vibrational assignment	Certainty
A	22515	$\tilde{A}-\tilde{X}\,0_0^0$	Firm
B	22760	$\tilde{A}-\tilde{X}\,11_0^1$	Firm
C	22939	$\tilde{A}-\tilde{X}\,10_0^1$	Firm
D	22951	part of $\tilde{A}-\tilde{X}$ system	Firm
E	22990	$\tilde{A}-\tilde{X}\,11_0^2$	Unsure
F	23031	$\tilde{B}-\tilde{X}\,0_0^0$-X	Unsure

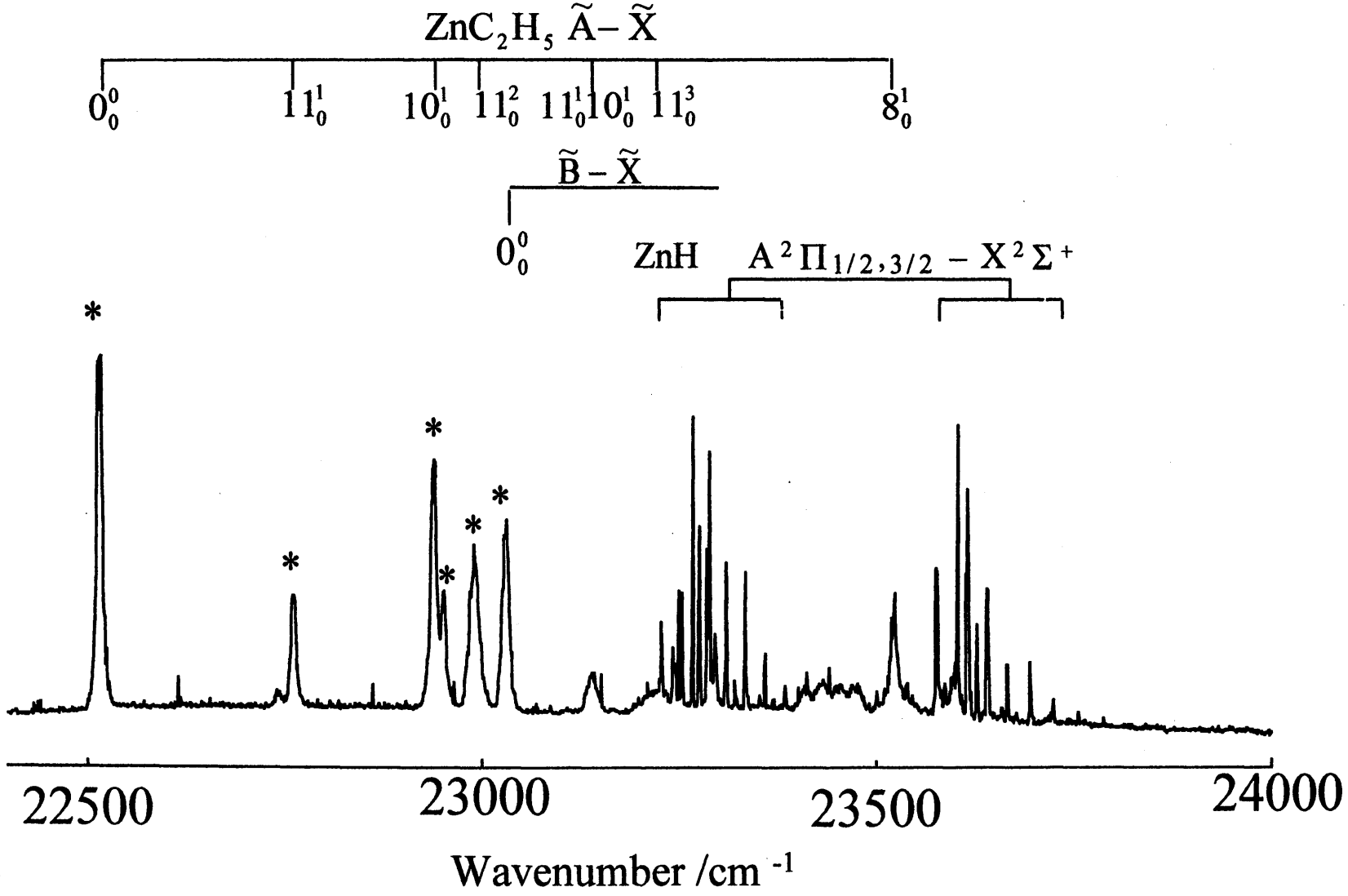

Figure 5.2 ZnC_2H_5 excitation spectrum

Table 5.1 also shows the approximate position of each band and the degree of confidence in the assignment.

The peak at 22951 cm^{-1}, band E, is much broader than the others in the low resolution spectrum and higher resolution clearly shows that it is made up of two separate vibronic transitions (see later). The lower wavenumber band, centred at 22988 cm^{-1} will be referred to as band E(i) while that at 22996 cm^{-1} is band E(ii).

5.3.2 Isotope shifts

Not withstanding the rotational structure, which is discussed later, the high resolution LIF spectra also reveal the positions of different isotopomer features. The four most common naturally occurring isotopes of zinc are ^{64}Zn(48.9%), ^{66}Zn(27.8%), ^{67}Zn(4.1%), and ^{68}Zn(18.6%). Figure 5.3 shows part of the high resolution spectrum of band A. separate peaks due to ^{64}Zn, ^{66}Zn, and ^{68}Zn can clearly be observed in an intensity ratio corresponding closely to the relative natural abundance. From the natural abundance, observation of weak peaks due to ^{67}Zn might also be expected but are not observed. A possible explanation for this could due to nuclear spin splitting. ^{64}Zn, ^{66}Zn, and ^{68}Zn each have a nuclear spin of 0 so no nuclear spin splitting is observed. On the other hand ^{67}Zn has a nuclear spin of 5/2 and so each transition can be split into five lines though the coupling of the nuclear spin to the spin of the unpaired electron. This will serve to dilute the intensity of each individual component making them too small to observe.

The observed isotope shift is helpful in a sense, but it is also a hindrance. On the negative side, each spectrum contains three times as many as a single isotopomer. The congestion and confusion this causes is quite severe in places, as will be seen later. On the other hand, the isotopic shift can of itself give useful information about the vibrational modes involved in a given transition. For example, a transition involving excitation of the Zn-C stretching mode should give a much larger zinc isotopic shift than, say, the methyl torsion. Quantitative arguments such as these could potentially help in the vibrational assignments. However, because it is not expected to be easy to describe the normal modes of ZnC_2H_5 in terms of, for example, simple bond stretches and angle distortions, a more quantitative approach was used in this work.

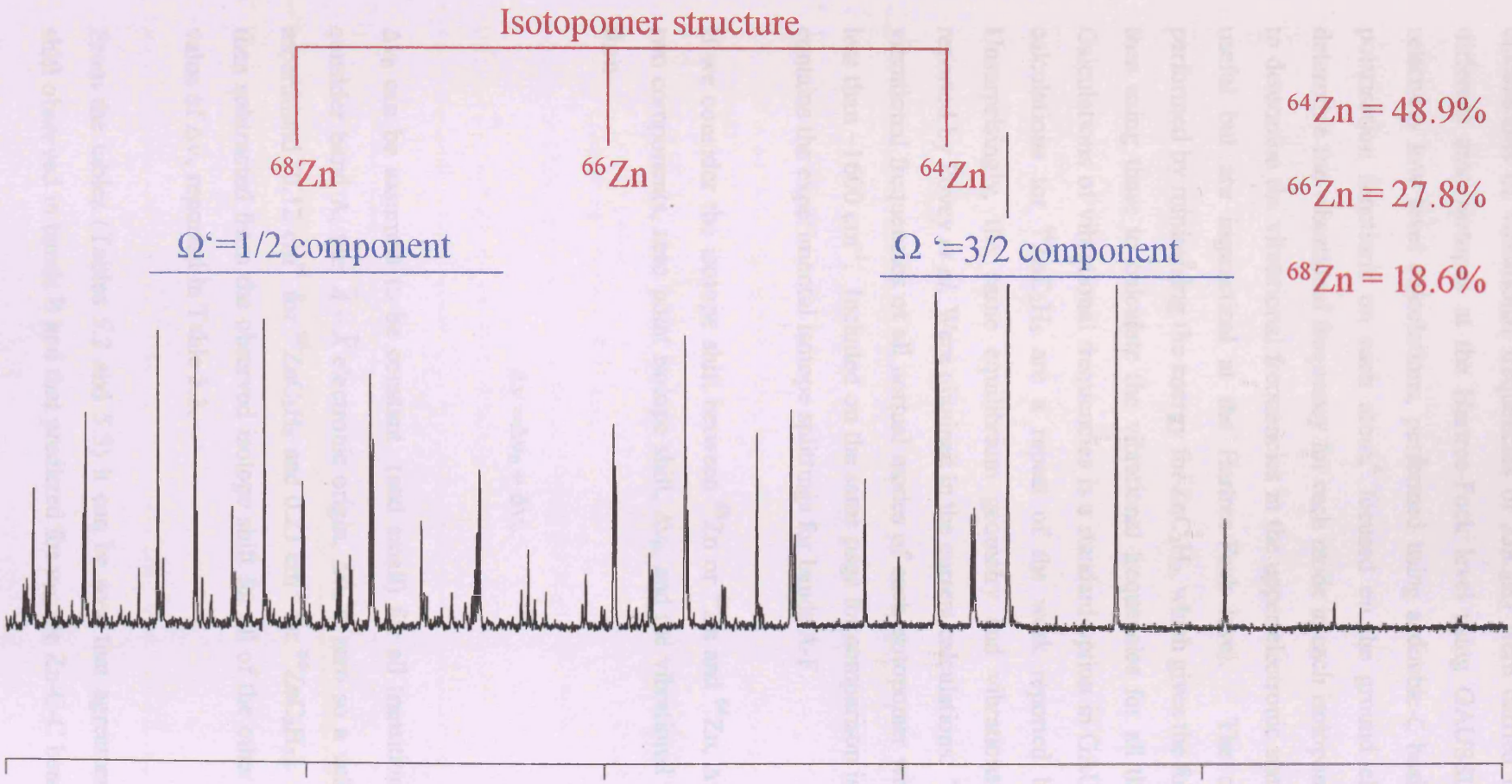

Figure 5.3: The rotationally resolved spectrum of band E(ii) showing the two spin-orbit like components of the $K'=1\text{-}K''=1$ sub-band

The more quantitative approach was based on *ab initio* calculations. *Ab initio* calculations of vibrational frequencies of ZnC_2H_5 were carried out for the three different zinc isotopes at the Hartree-Fock level using GAUSSIAN 94.[3] These relatively low level calculations, performed using a double-ζ basis set with added polarisation functions on each atom,[4] focused on the ground electronic state to determine the vibrational frequency for each mode in each isotopomer. Calculations to determine the vibrational frequencies in the upper electronic state would be more useful but are impractical at the Hartree-Fock level. The calculations were performed by minimising the energy for ZnC_2H_5, which gives the force constants and then using these to calculate the vibrational frequencies for all three isotopomers. Calculations of vibrational frequencies is a standard option in GAUSSIAN 94. The calculations for $^{64}ZnC_2H_5$ are a repeat of the work reported by Povey *et al.*[2] Unsurprisingly, the same equilibrium geometry and vibrational frequencies as reported by Povey *et al.* Were obtained in the current calculations. Table 5.2 lists the vibrational frequencies of all normal modes of each isotopomer with a frequency of less than ~1600 cm^{-1}. Included on the same page for comparison is Table 5.3 which contains the experimental isotope splittings for bands A-F.

If we consider the isotope shift between ^{68}Zn or ^{66}Zn and ^{64}Zn, $\Delta\nu$, to be made up two components, zero point isotope shift, $\Delta\nu_0$, and the vibrational isotope shift, $\Delta\nu_v$ then

$$\Delta\nu = \Delta\nu_0 + \Delta\nu_v. \qquad (1)$$

$\Delta\nu_0$ can be assumed to be constant (and small) for all transitions. If initially we consider band A, the $\tilde{A} - \tilde{X}$ electronic origin, $\Delta\nu_v$ is zero so a value of $\Delta\nu_0$ can be ascertained (0.12 cm^{-1} for $^{66}ZnC_2H_5$ and 0.23 cm^{-1} for $^{66}ZnC_2H_5$). These values are then subtracted from the observed isotope shift for all of the other bands giving the value of $\Delta\nu_v$ reported in Table 5.3.

From the tables (Tables 5.2 and 5.3) it can be seen that agreement in the isotopic shift observed in bands B and that predicted for ν_{11}, the Zn-C-C bend, is good. More

Table 5.2 Calculated[a] frequencies of ZnC_2H_5

Mode	Description[c]	Symmetry	*ab initio* vibrational frequencies[a] ($\Delta\nu$)[b] all in cm^{-1}		
			$^{64}ZnC_2H_5$	$^{66}ZnC_2H_5$	$^{64}ZnC_2H_5$
ν_4	CH_3 def.	a′	1596.5	1596.5	1596.5
ν_5	CH_2 def.	a′	1561.1	1561.1	1561.1
ν_6	CH_3 def.	a′	1516.6	1516.6	1516.6
ν_7	CH_2/CH_3 wag (ip)	a′	1208.2	1208.2	1208.2
ν_8	C-C stretch	a′	1057.9	1057.9	1057.9
ν_9	CH_2/CH_3 wag (ap)	a′	994.1	994.1	994.1
ν_{10}	Zn-C stretch	a′	381.3	380.3(-1.0)	379.4(-1.9)
ν_{11}	Zn-C-C bend	a′	196.5	195.9(-0.6)	195.4(-1.1)
ν_{14}	CH_3 def.	a″	1606.0	1606.0	1606.0
ν_{15}	CH_2/CH_3 twist (ap)	a″	1344.0	1344.0	1344.0
ν_{16}	CH_2/CH_3 twist (ip)	a″	961.5	961.5	961.5
ν_{17}	CH_2 rock	a″	602.9	602.9	602.8(-0.1)
ν_{18}	CH_3 torsion	a″	236.2	236.2	236.2

a) The *ab initio* calculations employed were at the Hartree-Fock UHF level using a DZP basis set. For more details see ref. 5.

b) $\Delta\nu$ is the difference in vibrational frequency between the specified isotopomer and ^{64}Zn. If not stated $\Delta\nu$ is zero.

c) The mode descriptions are approximate and are based on calculated atomic displacement vectors. According to the *ab initio* calculations the wagging, rocking and twisting motions of the CH_2 and CH_3 groups are heavily mixed. The abbreviations ip and ap refer to in-phase and anti-phase motions of the CH_2 and CH_3 groups.

Table 5.3 Observed isotope splittings in bands A-F

Band	$^{66}ZnC_2H_5$ in cm^{-1}			$^{68}ZnC_2H_5$ in cm^{-1}		
	$\Delta\nu$	$\Delta\nu_e$	$\Delta\nu_v$	$\Delta\nu$	$\Delta\nu_e$	$\Delta\nu_v$
A	-0.12	-0.12	-0	-0.23	-0.23	-0
B	-0.88	-0.12	-0.76	-1.74	-0.23	-1.71
C	-0.91	-0.12	-0.79	-1.76	-0.23	-1.53
D	-0.23	-0.12	-0.11	-0.45	-0.23	-0.22
E(i)	-0.89	-0.12	-0.77	-1.72	-0.23	-1.49
E(ii)	-1.08	-0.12	-0.96	-2.12	-0.23	-1.89
F	-0.80	-0.12	-0.68	-1.53	-0.23	-1.30

precisely the isotope shift will depend upon the magnitude of ν and, since the *ab initio* calculations are based upon ground state vibrational frequencies so a more accurate determination of ν_v should include the scaling factor of υ'/ν''. If this scaling factor is considered for ν_{11} the calculated value of the isotope shift is 0.75 cm^{-1} for ^{66}Zn which is in excellent agreement which the observed spitting ($\Delta\nu_v$) in band B (0.76 cm^{-1}). The dispersed fluorescence work reported in Chapter 3 assigned band B to one quanta in ν_{10} so the isotope splitting data reported strongly supports this assignment.

The dispersed fluorescence work assigned band C to one quanta in the Zn-C stretch (ν_{10}) and from Table 5.2 an isotope splitting (for $^{66}ZnC_2H_5$) of 1.0 cm^{-1} is expected. The agreement with the observed isotope splitting ($\Delta\nu_V$ = 0.79 cm^{-1}) is good but not excellent. The difference is magnified further by considering the υ'/ν'' factor which gives a new predicted value of $\Delta\nu_v$ of 1.11 cm^{-1}. This slight difference in predicted and observed isotope splitting does not disagree with the vibrational assignment made in Chapter 3, particularly as of the other feasible alternate assignments are expected to have an isotope splitting significantly smaller than that observed. It is possible to explain the smaller than expected splitting in two ways. (i) As the *ab initio* calculation are of ground state vibrational frequencies rather than those observed in the excited state the exact degree of mode mixing may not be accurately predicted. Or (ii) the ν_{11} level lies close in energy to another level of the same symmetry and though a fermi resonance the character of these states are mixed. If the ν_{10} level is mixed with a level for which a much smaller isotope splitting is expected, then the mixing process would account for the smaller isotope splitting observed.

A small isotope splitting (0.11 cm^{-1}) is observed for band D, implying that transition is to a vibrational mode in which the zinc remains more or less stationary. The position of the peak at 22951 cm^{-1} in the excitation spectrum is 436 cm^{-1} from the $\tilde{A}-\tilde{X}\,0_0^0$ electronic origin so using the *ab initio* frequencies the most obvious assignment is to $2\nu_{18}$, where ν_{18} is methyl torsion. Although $\Delta\nu_v$ is small (0.11 cm^{-1}) it is still larger than that predicted for $\Delta\nu_{18}$ which suggests mixing with a level(s)

close in energy. The ν_{10} and the $2\nu_{18}$ levels are close in energy, and since ν_{10} has a smaller than expected isotope splitting while that in ν_{18} is larger than expected, considerable mixing between these modes seems a likely explanation.

Band D is a peak of medium to strong intensity and this ties in nicely with the Femi resonance argument. If the $2\nu_{18}$ level has considerable ν_{10} character it is feasible that the 18_0^2 transition at 22951 cm^{-1} 'borrows' intensity from the 10_0^1 peak at 22939 cm^{-1}. The methyl torsion is non totally symmetric so two quanta is expected to be the first member of this vibrational progression in this mode from Frank-Condon arguments. However, Frank-Condon arguments would also lead one to expect the 18_0^2 peak to be very weak in the absence of Fermi resonance.

Interestingly, a weak peak is observed in the excitation spectrum at 22740 cm^{-1}, which is approximately halfway between band D and the origin. High resolution spectra of this weak band have not been recorded so it is not possible to comment on the isotope splitting. However, it is possible that this band corresponds to the 18_0^1 transition, with the intesity being gained from a vibronic coupling mechanism.

The dispersed fluorescence work of band D was not in itself useful in assigning this peak. The spectrum was comparable to that observed for band C and consisted mainly of features assigned to ν_{10}. It was therefore assumed in Chapter 3 that collisional depopulation to the near by level occurs before the emission of a fluorescence photon. An alternative explaination could be that the peak is dominated by $2\nu_{18}$ but contains contributions from ν_{10}, the dispersed fluorescence spectrum pumping this band will appears as if from ν_{10} since this is the source of the oscillator strength.

The information on vibrational structure ascertained from isotope splitting in bands E(i), E(ii), and F is less conclusive. Nevertheless the splitting observed in band E(ii)was the largest observed of any band (0.96 cm^{-1} for $^{66}ZnC_2H_5$), and larger than the predicted isotope splitting for single quantum excitation of any vibrational mode. This suggests assignment of band E(ii) to two quanta in either the Zn-C stretch or

Zn-C-C bend, as these are the only two modes for which a significant isotope splitting is predicted. In the low resolution work described in Chapter 3, band E was assigned to $\tilde{A}-\tilde{X}11_0^2$ but no distinction was made between band E(i) and band E(ii) so this assignment could apply to either. However, the isotope splitting data implies the assignment $\tilde{A}-\tilde{X}11_0^2$ to band E(ii) is correct and observed dispersed fluorescence spectrum arises from pumping band E(ii).

The difficulty with this assignment is, although the isotope splitting is too large to be explained using one quanta in any vibrational mode, it is still smaller than the predicted isotope shift for 11_0^2 of ~1.2 cm^{-1}. In addition the observed isotope splittings in band E(i) and band F are larger than can easily be explained. The *ab initio* work indicates that significant isotope splittings will only be observed for ν_{10} and ν_{11} yet it is not easy to explain bands E(i) or F in terms of either of these vibrational modes. However, as has been suggested in previous paragraphs, a mixing of vibrational levels, particularly those close in energy, could result in deviations from the expected isotope splittings. Clearly, while helpful, the isotope splittings are insufficient for establishing the assignment of some of the ZnC_2H_5 bands.

5.4 Rotational Structure

The rotational structure of bands A-F contain several common features. However, there are also substantial differences between each band so it is necessary to treat each individually. The band whose structure is most fully understood is band E(ii) and so this provides a convenient stating point.

5.4.1 Band E(ii)

Band E(ii) has been tentatively assigned as the $\tilde{A}-\tilde{X}11_0^2$ transition, where ν_{11} is the Zn-C-C bend. Figure 5.4 shows the region covered by band E(ii), The isotope splitting from the three isotopes of zinc makes the diagram more complicated than it would otherwise be and the magnitude of the splitting is labelled on the diagram.

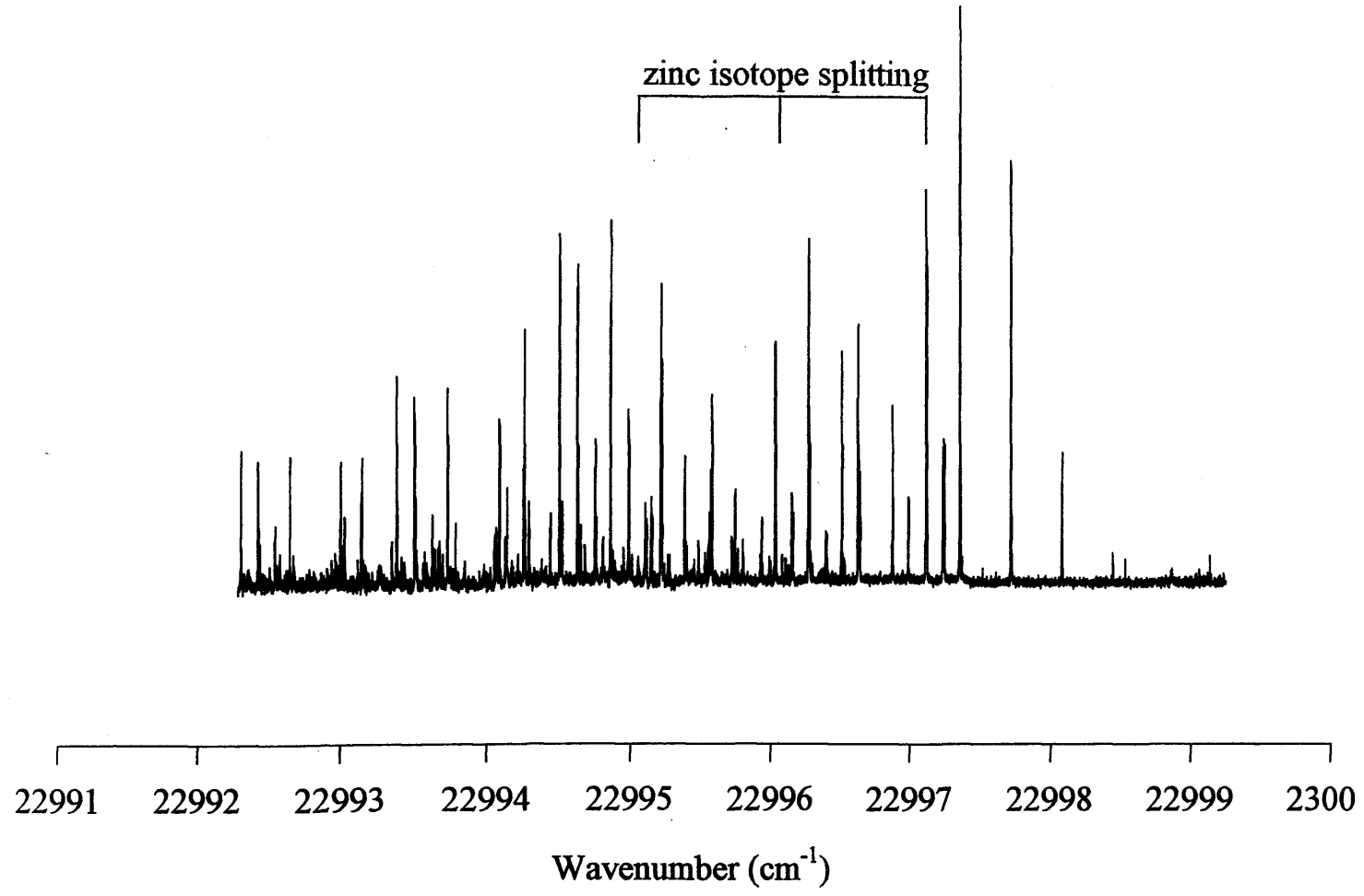

Figure 5.4: Spectrum showing the range covered by band E(ii)

SPECIAL NOTE

ITEM SCANNED AS SUPPLIED
PAGINATION IS AS SEEN

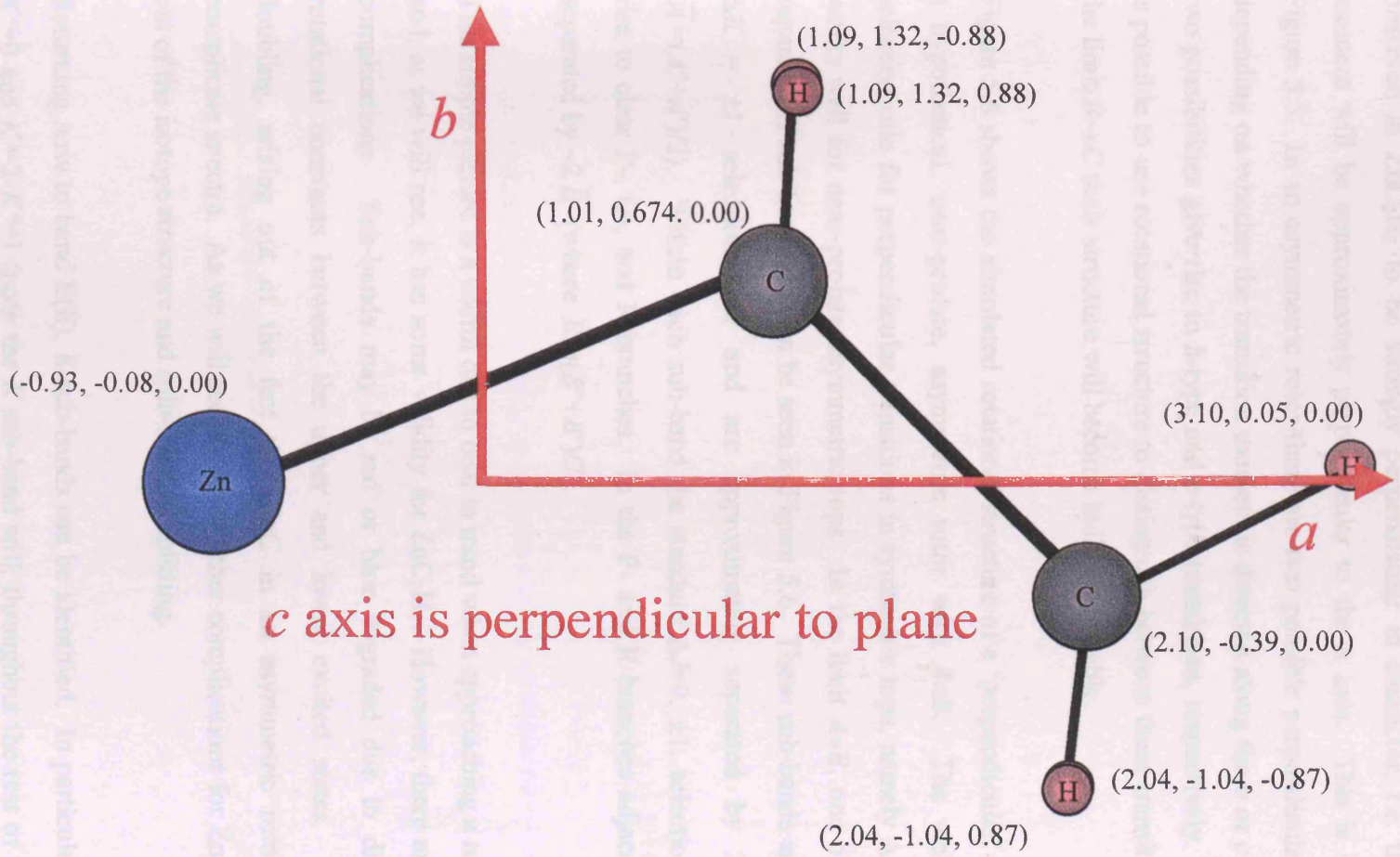

Figure 5.5 Geometry of ZnC_2H_5 from *ab initio* calculations. The cartesian coordinates (in A) of each atom are shown. The origin of these coordinates is the centre of mass of the molecule.

The *ab initio* calculations indicate that ZnC_2H_5 will be close to a prolate symmetric top with $A>>B\approx C$ (the calculated rotational constants were (A=1.0237, B=0.1179 and C=0.1100 cm^{-1}). By analogy with $ZnCH_3$, we expect the $\tilde{A}-\tilde{X}$ transition being observed in ZnC_2H_5 to be strongly perpendicular in character, *i.e.* the transition moment will be approximately perpendicular to the *a* axis. This is indicated by Figure 5.5. In an asymmetric rotor there are two possible perpendicular transitions depending on whether the transition moment is directed along the *b* or *c* axis. These two possibilities give rise to *b*-type and *c*-type transitions, respectively. Although it is possible to use rotational structure to distinguish between these transition types, in the limit $B\rightarrow C$ their structure will become indistinguishable.

Figure 5.6 shows the simulated rotational structure of a 'perpendicular' transition of a hypothetical, near-prolate, asymmetric rotor with $A»B$. The well known K selection rule for perpendicular transitions in symmetric tops, namely $\Delta K = \pm 1$, also works well for near-prolate asymmetric tops. In the limit $A»B$, one observes well separated K sub-bands, as can be seen in Figure 5.6. These sub-bands arise from the $\Delta K = \pm 1$ selection rule and are approximately separated by $2\overline{A}$ (where $\overline{A}=(A''+A')/2$). Within each sub-band the standard $\Delta J=0, \pm 1$, selection rule gives rise to clear P-, Q-, and R-branches. In the P- and R-branches adjacent lines are separated by $\sim 2\overline{B}$ (where $\overline{B}=(B''+B')/2$).

This simple picture is a useful one to bear in mind when approaching a new spectrum and, as we will see, it has some validity for ZnC_2H_5. However, there are also many complications. Sub-bands may be red or blue degraded due to differences in rotational constants between the upper and lower excited states. Asymmetry doubling, arising out of the fact that $B\neq C$ in an asymmetric rotor, will also complicate spectra. As we will see, there are other complications for ZnC_2H_5 arising out of the isotope structure and spin-rotation splitting.

Returning now to band E(ii), K sub-bands can be identified. In particular, the $K'=1$-$K''=0$ and $K'=2$-$K''=1$ (note the K sub-band will, throughout the rest of this chapter, be described using the following notation (K'-K'') *e.g.* (0-1) or (2-1) are relatively easy to pick out. Figure 5.4 is dominated by the (1-0) sub-band. One would expect

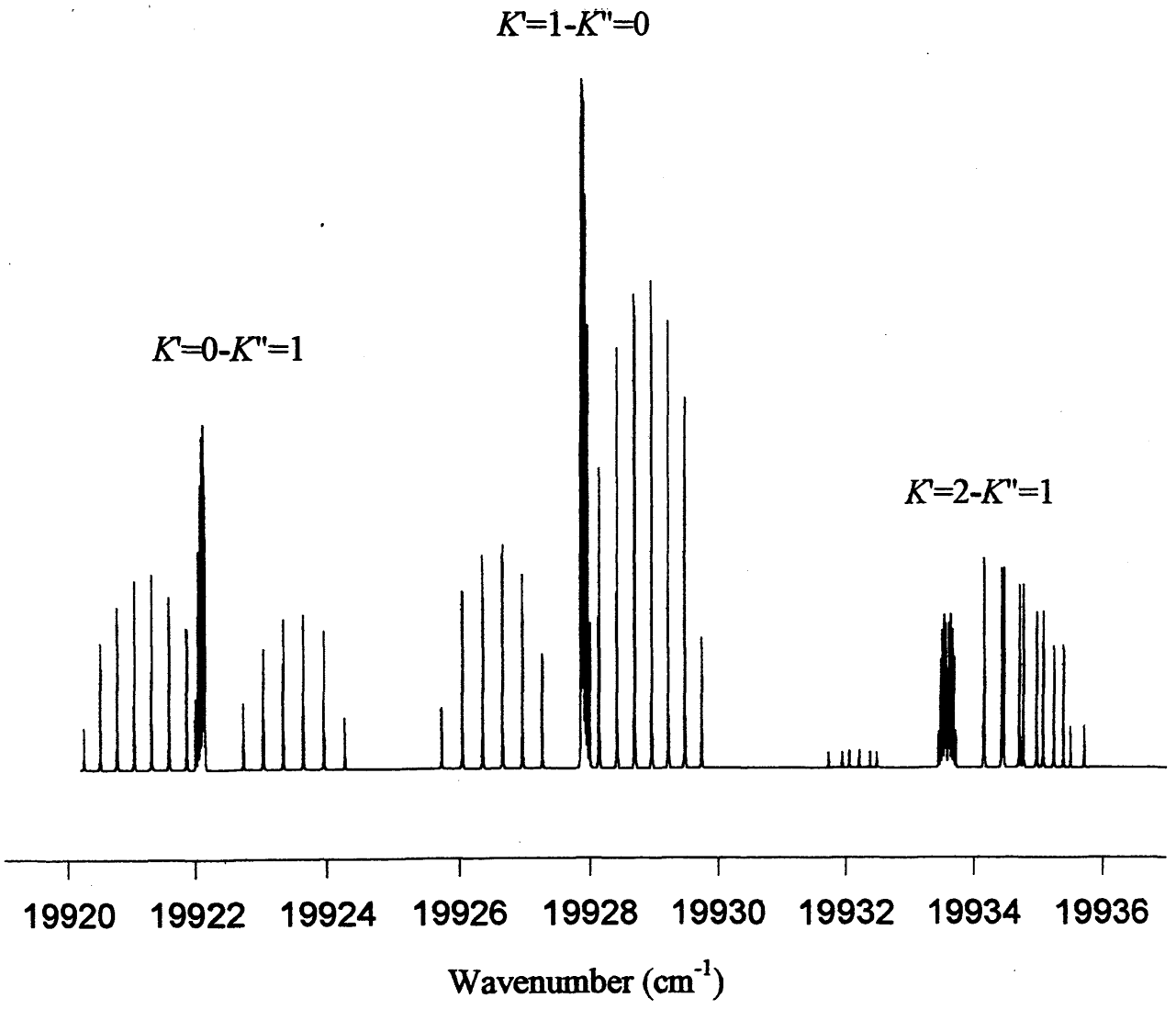

Figure 5.6: Simulate spectrum of a hypothetical near-prolate asymmetric top with $A'=A''=3$, $B'=B''=0.15$, and $C'=C''=0.14$ cm^{-1}

the (1-0) sub-band to be more intense than the (2-1) sub-band due to the greater population of K''=0 verses K''=1. This is a useful aid in identification. Another useful aid in identifying (2-1) sub-bands is the clear asymmetry doubling in these sub-bands because the asymmetry doubling is largest in K=1 stacks.

Although some of the coarse features mentioned can be recognised in the ZnC_2H_5 spectra, a simple asymmetric rotor model for ZnC_2H_5 is inadequate. A characteristic of the ZnC_2H_5 bands is the splitting of K'-K'' into doublets. As will be shown, this splitting is K'' dependent. Specifically it varies linearly with K' and can therefore be identified as a strong spin-rotation doubling in the excited state.[5-7] In particular, this splitting has the approximate value $\varepsilon_{aa}'K'$, where ε_{aa} is the diagonal a component of the spin-rotation tensor. Consequently, even without a sophisticated analysis, we can estimate that $\varepsilon_{aa}' \approx 2.7$ cm^{-1} in the upper state for band E(ii). The significance of this value will be discussed later in this chapter.

The spin-rotation doubling in the (1-0) sub-band is marked in Figure 5.7. This spin-rotation splitting is quite similar in effect to spin-orbit splitting, except for the fact that it is K' dependent (and hence there is no splitting in the (0-1) sub-band). In other words, each sub-band, except the (0-1) splits into two components which resemble spin-orbit doublets. This analogy with spin-orbit coupling is important because, like genuine spin-orbit coupling, a strong spin-rotation interaction can induce Hund's case (a) behaviour in an electronic state. In $ZnCH_3$, the $\tilde{A}^2E$-$\tilde{X}^2A_1$ transition is from a Hund's case (b) ground state to a Hund's case (a) excited state. This give rise to different rotational structure from that seen in case (a)-case (a) or case (b)-case (b) transitions (the latter corresponds to a 'normal' asymmetric rotor of the type described earlier). In a case (a)-case(b) transitions the rotational structure exhibits '+3B, +B, -B, -3B' structure, *i.e.* at low resolution four branches are seen with the aforementioned intervals between adjacent lines, rather than 2B. If ZnC_2H_5 also undergoes case (a)-case (b) transitions then it to should also show four branches. This behaviour is indeed observed.

Figure 5.7 shows part of the Ω'=3/2 component of the (1-0) sub-band. The overall pattern is similar to the classic '+3B, +B, -B, -3B' structure expected for spin-orbit

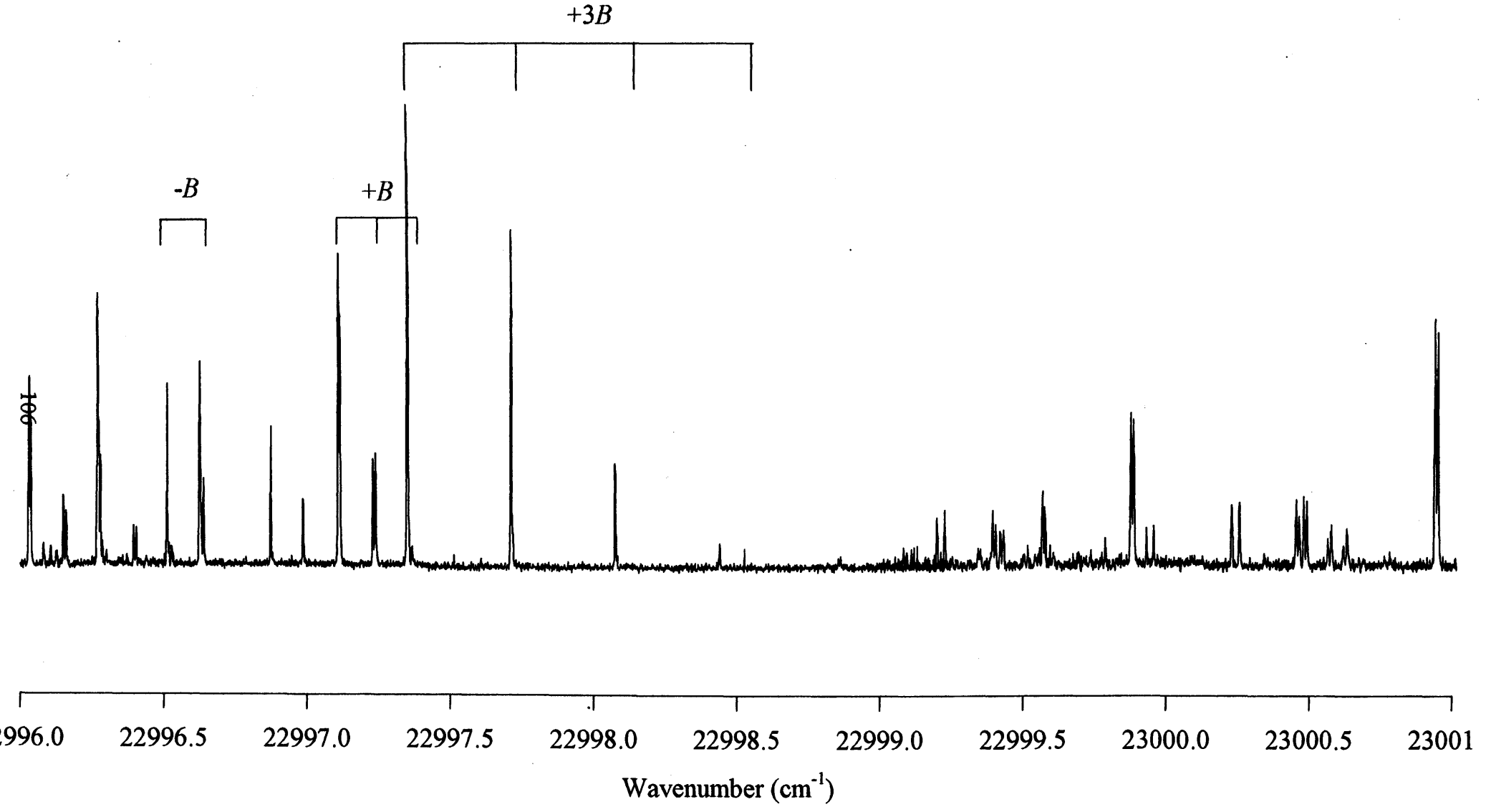

Figure 5.7: Part of band E(ii), the left hand side of the spectrum shows the -3*B*,-*B*,+*B*,+3*B* structure while the right hand side shows the (1-2) *K* sub-band and asymmetry splitting can clearly be seen

split ^{2}E-^{2}A transition in a symmetric top. The '+3*B*, +*B*, -*B*, -3*B*' pattern is again manifestation of the orbital angular momentum generated by coupling of the electron spin with rotation about the *a* axis, *i.e.* a spin-rotation interaction. It can been seen that the first member of the +*B* series is missing, as expected for a Ω'=3/2 system, and each of the others and the -*B* transitions, are composed of two lines while each of +3*B*/-3*B* is an individual line. The energy level diagram (figure 5.8) shows that the first member of the +*B* series is expected to be missing as these transitions are from $J''=K''-½$ which obviously do not exist for $K''=0$. From the energy level diagram it can also be seen that the small splitting of the +*B*/-*B* lines is due to a spin-rotation interaction in the ground state. This splitting is not observed in the +3*B*/-3*B* branches because parity restrictions allow only one of the spin-rotation doublets transitions to occur (+↔- transitions are allowed but +↔+ and -↔- transitions are parity forbidden).

The branches in the energy level diagram are labelled $^xY_{ii}$ where x refers to the designation of the ΔN value, Y refers to the ΔJ value and I refers to the relationship between *N* and *J* in each state. i=1 or 2 for $J=N+½$ or $J=N-½$, respectively, in a given electronic state.

In the (2-1) sub-band (see Figure 5.7) a splitting is observed which is in addition to the ground state spin rotation splitting described above. This splitting arises from asymmetry doubling. This splitting is caused by the differences between the *B* and *C* constants but is not a function of solely the ground or excited state values but a combination of both. Each of the +*B*/-*B* appears as four, approximately equally intense, lines. The +3*B*/-3*B* lines are simpler since ground state spin-rotation cannot be observed but they are still divided into two by the asymmetry. This discussion of the asymmetry splitting is slightly over simplified as the values of ε_{bb} and ε_{cc}, and possibly ε_{ab} and ε_{ba}, in both states will also effect splitting. Consequently, the asymmetry splitting can not accurately be used with a combination difference analysis to determine *B* or *C* in either state. A more sophisticated analysis involving simulations is essential.

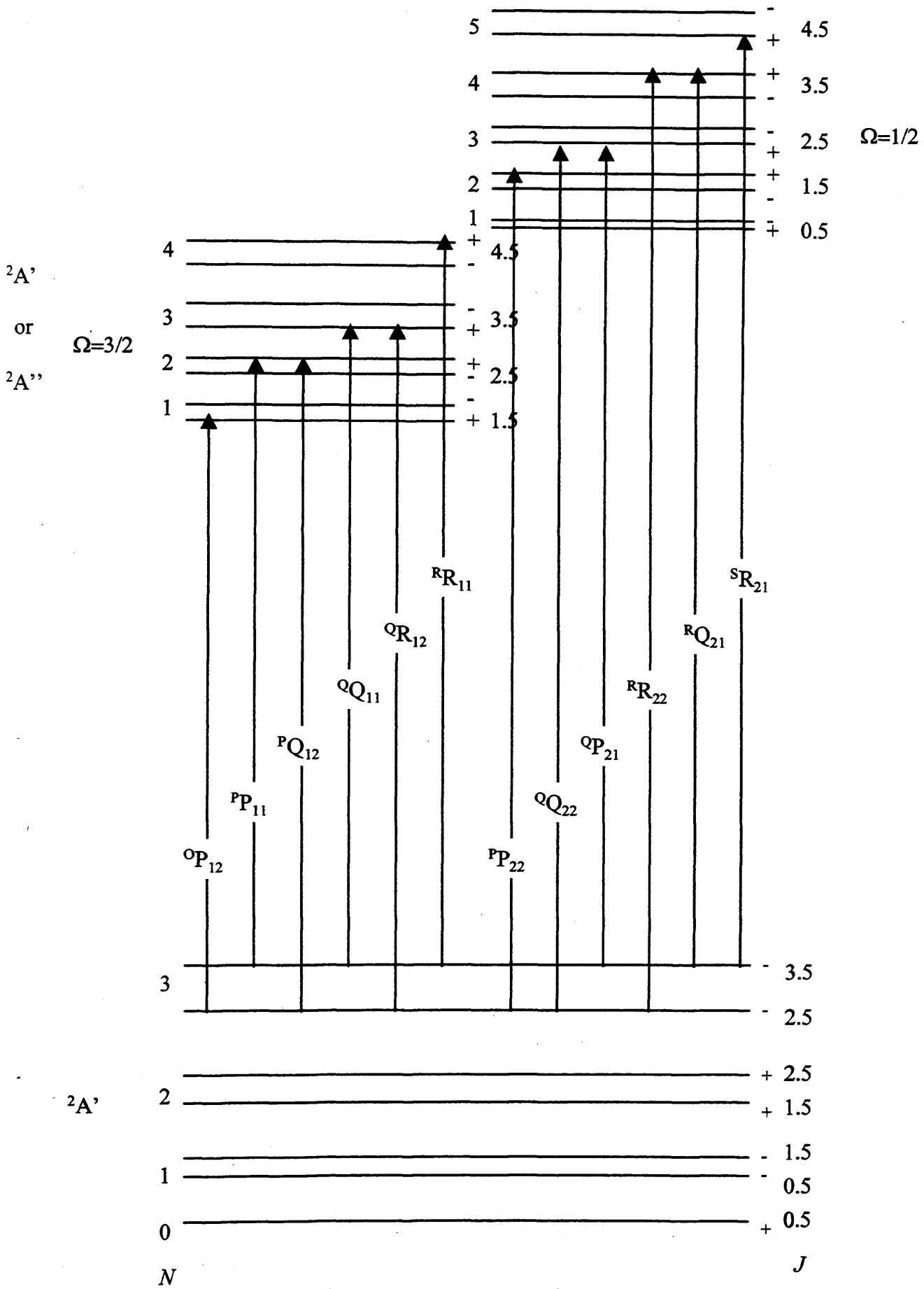

Figure 5.8: Energy level diagram for an asymmetric rotor with spin-rotation. Allowed transitions are marked on the figure. The twelve branches collapse into four at lower resolution.

5.4.1.2 Simulated spectra

Figure 5.9(b) shows the simulated spectrum obtained assuming a *b*-type transition for band E(ii): This simulation was obtained using the ASYMSR model described in Chapter 4. Figure 5.9(c) shows that assuming a *c*-type transition. In both simulations a single isotopomer has been included. Figure 5.9 shows that there is good agreement between the experimental and simulated spectra assuming either a *b*- or a *c*- type transition. Both spectra have been obtained by from a least square fit to the experimental spectrum (Figure 5.9(a)) and the molecular constants are given by Table 5.4 along with standard deviations. It can be seen that the overall standard deviations for both the *b*- and *c*-type transitions are comparable.

Although the *A* rotational constants in both the upper and lower electronic states have a relatively small standard deviation from the fit, this is actually misleading. *A'* and *A"* are strongly correlated and in fact the meaningful quantity is ΔA, *i.e.* the difference in *A* constants that is well determined but the absolute values are not. This arises as the (0-1) sub-band cannot be assigned.

A pure *c*-type transition would correspond to a transition from the $^2A'$ ground state to the $^2A''$ excited state (in which there is a node in the unpaired electron density in the plane of the molecule). Conversely, a *b*-type, $^2A'$-$^2A''$ transition is potentially part of an *a/b* hybrid transition because the axes defined by the Zn *p* orbitals and the principal axes do not coincide. Thus it might be thought that the appearance of some *a*-type (parallel) character would help distinguish between the $^2A''$-$^2A'$ and the $^2A'$-$^2A'$ transitions. However parallel character can not easily be found in the experimental spectrum. This can be explained either by assuming that the *a*-inerial axis is nearly parallel to the *z* axis, the Zn-C bond, or it is evidence that the transition is *c*-type and the symmetry of the upper state is $^2A''$.

The fact that band E(ii) can be quite accurately simulated assuming a *b*- or *c*-type transition is prehaps unsurprising as ZnC_2H_5 is close to a prolate symmetric top. In the symmetric rotor limit both *b*- and *c*-type transition would be equivalent transitions perpendicular to the top axis. From the simulated spectra (Figure 5.9(b)

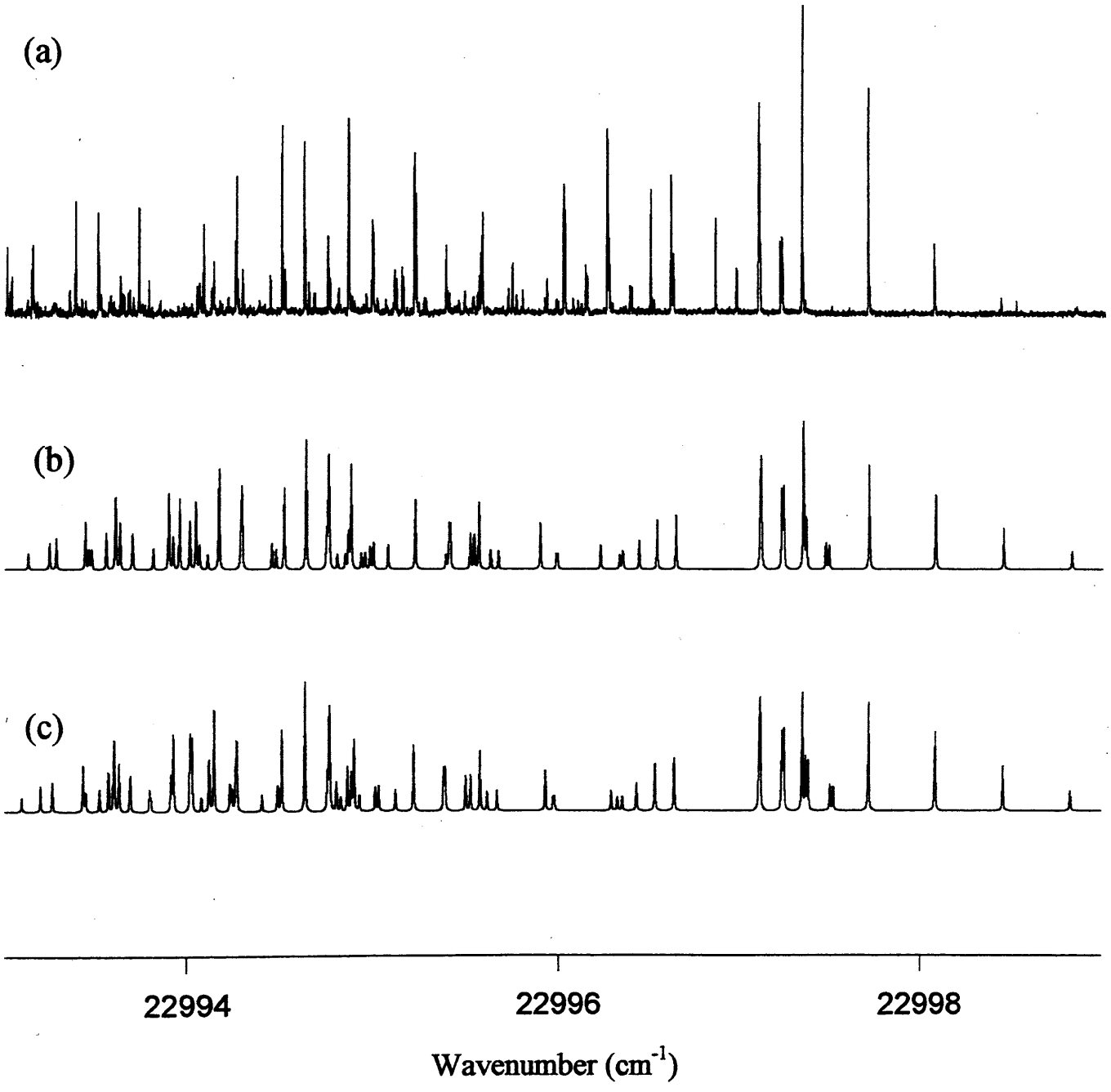

Figure 5.9 Experimental (a) and simulated spectra generated assuming a *b*-type (b) and a *c*-type transition moment .

Table 5.4 comparison of rotational constants generated assuming a *b*- and a *c*-type transition for band E(ii)

Constant	*b*-type $^{64}Zn/cm^{-1}$	SD/cm^{-1}	*c*-type $^{64}Zn/cm^{-1}$	SD/cm^{-1}
T_e	22994.7394	0.0067	22994.7423	0.0078
A''	1.0184	0.0007	1.0179	0.0008
B''	0.1214	0.0006	0.1237	0.0004
C''	0.1145	0.0006	0.1146	0.0004
ε_{aa}''	0.0000[a)]	-	0.0000[a)]	-
ε_{bb}''	0.004[a)]	-	0.004[a)]	-
ε_{cc}''	0.004[a)]	-	0.004[a)]	-
A'	1.0856	0.0009	1.0843	0.0009
B'	0.1253	0.0025	0.1209	0.0023
C'	0.1114	0.0023	0.1201	0.0022
ε_{aa}'	2.7090	0.0031	2.7245	0.0029
ε_{bb}'	0.1473	0.0131	0.1561	0.0097
ε_{cc}'	0.1250	0.0139	0.1667	0.0109
Overall SD		0.0030		0.0039

[a] these values were fixed in the fit.

and (c)) it can be that the main area of difference between the two types of transitions is found in the (0-1) sub-band. Unfortunately this spectral region has proved the most difficult in which to assign lines for three reasons:

(i) The low temperature in a supersonic jet limits the population of K''-1.

(ii) The ^{64}Zn K'=0-K''=1 sub-band falls in the same spectral region as the stronger (1-0) sub-band of the heavier isotopes.

(iii) The magnitude of ε_{bb} and ε_{cc} in both states has a large effect on the position of lies and removes the +2*B*/-2*B* structure expected for the (0-1) transition. The lack of clear pattern in the simulated spectra makes finding corresponding peaks in the experimental spectrum very difficult. We have not been successful so far in the quest.

Figure 5.10 show the best simulated spectrum achieved. Each isotopomer of zinc has been included and Table 5.5 lists the rotational constants determined for each. In the final fit the values of the *A*, *B* and *C* rotational constants in both states and the upper state spin-rotation constants ε_{aa}, ε_{bb} and ε_{cc} were allowed to vary. The ground state spin-rotation constants ε_{bb} and ε_{cc} were manually adjusted to obtain the correct splitting in the +*B*/-*B* structure. If they were allowed to vary as part of the fit the program adjusted the lines to absolute positions rather than fitting the two +*B*/-*B* lines relative to each other. Although a value of 4×10^{-3} cm^{-1} is quoted for both ε_{bb} and ε_{cc} the splitting is dominated by a matrix term involving $(\varepsilon_{bb}+\varepsilon_{cc})/2$ so it has been impossible, in this work, to determine ε_{bb} and ε_{cc} independently.

The supersonic jet experiments performed by Miller typically have a rotational temperature of 1-3 K. The spectrum of band E(ii) was simulated at a number of temperatures and the best visual agreement between experimental and simulation was obtained at ~1.0-1.5 K. The simulated spectra shown here employed a rotational temperature of 1.5 K so that any error in this temperature serves to overemphasise the weaker parts of the spectrum, enabling real features with a low intensity to be separated from the noise. The very low temperature also means that very few rotational levels are populated so transitions from high *J* levels ($J > 9/2$) are not considered, limiting the time taken for simulations to be performed.

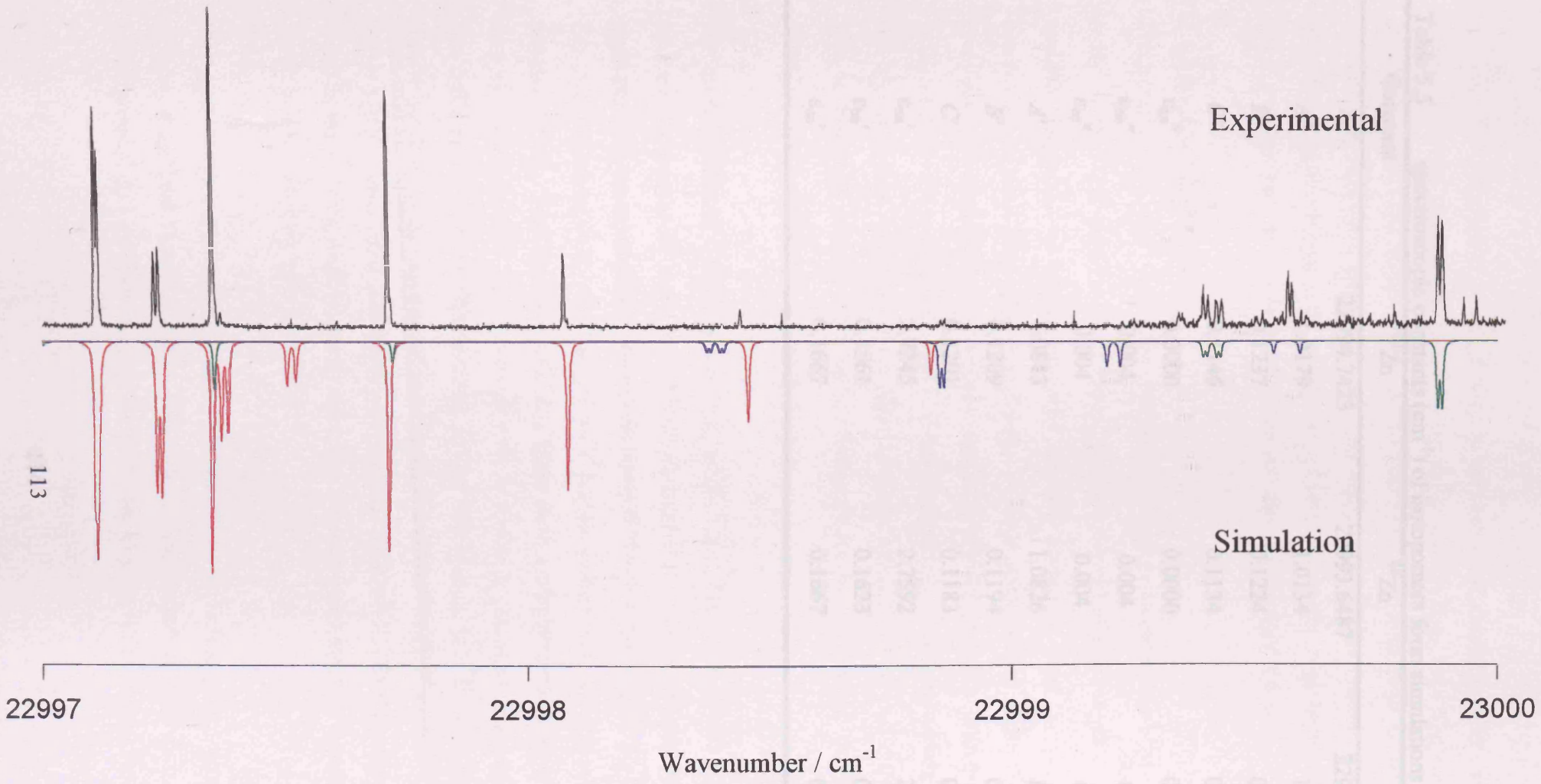

Figure 5.10: Experimental and simulated spectra of band E(ii). The experimental spectrum is made from two scans, joined at ~22999 cm^{-1}, which accounts for some of the relative intensity differences and some additional peaks in the simulated spectrum. The different colours in the simulated spectrum represen the diffent zinc isotopes (red- ^{64}Zn, green-^{66}Zn and blue ^{68}Zn)

Table 5.5 spectroscopic constants (cm^{-1}) of isotopomers form simulations of band E(ii)

Constant	^{64}Zn	^{66}Zn	^{68}Zn
T_e	22994.7423	22993.6487	22992.5928
A''	1.0179	1.0134	1.0129
B''	0.1237	0.1224	0.1219
C''	0.1146	0.1134	0.1129
ε_{aa}''	0.0000	0.0000	0.0000
ε_{bb}''	0.004	0.004	0.004
ε_{cc}''	0.004	0.004	0.004
A'	1.0843	1.0826	1.0839
B'	0.1209	0.1194	0.1179
C'	0.1201	0.1183	0.1177
ε_{aa}'	2.7245	2.7592	2.7883
ε_{bb}'	0.1561	0.1623	0.1634
ε_{cc}'	0.1667	0.1667	0.1704

In earlier fits all constants were allowed to vary but those constants which had small values and large standard deviations were set at zero in later fits. The centrifugal distortion terms were found to be in this category. The magnitude of centrifugal distortion is strongly dependent on the magnitude of the rotational angular momentum so for a system in which transitions are only observed from states with low J, as is the case here, centrifugal distortion can often be ignored.

5.4.2 Band A (22515 cm^{-1})

The peak at 22515 cm^{-1} in the low resolution excitation spectrum has been assigned to the $\tilde{A}$ - $\tilde{X}\,0_0^0$ transition as there are no peaks to the red of this intense band. The rotational structure of the origin band labelled earlier as band A, bears many similarities to band E(ii) discussed above. A large spin-rotation interaction again gives structure characteristic of a Hund's case (a)-case (b) transition with the classic '+3B, +B, -B, -3B' pattern and a spin-orbital like splitting. In the case of the band A the spin-orbit like splitting, given approximately by $\varepsilon_{aa}'K'$, gives $\varepsilon_{aa}' \approx 1.43$ cm^{-1}. This substantially smaller than the ε_{aa}' obtained for band E(ii) and trends in the magnitudes of ε_{aa} discussed in a later section.

The most significant difference between bands A and E(ii) is in the $|\Omega'|=1/2$ spin-rotation component of the $K'=1$, $K''=0$ sub-band (Ω is the orbit+spin projection quantum number in the upper electronic state).. This can be seen in Figure 5.11. The peaks labelled $^{Q}Q_{11}$ and $^{Q}R_{12}$ form a regular pattern and are separated by a distance of ~B. The lines labelled $^{R}R_{11}$ again form a regular pattern separated this time by a distance ~3B. This pattern is what is similar to that observed in band E(ii). The difficulty is that the first member of the +3B branch, the $^{R}R_{11}(0.5)$ transition, should lie close to the position of the $^{Q}Q_{11}(2.5)$ and the $^{Q}R_{12}(1.5)$ transition. While this is true for band E(ii), it is clearly not the case for band A. This anomaly is only found in the 1/2 spin-rotation component; the 3/2 component looks as expected from theory and comparison with band E(ii).

One possible explanation to this strange structure is a perturbation that moves some of the rotational levels which will cause unexpected rotational structure. Unfortunately, it is difficult use this theory to use explain the rotational structure of

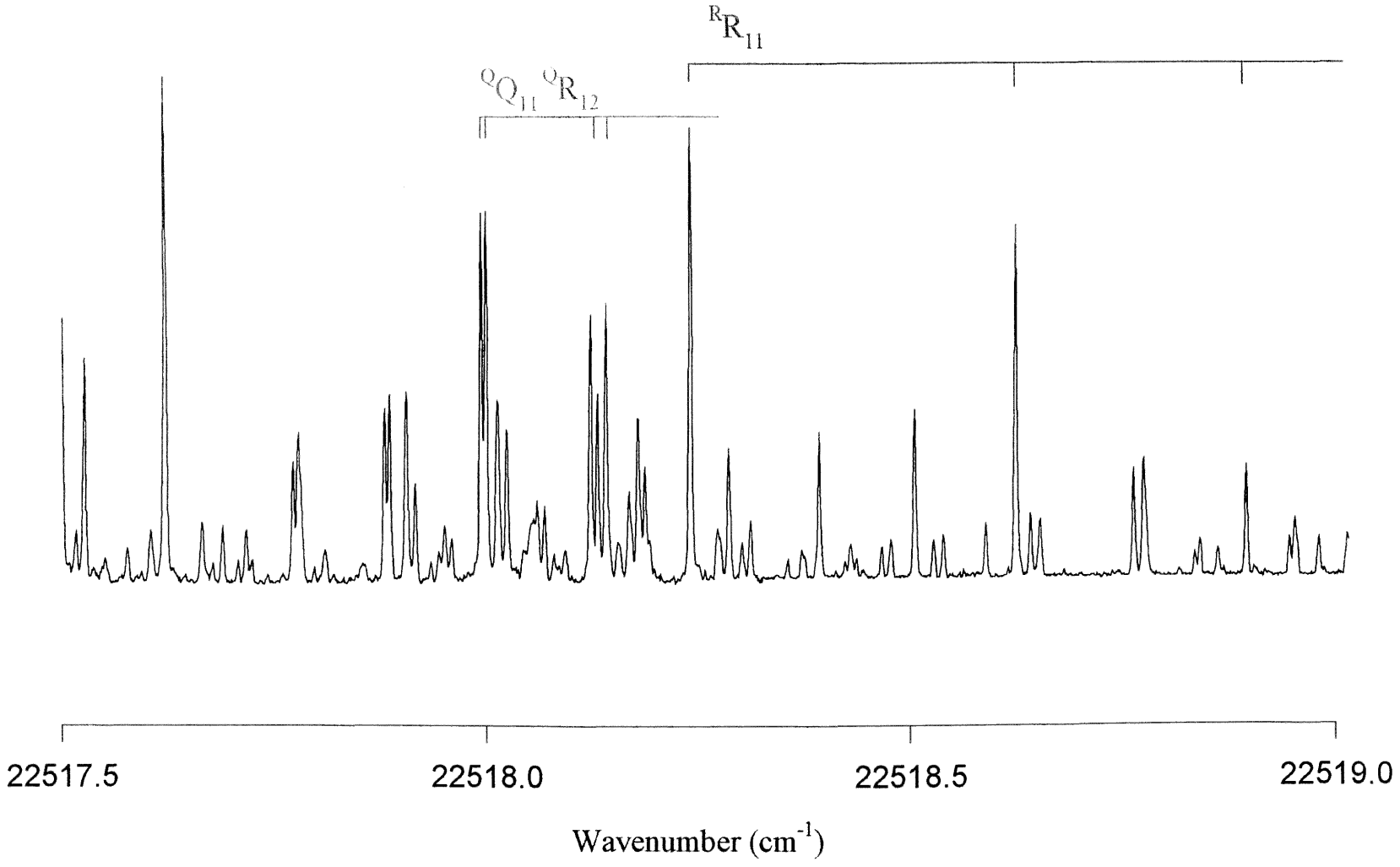

Figure 5.11 Experimental spectrum of part of band A

the origin band as the $^{Q}Q_{11}(0.5)$ and the $^{R}R_{11}(0.5)$ transitions share the same ground state (excluding spin-rotation splittings from ε_{bb}, ε_{cc}, ε_{ab} and ε_{ba}). Similarly, the excited state of the $^{Q}R_{12}(1.5)$ transition is the same as the $^{R}R_{11}(0.5)$ transition (again excluding spin rotation splittings). Another problem with the theory of a perturbation is that band B is very similar to band A and the possibility of a perturbation effecting both rotational systems is a similar way is very slim. A more probable explanation is that the unexpected structure is a manifestation of a particular combination of spin-rotation constants. The effect of the off-diagonal spin-rotation constants ε_{ab} and ε_{ba} are particularly difficult to predict.

5.4.2.1 Simulated spectra

A simulated spectrum that matches all of the assigned lines in the real spectrum has not been obtained. In particular the unusual rotational structure in the $+B$ branch, described above, has proved difficult to simulate. A reasonable fit to parts of the origin band can be obtained assuming a *b*- and a *c*-type transition (see Figure 5.12) generating the constants detailed in Table 5.6.. The parts of the spectrum included in the fit are the $+B$ and $+3B$ systems of the $|\Omega'|=3/2$ component of the (0-1) and (1-0) sub-bands; the $+3B$ systems of the $|\Omega'|=1/2$ components of the (0-1) and the (1-0) sub-bands and the $-B$ system of the (1-0) sub-band. The $+B/-B$ structure of the $|\Omega'|=1/2$ component of the (1-0) sub-band has not been included as a fit which included it was not possible. The $-B$ and $-3B$ lines are less well represented in the fits as the intensities of these lines are considerably less than the corresponding $+B$ lines often to the extent that assignment of the $-B$ and $-3B$ structure is not possible. The $-B$ lines are often difficult to assign as they under lie strong $+B$ and $+3B$ lines from other isotopes.

The $+B$ structure of the $|\Omega'|=1/2$ component of the (2-1) sub-band has not been assigned as it under lies the stronger $|\Omega'|=3/2$ component of the (1-0) sub-band. Individual lines can not easily assigned but the general position of the $+B$ transitions appear to be in the spectral region predicted by the simulations. This is in marked contrast to the $+B$ structure of the $|\Omega'|=1/2$ component of the (1-0) sub-band implying that the anomaly is purely a feature of the 1/2 component of the (1-0) sub-band and not any other sub-bands. To test this conjecture further *K* sub-bands wound need to

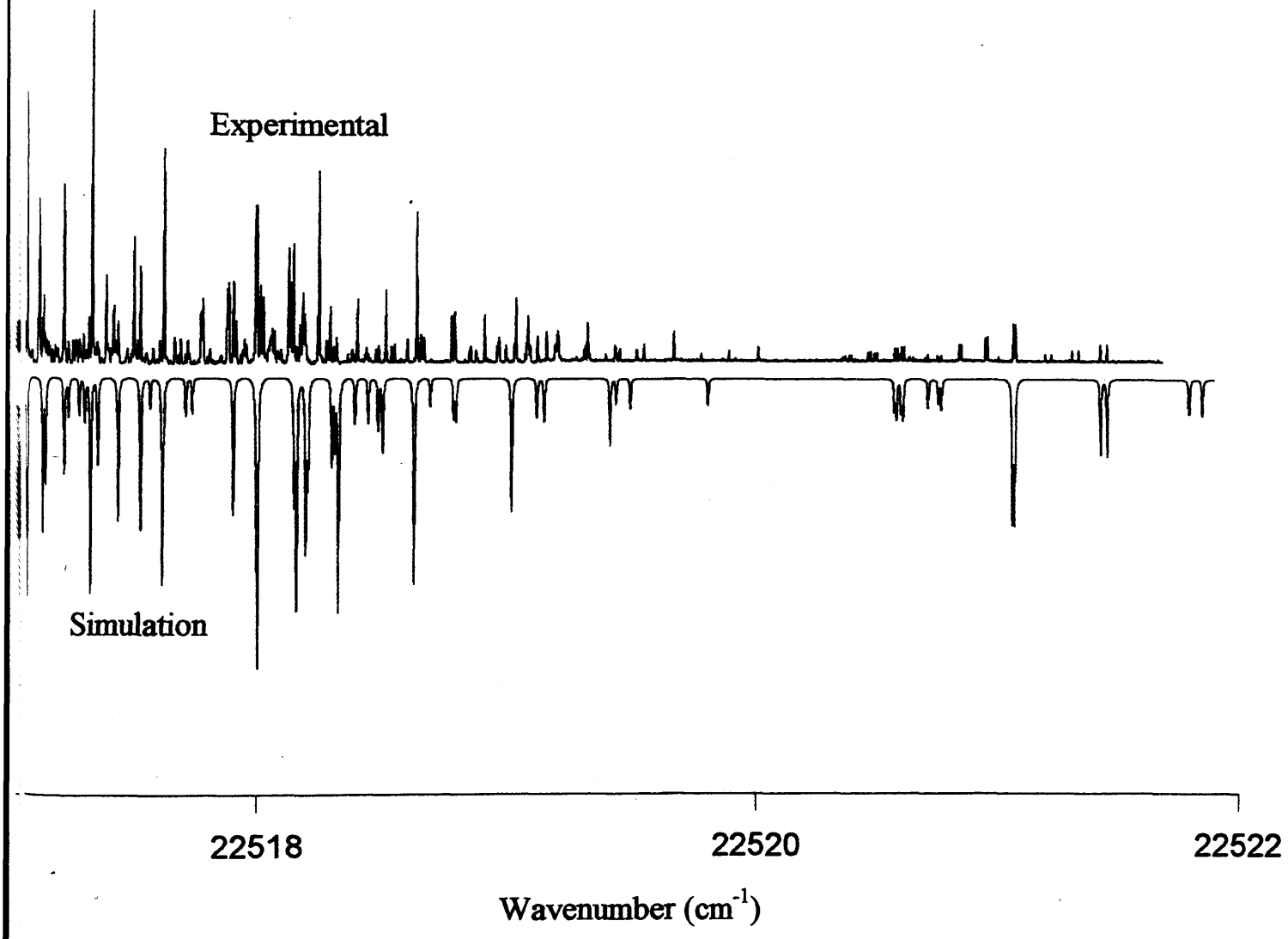

Figure 5.12 Experimental and simulated spectra for part of band A. The constants used for the simulation are given in Table 5.6. Only ^{64}Zn transitions are included in the diagram.

Table 5.6 Rotational constants form simulations of band A for each isotope of zinc assuming a *c*-type transition (cm^{-1})

Constant	^{64}Zn	^{66}Zn	^{68}Zn
T_e	22516.2811	22516.1763	22516.0520
A''	1.0179	1.0134	1.0129
B''	0.1237	0.1224	0.1219
C''	0.1146	0.1134	0.1129
ε_{aa}''	0.0000	0.0000	0.0000
ε_{bb}''	0.004	0.004	0.004
ε_{cc}''	0.004	0.004	0.004
A'	1.0539	1.0521	1.0543
B'	0.1199	0.1215	0.1206
C'	0.1187	0.1173	0.1146
ε_{aa}'	1.3673	1.3762	1.3762
ε_{bb}'	0.0195	0.0300	0.0228
ε_{cc}'	0.1342	0.1546	0.1434

be analysed which was not possible in the current work due to the low rotational temperature.

5.4.3 Band B

The rotational structure of band B (see Figure 5.13) is very similar to that of band A particularly with regard to the relative positions of the $+B$ and $+3B$ structure in the $|\Omega'|=1/2$ component of the (0-1) sub-band. In band B the spin-rotation splitting due to ε_{aa} is slightly bigger than band A which helps the assignment by making the $+B$ structure of the (0-1) sub-band fall at a slightly lower wavenumber than the $|\Omega'|=3/2$ component of the (0-1) sub-band. A simulated spectrum using the rotational constants from the fit of band A (see above) was performed. The only constants changed were T_e and ε_{aa}. A full fit of Band B itself was not attempted as the recorded spectrum does not continue as far as the $|\Omega'|=3/2$ component of the (0-1) sub-band.

5.4.4 Bands C,D and E(i)

These band have been group together as they each contain a further perturbation of the rotational structure. In bands C and E(i) each peak expected from analogy with other bands is broadened. This broadening appears to be caused by a small splitting which is only just resolvable at the resolution employed in this work (~100 MHz). In band D on the other hand the splitting is about 0.01 cm^{-1} which is easily resolvable in this work. The magnitude of the splitting in band D reveals it has an interesting structure (see Figure 5.14). Each line in the $|\Omega'|=1/2$ component of the (1-0) sub-band is split into two lines of approximately equal intensity while each line in the $|\Omega'|=3/2$ component of the (1-0) sub band is split into three lines with approximately a 3:2:2 intensity ratio. Unfortunately it has not been possible to examine other K sub-band due to the limited range of the spectrum recorded combined with the significantly increased spectral congestion making it impossible to assign other sub bands. The resolution of Bands C and E(ii) combined with the much smaller splitting does not allow the precise nature of the splitting in those bands to be determined.

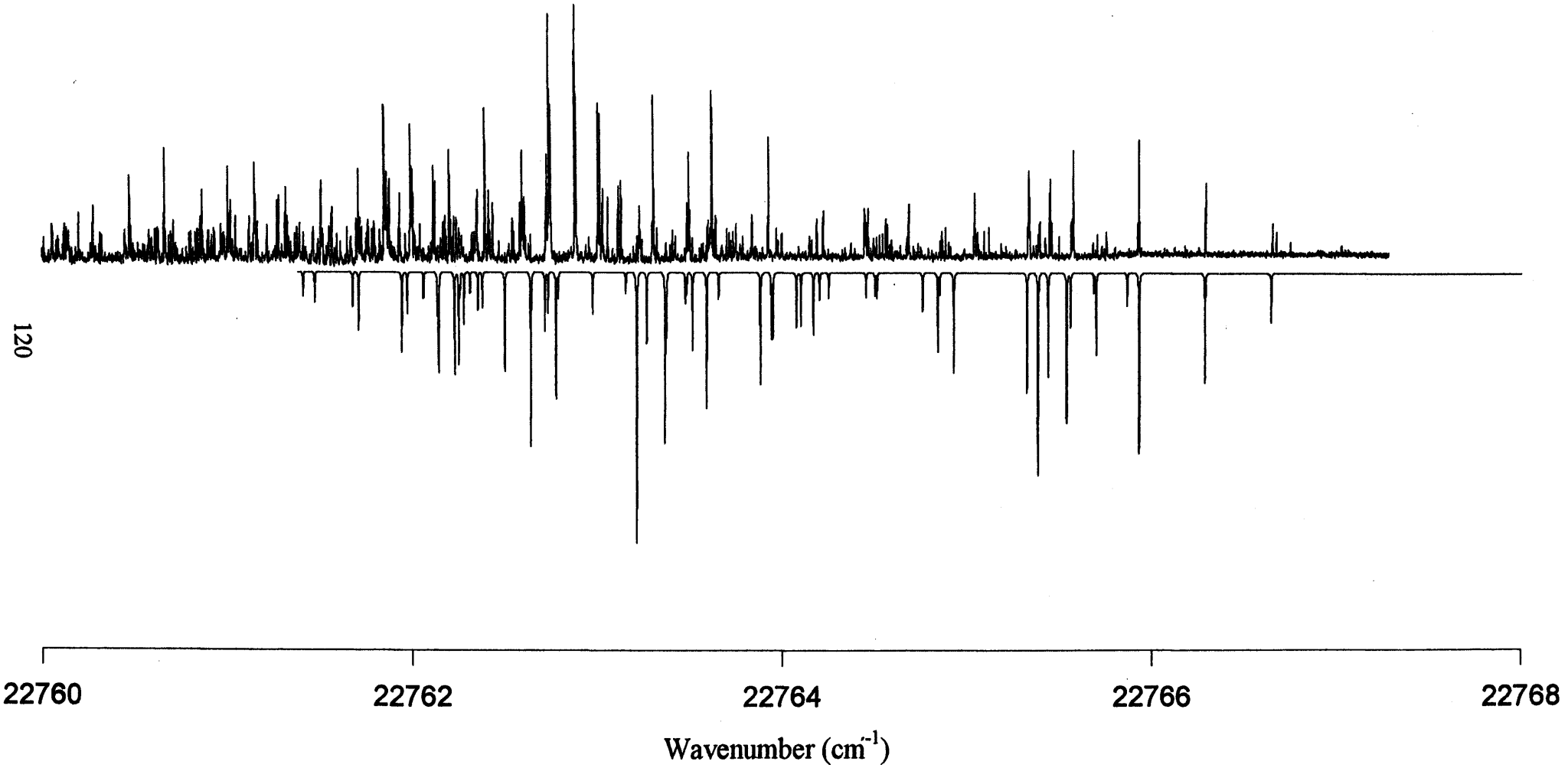

Figure 5.13: Experimental spectrum (top) and a simulation of band B of $^{64}ZnC_2H_5$. Details of the simulation are given in the text

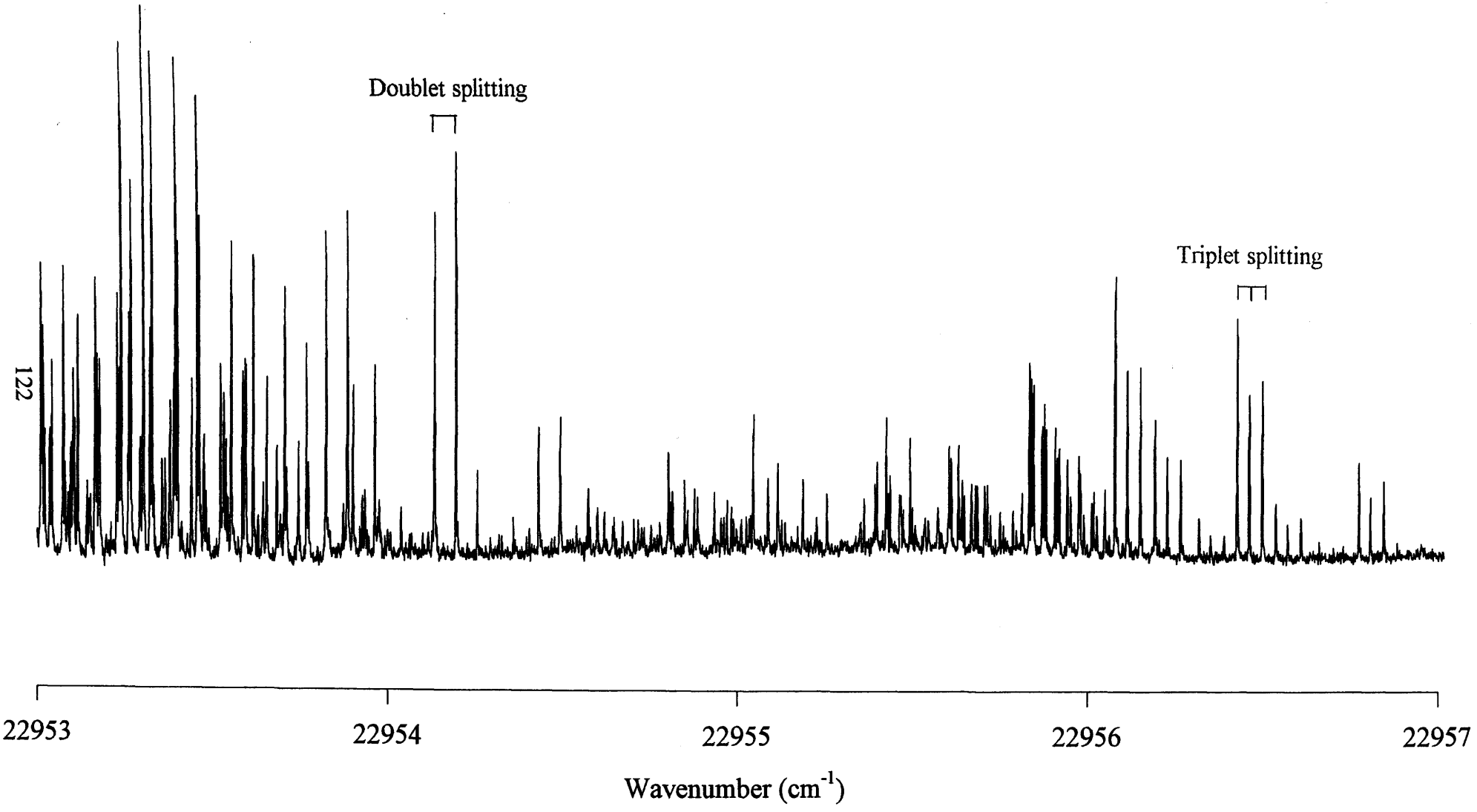

Figure 5.14: Rotationally-resolved spectrum of band D showing the unusual splittings referred to in the text.

One possible source of the splitting, that must be considered is hypefine coupling due to nuclear spin. However, as mentioned previously the three commonest isotopes of zinc, ^{64}Zn, ^{66}Zn and ^{68}Zn have zero nuclear spin and so this theory must be ruled out. A more feasible suggestion may come from looking at the vibrational assignment of band D. The dispersed fluorescence work (Chapter 3) was inconclusive, but the isotopic shift data indicated a probable assignment to two quanta in the methyl torsion. It is therefore possible that the unusual splitting is a methyl tunnelling splitting. The broadening in bands C and E(i) may indicate that these transitions also contain some methyl torsion character, albeit in smaller amounts. This fascinating possibility amounts to little more than speculation at present but is worthy of future investigation.

5.4.4.1 Simulated spectra

The effect of methyl tunnelling splitting have not been included in the ASYMSR model. Consequently, no simulated spectra for bands C, D and E(i) are reported here. Ultimately ASYMSR may need to be modified to incorporate methyl tunneling splittings, something that should be possible in the Leicester spectroscopy group.

5.4.5 Band F

Band F again bares considerable resemblance to Band E(ii) but also has considerable differences. As for all the bands the coarse '+3*B*, +*B*, -*B*, -3*B*' rotational structure is very evident. However, these features are only observed for the $|\Omega'|=3/2$ component of the (1-0) sub-band, *i.e.* no features from any other *K* sub-bands are seen nor is there any sign of the $|\Omega'|=1/2$ component. There are two obvious explanations for this:

i) The $|\Omega'|=1/2$ component has a low (or zero) fluoresce quantum yield, possibly because of pre-dissociation.

ii) ε_{aa} is large so the 1/2 component, along with the other *K* sub-band falls outside the scan range. For this to be the case ε_{aa} would need to be greater than ~4.5 cm^{-1} which is not inconceivable. An argument against this however is the absence of any obvious broadening of Band F in the low resolution excitation spectrum.

5.4.5.1 Simulated spectra

It is possible to generate simulated spectra that match the real spectrum of band F assuming a *b* and a *c*-type transition. The difficulty is that only a few lines can be included in the fit so the rotational constant produced have large standard deviations even though the ground state constants were fixed at those determined from band E(ii). As only one spin-orbit like component is observed it is impossible to determine the value ε_{aa}. Consequently, the fitted spectra for band F have little value and are not considered further.

5.5 Discussion

5.5.1 Geometry

Cerny *et al.*[1] determined the equilibrium geometry of $ZnCH_3$ from the *A* and *B* rotational constants. From rotational resolved spectrathey determined *A* and *B* for three isotopes of zinc but the differences in constants between the isotopes was not sufficiently large to aid in the calculation of geometric parameters. $ZnCH_3$ has three independent geometric parameters. The Zn-C and C-H bond lengths and the Zn-C-H bond angle. From two rotational constants it is obviously impossible to determine all three parameters. The approach adopted by Cerny was to fix the C-H bond lengths. As the transition is mainly zinc localised these assumptions should be quite valid and Cerny deduced the Zn-C bond length and the Zn-C-H bond angle in the $\tilde{X}^2A_1$ and the $_1\tilde{A}^2E$ states.

In going from $ZnCH_3$ ZnC_2H_5 an extra rotational constant can be determined but there is a greater increase in the number of parameters required to specify the geometry. However, if the transition is assumed to be zinc localised, it isreasonable to fix all the C-H bond lengths and the C-C-H and Zn-C-H bond angles can potentially be achieved. But a treatment along these lines has not been performed by the author for two reasons:

(i) The confidence in the determined rotational constants is not high enough to make the geometric parameters calculated reliable.

(ii) The observed rotational constants, particularly the *A* constant, in molecules that have a large spin-rotation coupling, is not purely inversely related to the moment of inertia about the *a* axis. Specifically, the coupling to nearby electronic states gives rise to a second order effect that is discussed in section 5.5.2.1. In ZnC_2H_5 this effect cannot be ignored but also it has not been possible to quantify it. Thus any calculations which use the *A* constant in a geometry determination without accounting for this second order contribution are liable to be misleading.

5.5.2 Determining physical parameters from the spin-rotation components

Before considering the specific spin-rotation constants of ZnC_2H_5, particularly ε_{aa}, it is pertinent to consider what physical parameters can be determined from spin-rotation constants. The model that will be used here follows that described recently by Morbi *et al.*.[12]

The spin-rotation tensor ε arises from two components; a direct magnetic coupling between the electronic spin and molecular motion, and a second order spin-orbit coupling mediated by the electron spin and the unquenched angular momentum of the unpaired electron. It has been shown (Curl,[18] Dixon[19]) that the second order spin-rotation coupling frequency plays the major part in the interaction. Physically, the second order spin-orbit constants, $\varepsilon_{\alpha\alpha}^{(2)}$, for the state l_0 can be interpreted as the sum of the interaction of the state l_0 with other electronic states l_n:

$$\varepsilon_{\alpha\alpha}^{(2)} = \sum_{n\neq 0}\sum_{j}\frac{4B_\alpha k_j \langle\psi_0|\hat{L}_\alpha|\psi_n\rangle\langle\psi_n|\hat{\eta}_{\alpha,j}|\psi_0\rangle}{E_n^o - E_0^0} \qquad (2)$$

where $\alpha = a$, b or c, $B_\alpha = A$, B, or C, and L_α is the projection of the electronic orbital angular momentum, **L**, upon axis α. The sum *j* is over all electrons and the sum *n* is over all states. k_j=+1 for the promotion of an unpaired electron, k_j=-1 for promotion to a half-filled orbital and zero otherwise. The matrix element involving $\hat{\eta}_{\alpha,j}$ can be written in terms of the one electron orbital angular momentum operators, $\hat{\eta}_{\alpha,j} = \varsigma_j \hat{l}_{\alpha,j}$, where ζ_j is the spin-orbit coupling constant for the electron.

In the pure precession limit all electrons are neglected except the unpaired valence electron upon the Zn atom. With this approximation the sum over j can be removed and replaced with a single term, $\varsigma_{4p}\hat{l}_\alpha$, leaving the second order correction to the spin-rotation constant as:

$$\varepsilon_{\alpha\alpha}^{(2)} = \sum_{n\neq 0} \frac{4B_\alpha \langle \psi_0 | \hat{l}_\alpha | \psi_n \rangle \langle \psi_n | \varsigma_{4p} \hat{l}_\alpha | \psi_0 \rangle}{E_n^o - E_0^o} \tag{3}$$

Another approximation that can be made is the unique perturber approximation, where it is assumed that each electronic state interacts solely with a single, dominant perturbing state, all other state being far removed energetically, and therefore making negligible contributions to equation (3). This approximation removes the summation over all states. In the pure precession limit the low lying excited states are treated as pure p-type orbitals upon the zinc atom. Table 5.7 shows the correlation of the electronic state and the principal axis system with the (x, y, z) co-ordinate system of the zinc atom. The interpretation of the spin-rotation constants for the ZnC_2H_5 molecule is further complicated by the lack of molecular symmetry. As ZnC_2H_5 is an asymmetric top molecule the a and b axes defined by the moment of inertia are no longer coincidental with the x and y axes describing the p-orbitals of the zinc atom. The deviation between the axes is small ($<20^0$ from *ab initio* calculations) and in this simplistic treatment is ignored.

Table 5.7

$ZnCH_3$		ZnC_2H_5	
$\tilde{A}^2E \equiv p_x, p_y$	$\tilde{I}_b = \tilde{I}_y$, $\tilde{I}_c = \tilde{I}_x$	$\tilde{A}^2A' \equiv p_x$	$\tilde{I}_c = \tilde{I}_x$
		$\tilde{B}^2A'' \equiv p_y$	$\tilde{I}_b = \tilde{I}_y$
$\tilde{B}^2A_1 \equiv p_z$	$\tilde{I}_a = \tilde{I}_z$	$\tilde{C}^2A' \equiv p_z$	$\tilde{I}_a = \tilde{I}_z$

The diagonal spin-rotation parameter $\varepsilon_{\alpha\alpha}$ arises from a coupling of different electronic states through a rotation about the α axis. If the $\tilde{A}^2A'$ state of $ZnCH_3$ is considered, a rotation about the a (z) axis will couple the $\tilde{A}^2A'$ state with the $\tilde{B}^2A''$

state, a rotation about the *c* (*x*) axis will couple the $\tilde{A}^2A'$ and the $\tilde{C}^2A'$ state. A rotation about the *b* (*y*) axis will not couple the $\tilde{A}^2A'$ state with any other low lying state as the unpaired electron's orbital is symmetric about the b axis and thus the rotation has no effect. Unique perturber approximation, and assuming that the electronic states arise from pure *p*-type orbitals, the one-electron orbital angular momentum operators shown in Table 5.8 can be substituted into equation (3).

Table 5.8

$\tilde{l}_x p_x = 0$	$\tilde{l}_y p_x = -ip_z$	$\tilde{l}_z p_x = ip_y$
$\tilde{l}_x p_y = ip_z$	$\tilde{l}_y p_y = 0$	$\tilde{l}_z p_y = -ip_z$
$\tilde{l}_x p_z = -ip_z$	$\tilde{l}_y p_z = ip_z$	$\tilde{l}_z p_z = 0$

If by way of example we consider ε_{aa} in the $\tilde{A}^2A'$ state of zinc monoethyl, again assuming that the A' is the lowest excited state, after substitution equation (3) becomes equation (4).

$$e_{aa}^{(2)} = \frac{4A\langle p_y|l_z|p_x\rangle\langle p_x|V_{3p}l_z|p_y\rangle}{E_{\tilde{B}} - E_{\tilde{A}}} \qquad (4)$$

$$= \frac{-4AV_{3p}i^2}{E_{\tilde{B}} - E_{\tilde{A}}} = \frac{+4AA^{SO}}{E_{\tilde{B}} - E_{\tilde{A}}}$$

In the final step ζ_{3p} was replaced with A^{SO} which is the spin-orbit splitting in the hypothetical linear molecule. It can seen that ε_{aa} in the $\tilde{B}^2A''$ state is the negative of equation (4). Table 5.9 summarises expressions for the spin-rotation parameters, $\varepsilon_{\alpha\alpha}$, in the $\tilde{A}^2A'$ and $\tilde{B}^2A''$ states; the parameters for the $\tilde{C}^2A'$ state are not listed as the state has not been observed. To obtain these expressions the implied ordering of states has been assumed and so if the $2A''$ is lower than the first excited $2A'$ state then the signs of certain terms will be reversed.

Table 5.9 Expressions for the spin-rotation constants

$\tilde{A}^2A'$		
$\varepsilon_{aa}^{(2)} = \dfrac{+4AA^{SO}}{E_{\tilde{B}} - E_{\tilde{A}}}$	$\varepsilon_{bb}^{(2)} = 0$	$\varepsilon_{cc}^{(2)} = \dfrac{+4CA^{SO}}{E_{\tilde{C}} - E_{\tilde{A}}}$
$\tilde{B}^2A''$		
$\varepsilon_{aa}^{(2)} = \dfrac{-4AA^{SO}}{E_{\tilde{B}} - E_{\tilde{A}}}$	$\varepsilon_{bb}^{(2)} = \dfrac{+4BA^{SO}}{E_{\tilde{C}} - E_{\tilde{B}}}$	$\varepsilon_{cc}^{(2)} = 0$

5.5.2.1 Second order correction to rotational constants

A second order term caused by the interaction of one or more electronic states with an electronic state also affects the magnitude of the rotational constants (*A*, *B*, and *C*). Using a similar analysis to that described above for the second order spin-rotation the second order correction of the rotational constants was again shown by Morbi *et al.*[12] to be

$$B_a^{(2)} = \sum_{n \neq 0} \frac{4B_a^2 \langle y_0 | \tilde{l}_a | y_n \rangle^2}{E_0^o - E_n^o} \qquad (5)$$

where B_α is again the rotational constant about the principal axis α and the other parameters were defined above in the spin-rotation discussion. Using the same assumptions of a pure precession model and the unique perturber approximation it can be shown the second order corrections of the rotational constants for the $\tilde{A}^2A'$ and $\tilde{B}^2A''$ states are shown in Table 5.10. It is again assumed that the 2A′ state is lower in energy than the 2A″ state.

Table 5.10 Expressions for the second-order correction of rotational constants

$\tilde{A}^2A'$		
$A^{(2)} = \frac{\pm 4A^2}{E_{\tilde{A}} - E_{\tilde{B}}}$	$B^{(2)} = 0$	$C^{(2)} = \frac{+4C^2}{E_{\tilde{C}} - E_{\tilde{A}}}$
$\tilde{B}^2A''$		
$A^{(2)} = \frac{\pm 4A^2}{E_{\tilde{A}} - E_{\tilde{B}}}$	$B^{(2)} = \frac{+4B^2}{E_{\tilde{C}} - E_{\tilde{B}}}$	$C^{(2)} = 0$

In both states the second-order correction to the A constant is likely to be significant as the difference in energy between the $\tilde{A}$ and $\tilde{B}$ states is the smallest and the A constant is large. While the second order corrections to the B and C rotational constants are likely to be insignificant for two reasons:

(i) The magnitude depends upon the square of the rotational constant and the B and C constant are an order of magnitude smaller than the A constant.

(ii) The separation between the A/B states and the C state is significantly greater then the separation between the B and C states.

5.5.2.3 Spin rotation parameters in $ZnCH_3$

Before considering the spin-rotation parameters for ZnC_2H_5, it is worth reviewing the spin-rotation constants of $ZnCH_3$ reported by Cerny *et al.*.[7] In this paper they investigated the $\tilde{A}^2E$ - $\tilde{X}A_1$ transition. They commented upon the value of ε_{aa} and reported the value of ε_{bc} to be -1.343 cm^{-1} in the $\tilde{A}^2E$ state, but did not interpret the physical significance of this value. ε_{bc} is analogous to ε_{bb} and ε_{cc} ($\varepsilon_{bc}=(\varepsilon_{bb}+\varepsilon_{cc})$) in ZnC_2H_5, described above as $ZnCH_3$ is a prolate symmetric top and, in a similar way it can be shown that second order spin-orbit correction to the spin-rotation constants are given by equation (6) below. Again a pure precession model and the unique perturber approximation in which the $\tilde{A}^2E$ state is perturbed solely by the B^2A' (p_z) state are assumed.

$$\varepsilon_{bc}^{(2)} = \frac{4A\langle p_z|\hat{l}_x|p_x\rangle\langle p_x|\varsigma_{4p}\hat{l}_z|p_z\rangle}{E_{\tilde{B}} - E_{\tilde{A}}} \qquad (6)$$

$$= \frac{4BA^{SO}}{E_{\tilde{B}} - E_{\tilde{A}}}$$

A^{SO} is the spin-orbit splitting in the hypothetical linear molecule. Although a value for the spin-orbit splitting for the $\tilde{A}^2E$ state of $ZnCH_3$ is known, the Jahn Teller distortions within the molecule affect the value so that it is no great use in this calculation. Instead the value taken from ZnH is used (342 cm^{-1}).[20] This assumption should not be too great as the states $\tilde{A}^2E$ and $\tilde{B}^2A_1$ states (analogous to the $A^2\Pi$ and $B^2\Sigma^+$ states in ZnH) involved in the coupling are both largely non-bonding and metal localised in character. Using the value for ε_{bc} of Cerny *et al.* and equation (6) an energy separation, ΔE, between the $\tilde{A}^2E$ and the B^2A_1 states of 3454 cm^{-1} is deduced. This separation is consistent with the separation between the related $A^2\Pi$ and $B^2\Sigma^+$ states in ZnH (4318 cm^{-1}). Unfortunately, the $\tilde{B}^2A_1$ state has not yet observed so the exact separation of the states awaits determination.

5.5.2.4 ε_{aa} in ZnC_2H_5

All of the spin-rotation constants in the ground electronic state of ZnC_2H_5 are, like those of $ZnCH_3$, expected to be small because of the large energy separation between this state and all higher doublet states. However, the proximaty of excited states leads one to expect much larger spin-rotation constants in the excited states. In particular, ε_{aa} in the $\tilde{A}$ and $\tilde{B}$ states of ZnC_2H_5 might be quite large because of the likely small energy separation between the states. This proposition is bourne out by the results shown earlier.

The values of ε_{bb} and ε_{cc} reported for $ZnCH_3$ in Table 5.11 are identical as $ZnCH_3$, is an symmetric top. As can be seen the agreement is quite good with the only significant difference being the sign of ε_{bc}'. Although the agreement in ε_{aa}' is excellent this is not a fair comparison due to the differing electronic structures of the two molecules.

Table 5.11 Comparison of spin-rotation constants of $ZnCH_3$ and ZnC_2H_5 (extracted from band E(ii))

Spin-rotation constant	$^{68}ZnCH_3$	$^{68}ZnC_2H_5$
ε_{aa}''	0	0
ε_{bb}''	0.0119	0.004
ε_{cc}''	0.0119	0.004
ε_{aa}'	2.72	2.7245
ε_{bb}'	-0.1334	0.1561
ε_{cc}'	-0.1334	0.1667

Miller and co-workers have reported the molecular constants for $CdCH_3$, $ZnCH_3$[1] and $MgCH_3$[13] in which a negative value of ε_{bc}' has been deduced from simulations for all three molecules. While Bernath and co-workers and Stimle and co-worker have reported a positive value of ε_{bb}' and ε_{cc}' in their work on various low lying states of CaSH and $CaNH_2$.[10-14] (But note the sign of ε_{aa}' is well established).

The expressions for the spin-rotation constants of the $\tilde{A}$ and $\tilde{B}$ states of ZnC_2H_5, given earlier in Table 5.10, theory suggests that ε_{bb} and ε_{cc} should have a positive value as they are a measure of the interaction a low lying electronic state with the p_z orbital on zinc which is expected to be a higher energy than the $4p_x$ and $4p_y$ orbitals. The value for the $\tilde{A}$ state of ZnC_2H_5 obtained within this work are consistent with this idea.

5.5.2.5 Trends in the value of ε_{aa}

The table below (Table 5.12) shows the approximate value of ε_{aa}' deduced from the bands A-F.

Table 5.12 Table showing the values of ε_{aa} for all bands

Band	ε_{aa} (cm^{-1})
Origin	1.4
1	2.5
2	2.5
3	2.6
4A	0.8
4B	2.6
5	unknown

There is clearly a large jump in values in moving from band A to band B but the remaining values are all pretty much the same with the exception of band E(i). Possible explanations of these findings will now be given.

5.5.2.6 ε_{aa} in the $\tilde{A}-\tilde{X}$ electronic origin band(band A)

The unique perturber, pure pression expression for ε_{aa} in the $\tilde{A}$ state is

$$\varepsilon_{aa}^{(2)} = \frac{+4AA^{SO}}{E_{\tilde{B}} - E_{\tilde{A}}} \tag{7}$$

Employing the experimental value of the A rotational constant and using the spin-orbit coupling constant in the $A^2\Pi$ state of ZnH (342 cm^{-1}) as an approximation for A^{SO} of ZnC_2H_5, it is possible to determine the energy separation between the $\tilde{A}$ and $\tilde{B}$ states. The value of A used in the calculation was that determined from the simulation assuming a *c*-type transition (1.0539 cm^{-1}). It would be more appropriate to use the value that has been corrected by removing any second order contribution to A from the interaction of nearby states, (see section 5.5.2.1) but since the $\tilde{A}-\tilde{B}$ energy separation is needed for this calculation this is impossible. Ignoring the second order contribution to A gives a value of 1054 cm^{-1} for the separation of the $\tilde{A}$ and $\tilde{B}$ states, *i.e.* the $\tilde{B}-\tilde{X}$ electronic origin is estimated to be at about 23572 cm^{-1}.

There is a peak in the excitation spectrum reported by Povey at 23526 cm^{-1} but the dispersed fluorescence spectrum recorded pumping this transition suggests that it is a vibrartional feature in the $\widetilde{A}$-$\widetilde{X}$ system. There is also a weaker peak at ~23600 cm^{-1} which is partially obscured by $A^2\Pi$-$X^2\Sigma^+$ transition of ZnH which might be the $\widetilde{B}-\widetilde{X}$ origin. It is possible that the $\widetilde{B}$ state does not fluoresce perhaps because of competitive pre-dissociation. In a recent paper by Bezant and Ellis[21] the $\widetilde{A}$-$\widetilde{X}$ system of the related molecule CdC_2H_5 was investigated. In this work only the electronic origin was observed and the lack of vibrational structure was attributed to pre-dissociation.

It should be noted here that the interpretation of spin-rotation constants given above makes a number of questionable assumptions. Possibly one of the largest sources of error is the assumption that the spin-rotation coupling is purely an interaction between two levels, other nearby electronic states are not considered nor are vibrational levels within the same electronic states considered. If the observed spin-rotation splitting was achieved from an interaction with more than one electronic state, or several vibrational levels within the same electronic state, the theory is likely to predict a energy separation that is smaller than it is in reality. Field and Lefebrufe[22] in their book "Perturbations in the spectra of Diatomic Molecule" have considered interactions between electronic states close in energy and concluded that a Frank-Condon factor should be included as part of the calculation of the interaction between states.

5.5.2.7 ε_{aa} in bands B-E(ii)

ε_{aa}' is found to be positive in all of these bands which indicates that each of these levels interact with another electronic state or at least a vibrational level of another electronic state that is higher in energy. Band C-E(ii) are all reasonably close in energy so that if the upper electronic state is the same for each band then the ε_{aa}' should be very similar for each. This also assumes that the rotation constant A' does not vary significantly from band to band. This scenario seems to be the case for bands C, D and E(ii). Using equation (7) and the A' and ε_{aa}' values for band E(ii), and gives a ΔE of 550 cm^{-1}. This separation would put upper state of the interaction

at 23546 cm^{-1}, which is very close to that predicted from the ε_{aa}' deduced from the $\tilde{A}-\tilde{X}$ electronic origin (23572 cm^{-1}).

The value ε_{aa}' in band E(i) does not fall in to this general trend, being much smaller than in the other bands in the same region. The most obvious explanation is than band E(i) has a poor Franck-Condon overlap with the $\tilde{B}-\tilde{X}$ origin band so the observed splitting would be smaller as the interaction is smaller.

5.6 Future work

This chapter describes the rotationally resolved spectroscopy of ZnC_2H_5. Assignments of spectra are, in many cases, obvious far from complete. Band E(ii) is the most fully understood but even in this case the structure of the (0-1) *K* sub-band could not be ascertained. Unfortunately this meant that there are still uncertainties regarding spectroscopic constants and even the type of transition is has not been firmly established. Similarly, and usually more serve, problems have been encountered for the other rotationally resolved bands. There are further experiments that could be performed to improve assignments. LIF spectra recorded under higher temperature conditions might make it easier to locate additional sub-bands, especially the (0-1). Experiments using deuterated diethyl zinc precursor might also be of some assistance, although these would require a difficult and expensive synthesis to produce this precursor.

Finally, we feel that the unusual splittings in band C, and the possibly related splittings in bands B and E(i) are deserving of further work. The author has suggested that these splittings may arise from the hindered rotation of the methyl group. This type of splitting has not been observed in any of the previous rotationally resolved spectroscopic studies of metal-containing free-radicals.

References

1 R.L. Jackson, *Chem. Phys. Lett.* **92**, 807 (1990)

2 R.L. Jackson, *Chem. Phys. Lett.* **96**, 5938 (1992)

3 R.L. Jackson, *J. Chem. Phys.*, **96**, 5938 (1992)

4 P.F. Seider, *J. Phys. Chem.*, **98**, 2095 (1994)

5 I.M. Povey, A.J. Bezant, G.K. Corlett, and A.M. Ellis, *J. Phys. Chem.*, **98**, 10427 (1994)

6 S.J. Pooley, and A.M. Ellis, *J. Mol. Spectrosc.*, **185**, 48 (1997)

7 T.M. Cerny, X.Q. Tan, J.M. Williamson, E.S.J. Robles, A.M. Ellis and T.A. Miller, *J. Chem. Phys.I*, **99**, 12 (1993)

8 E.S.J Robles, A.M. Ellis, and T.A. Miller, *Chem Phys Lett.*, **178**, 185 (1993)

9 C.J. Whitham, and C.H. Jungen, *J. Chem. Phys.*, **93**, 2 (1990)

10 A.J. Marr, M. Tanimoto, D. Goodridge, and T.C. Steimle, *J. Mol. Spectrosc.*, **176**, 268 (1996)

11 C. Zhao, P.G. Hajigeorgiou, P.F. Bernath, and J.W. Hepburn, *J. Mol. Spectosc.*, **176**, 268 (1996)

12 Z. Morbi, C. Zhao, and P.F. Bernath, *J. Chem. Phys.*, **106**, 12 (1997)

13 C.N. Jarman, and P.F.Bernath, *J. Chem. Phys.***98**, 9 (1993)

14 C.T. Scurlock, T. Henderson, S. Bosely, K.Y. Jung, and T.C. Steimle, *J. Chem. Phys.*, **100**, 15 (1994)

15 D.W. Cullin, L. Yu, J.M. Williamson, M.S. Platz and T.A. Miller, *J. Phys. Chem.*, **94**, 3387 (1991)

16 J.H. Van Vleck, *Rev. Mod. Phys.*, **23**, 213 (1951)

17 J.M. Brown and T.J. Sears, *J. Mol. Spectrosc.*, **75**, 111 (1979)

19 R.F. Curl, *Mol. Phys.*, **9**, 585 (1965)

20 K.P. Huber and G. Hertzberg, *Molecular Spectra and Molecular Structure. IV. Constants for Diatomic molecules,* Van Nostrand Reinhold, New York, p. 679 (1979)

21 A.J. Bezant and A.M. Ellis, *J. Mol. Spectrosc.*, **185**, 54 (1997)

Chapter Six

LIF spectroscopy of the BaOH free-radical

6.1 Introduction

The alkaline-earth monoxides and monohydroxides initially attracted attention in the early 1950's because of the intense colours that resulted from adding alkaline-earth salts to a flame. In 1955 James and Sugden[1] proposed that, while a number of emission bands in the visible and near-infrared were due to the monoxides of the alkaline-earth metals, the most intense bands probably arose from electronic transitions in the metal monohydroxide. Following on from this suggestion, Charton and Gaydon[2] studied the more intense flame emission band systems in the green, red and near-IR regions of the spectrum originating from addition of barium salts to a flame. Barium monohydroxide was assigned conclusively as the spectral carrier by observing small shifts in the emission lines due to deuterated analogues of the molecules.

The development of laser-induced fluorescence spectroscopy (LIF) in the mid-1970's introduced an alternative method for investigating short-lived molecular species. Flame species could now be selectively excited using narrow laser bandwidths and studied with, potentially, much higher resolution. Haraguchi and co-workers[3] re-investigated the band systems in the green and near-IR regions for barium-containing flames using LIF spectroscopy. They observed overlapping spectra, attributed to contributions from both BaO and BaOH, in the 18500 - 21000 cm^{-1} region. The bands arising from the $A^1\Sigma$ - $X^1\Sigma$ system of BaO were easily identified as the band contours of the rotational structure strong red-shading. Two broad emission bands, that were not red-shaded, were also observed, centred at ~19500 cm^{-1} and ~20500 cm^{-1} respectively, which are at the same positions as the $\tilde{C}^2\Pi - \tilde{X}^2\Sigma^+$ bands of BaOH assigned by James and Sugden in the 1950s.[1] There was insufficient resolution for a rigorous assignment in the LIF work of Haraguchi *et al.*,[3] and therefore these two bands were attributed to BaOH by analogy with the earlier work by James and Sugden.[1]

Although flames are an obvious source of short-lived molecules and radicals, they present a serious disadvantage to the high-resolution spectroscopist. The high temperatures in flames can cause severe spectral congestion. Cooler samples (close to room temperature) of metal-containing molecules can be obtained with a Broida

oven and Bernath[4] in particular has exploited this to obtain electronic spectra of many monoligated compounds of the alkaline-earth metals, including the monohydroxides. This work showed these radicals were linear in the ground and excited states observed and the alkaline-earth monohydroxides have very similar electronic structures to the halide analogues.

An alternative method for making metal-containing molecules employs laser ablation. This is easily combined with a supersonic nozzle and the dramatic cooling this confers creates an excellent environment for spectroscopic observations. Recently Pereira and Levy used both LIF and REMPI (resonance enhance multiphoton ionisation) combined with a laser ablation/supersonic jet assembly to investigate the higher states of CaOH.[5] Of the three new excited electronic states discovered, they found the first evidence for a bent, covalent state in an alkaline earth monohydroxide.

In this chapter the application of a laser ablation nozzle in the study of excited electronic states of the BaOH free radical is described. The $\widetilde{X}^2\Sigma^+$, $\widetilde{A}^2\Pi$, and $\widetilde{B}^2\Sigma^+$ states of BaOH have all been investigated in some detail in previous studies with the rotational constants and the Ba-O stretching frequency and the Ba-O-H bending frequency being reported.[6,7] Beside these, the only other excited state which has been identified has been the $\widetilde{C}$ state. However, as discussed above, previous work on the $\widetilde{C}-\widetilde{X}$ system involved very low resolution spectroscopy and no spectroscopic constants could be extracted. Indeed, even the symmetry of the $\widetilde{C}$ state of BaOH is unknown. This chapter is composed of two parts. First, a new transition of BaOH, identified as the $\widetilde{D}^2\Sigma^+ - \widetilde{X}^2\Sigma^+$ system, is reported for the first time. Second the findings from a reinvestigation of the $\widetilde{C}-\widetilde{X}$ region are presented. The latter turns out to be more complicated than expected by analogy with the valence isoelectronic molecule BaF, and possible reasons for this apparent discrepancy are discussed.

6.2 Experimental

The experiments were carried out using the techniques described in chapter 2 so details here are deliberately concise. BaOH was prepared by laser ablation of barium metal within an aluminium fixture, which was itself attached to a pulsed valve (general

valve series 9). Hydrogen peroxide was seeded into helium carrier gas flowing over the metal surface to help form BaOH in initial experiments, but it was subsequently found that this had little impact on the BaOH concentration. Presumably, this was due to traces of water in the carrier gas and/or on the metal surface. In a typical experiment, pulses with energies in the region of 30 mJ from an ArF excimer laser (Lambda Physik, model Compex 100) were softly focused onto the barium surface in synchronisation with the arrival of gas pulses from the pulsed valve. The mixture was then expanded into a Roots-pumped vacuum chamber to form a supersonic jet.

The expanding jet was crossed by the beam from a pulsed dye laser (Lambda Physik Scanmate 2E, pumped by a Continuum Surelite Nd:YAG laser) about 25 mm downstream of the fixture. In the current work, the dye laser was operated without an intracavity etalon giving a linewidth of ~0.2 cm^{-1}. Excitation spectra were obtained by detecting the total fluorescence transmitted by a f/1.3 collection lens on to a Hammamatsu R562 photomultiplier tube (PMT). Where helpful, long-pass filters were placed between the lens and the PMT to reduce the signal due to scattered dye laser light. Dispersed fluorescence spectra were obtained by passing the fluorescence into a 0.27 m monochromator (Acton Research) equipped with a PMT detector. All PMT signals were amplified (SRS 545 preamplifier), digitised by a CAMAC-based transient recorder (LeCroy 2262), and then transferred to a PC. Gated integration and multiple shot averaging was achieved by home-written software routines.

6.3 The $\tilde{D}^2\Sigma^+ - \tilde{X}^2\Sigma^+$ system

6.3.1 Vibrational structure

An LIF excitation spectrum covering the range 22700 - 24400 cm^{-1} is shown in Figure 6.1. Three distinct band groups can be identified in the spectrum, centred at 23057, 23622 and 24172 cm^{-1}. The spectral carrier is undoubtedly barium-containing since no LIF signal was observed when the barium target was removed. Several conceivable barium-containing molecules could be the spectral carrier, but it is easily confirmed to be BaOH using dispersed fluorescence spectroscopy. The dispersed fluorescence spectrum obtained by pumping the 23057 cm^{-1} band, shown in Figure 6.2(a), exhibits a short progression of interval 495 ± 5 cm^{-1}. Kinsey-Nielson *et al.*[6] obtained a value of 495 cm^{-1} for the Ba-O stretch (ν_3) in the $\tilde{X}^2\Sigma^+$ ground electronic

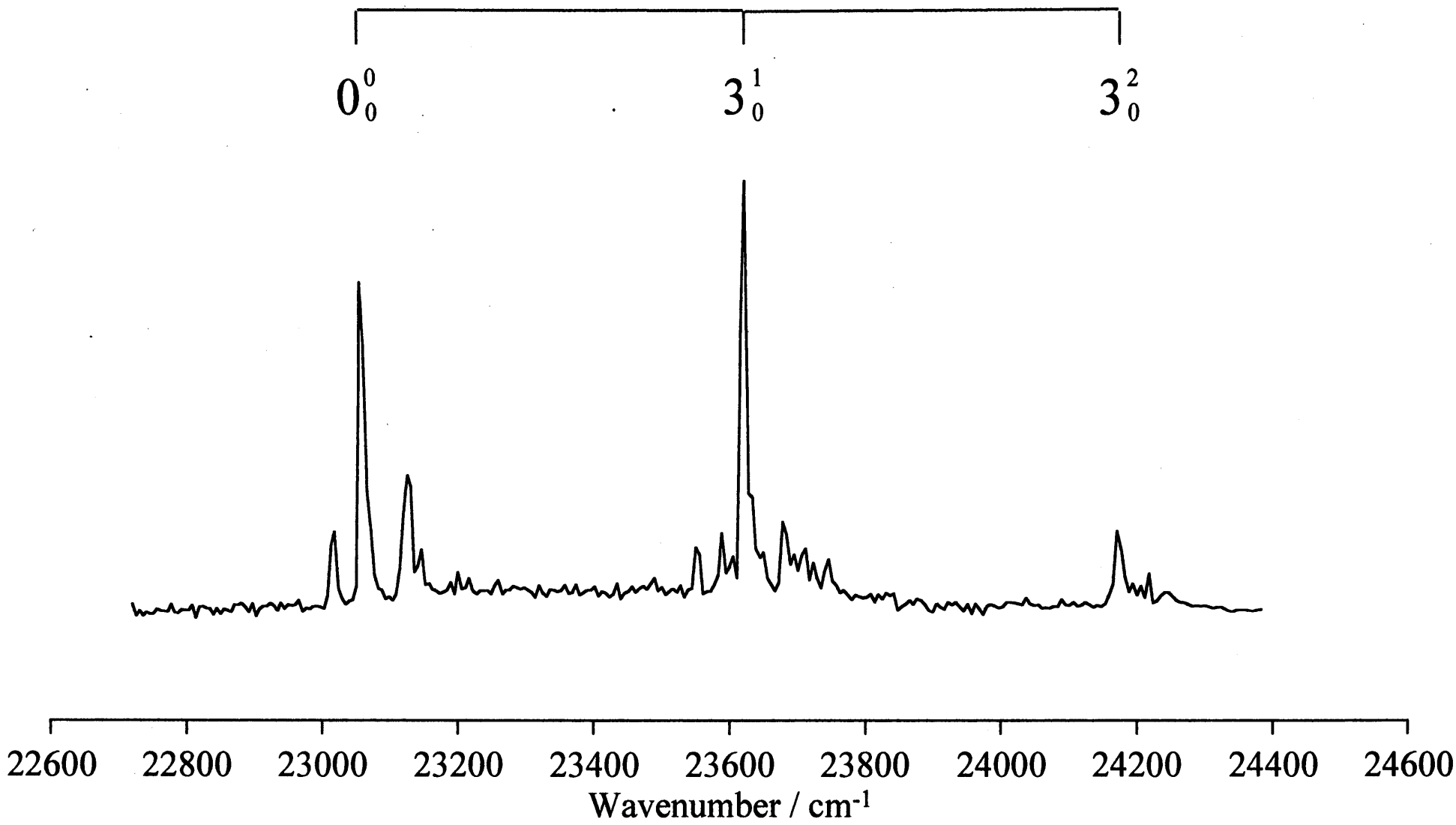

Figure 6.1 Excitation spectrum of the $\tilde{D}^2\Sigma^+ - \tilde{X}^2\Sigma^+$ transition of BaOH. A progression in the Ba-O stretch can be seen.

state of BaOH and so we assign the progression in Figure 6.2(a) to ν_3 in BaOH. Kinsey-Nielson *et al.* also reported a frequency of 661.1 cm^{-1} for two quanta in the Ba-O-H bending mode (ν_2). This correlates well with a very weak peak some 660 ± 5 cm^{-1} to the red of the pump position in our dispersed fluorescence spectrum. The Ba-O-H bend is a non-totally symmetric vibrational mode and therefore single quantum excitation of this mode is forbidden in the Franck-Condon limit. In fact a very weak but reproducible band, identified in Figure 6.2(a), is observed at the single quantum position for the Ba-O-H bend. This must gain intensity through a vibronic coupling mechanism.

No electronic spectra of BaOH have been reported previously in the region shown in Figure 6.1, hence this system is a new one. Since it lies above the $\tilde{C}-\tilde{X}$ system (see later) we refer to it as the $\tilde{D}-\tilde{X}$ system of BaOH. The peak at 23057 cm^{-1} in the excitation spectrum is assigned as the 0_0^0 band of this $\tilde{D}-\tilde{X}$ system, since no additional bands of any significant intensity were observed in the 22000-23000 cm^{-1} region. Since the Ba-O stretch is the major Franck-Condon active mode in the dispersed fluorescence spectrum, the same should be true in the excitation spectrum. We therefore assign the bands at 23057, 23622, and 24172 cm^{-1} to a progression in the Ba-O stretch. This gives a Ba-O stretching frequency in the excited state of 563 cm^{-1}, significantly larger than the ground electronic state. Confirmation of this assignment is provided by the dispersed fluorescence spectrum obtained by pumping the 23622 cm^{-1} transition, assigned to the 3_0^1 transition, which as expected shows a clear enhancement in the Ba-O stretching progression (see Figure 6.2(b)).

In addition to the main progression, sequence bands can also be seen in Figure 6.1. The band immediately to the blue (+69 cm^{-1}) of the 0_0^0 band is consistent with the 3_1^1 transition using the Ba-O stretching frequencies of the $\tilde{X}$ and $\tilde{D}$ states quoted earlier. The band to the red (-40 cm^{-1}) may be the 2_1^1 sequence transition in the Ba-O-H bending mode, since the only other unaccounted for mode, the O-H stretch (ν_1), has a much higher frequency and its excited vibrational levels are therefore unlikely to have significant populations. If correct, this would give a frequency of 290 cm^{-1} for

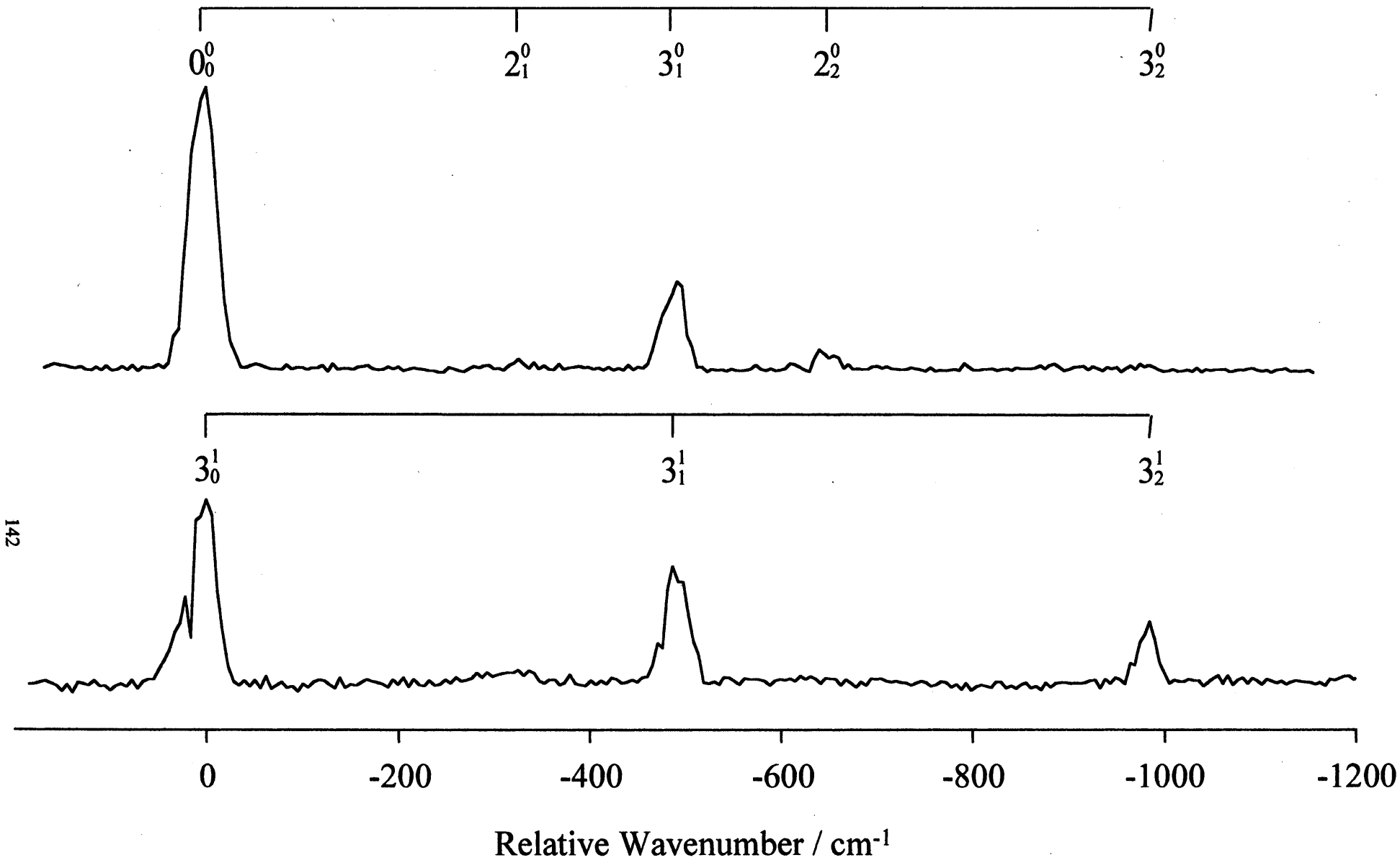

Figure 6.2 Dispersed fluorescence spectrum pumping transitions at (a) 23057 cm^{-1} and (b) 23622 cm^{-1}

the Ba-O-H bend in the $\tilde{D}$ state when combined with the known frequency of this mode in the ground electronic state.[6]

6.3.2 Electronic state assignment

The spectrum shown in Figure 6.1 is a new electronic band system of BaOH. To assign the excited state symmetry, a comparison with the well-studied molecule BaF is valuable. Since BaOH is isoelectronic with BaF, it is reasonable to assume that their electronic states will show strong similarities. A comparison of the energies of the known electronic states of the two molecules is given in Figure 6.3. This figure shows that the origin of the new state of BaOH observed in this work, at 23057 cm^{-1}, is at a similar position to that of the $D^2\Sigma^+$ state of BaF (24177 cm^{-1} for the origin[8]). Since all other states of BaF are either much higher, or much lower, in energy the BaOH excitation spectrum in Figure 6.1 is most likely due to the $\tilde{D}^2\Sigma^+ - \tilde{X}^2\Sigma^+$ transition of BaOH. This is consistent with the lack of any observable spin-orbit splitting in the spectrum.

6.3.3 Rotational contours

The assignment to the $\tilde{D}^2\Sigma^+ - \tilde{X}^2\Sigma^+$ transition of BaOH is also consistent with the rotational contours of the individual bands. Rotational structure was not resolved, but the rotational contours of each band showed clear *P*- and *R*-branches but no *Q*-branch, as would be expected for a $^2\Sigma$-$^2\Sigma$ transition. An approximate rotational constant for the excited state could be extracted by simulating the rotational contour. Fixing the ground state rotational constant at its known value (0.2166 cm^{-1} from reference 6), a best visual match between simulated and observed contours was obtained for B_0' of 0.255 cm^{-1}, with an estimated error range of ± 0.005 cm^{-1}.

If it is assumed that the O-H bond length does not alter significantly on electronic excitation, the increase in rotational constant is due to a decrease in the Ba-O bond length. This is consistent with the increase in the Ba-O stretching vibrational frequency seen on $\tilde{D} \leftarrow \tilde{X}$ excitation, implying a strengthening of the Ba-O bond. Comparable behaviour is observed for BaF,[9] thus further supporting the BaOH assignment.

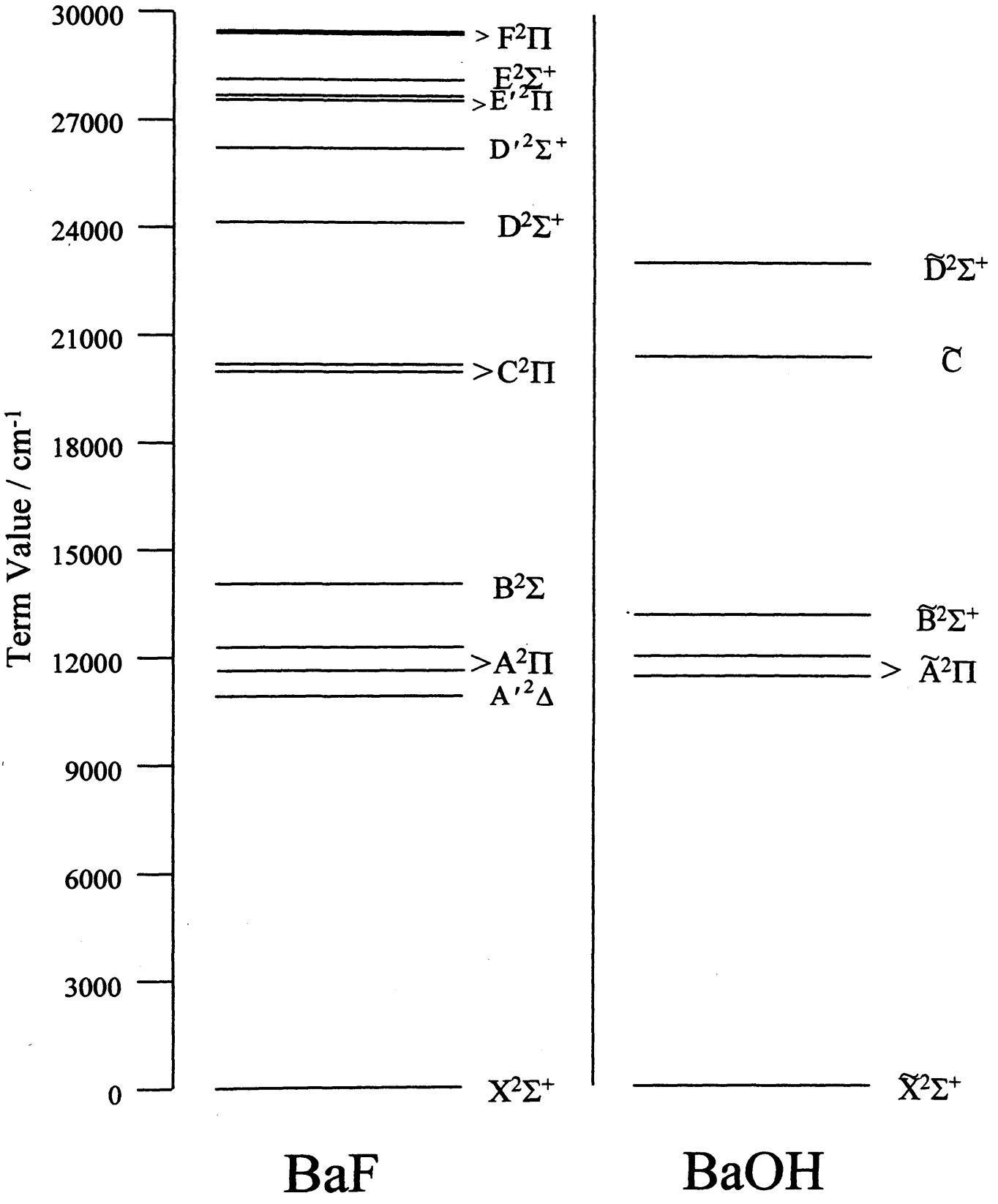

Figure 6.3 Comparison of the energies of the known electronic states of BaF and BaOH T_e term values taken from reference 8, are shown.

6.4 The $\widetilde{C}-\widetilde{X}$ region

Attention now focused upon the $\widetilde{C}-\widetilde{X}$ system of BaOH. As mentioned in the introduction, this system is, in conjunction with BaO, thought to be responsible for the green colour of barium-containing flames and is therefore of considerable interest. However, in earlier spectroscopic work no firm assignments were made other than identifying bands at 487 and 512 nm in the emission spectrum (20530 and 19530 cm^{-1} respectively) as being due to BaOH.[1-3] In the supersonic jet work reported in this chapter LIF survey scans which included this region were performed. First, the coarse structure in the spectrum is considered, and then move on to discuss rotational structure and possible assignments.

6.4.1 Identifying the BaOH bands

Figure 6.4 shows the LIF excitation spectrum recorded between 20000-21500 cm^{-1}. Several strong bands are observed together with many weaker ones. There are two contributors to this spectrum, BaO and BaOH. The BaO $A^1\Sigma$-$X^1\Sigma$ electronic transition overlaps this region. This system is characterised by a long vibrational progression and strongly red-shaded vibronic bands. It is therefore easy to identify the BaO transitions and these are responsible for a number of very weak bands in Figure 6.4. However, the strong bands clearly do not arise from BaO and are therefore attributed to BaOH. The fluorescence lifetimes of vibrational feature in the BaO $A^1\Sigma$-$X^1\Sigma$ system are observed at >200 ns while the fluorescence lifetime of peaks assigned to BaOH is about 50 ns.

The four strongest bands span the region between 20240 and 20620 cm^{-1}. These seem to form two spin-orbit doublets, one being the 20270/20548 cm^{-1} pair and the other the 20355/20605 cm^{-1} pair. If correct, these imply spin-orbit splittings of 278 and 250 cm^{-1}, respectively. One way of checking this assignment is to search for other band pairs containing these characteristic splittings. Scans to lower wavenumbers revealed no such pairings, and indeed no bands of significant intensity other than those due to BaO were found in the 16000-20000 cm^{-1} region. However, on the high wavenumber side at least one vibrational progression could be identified showing the 250 cm^{-1} splitting. For reasons discussed later, this has been labelled as a progression

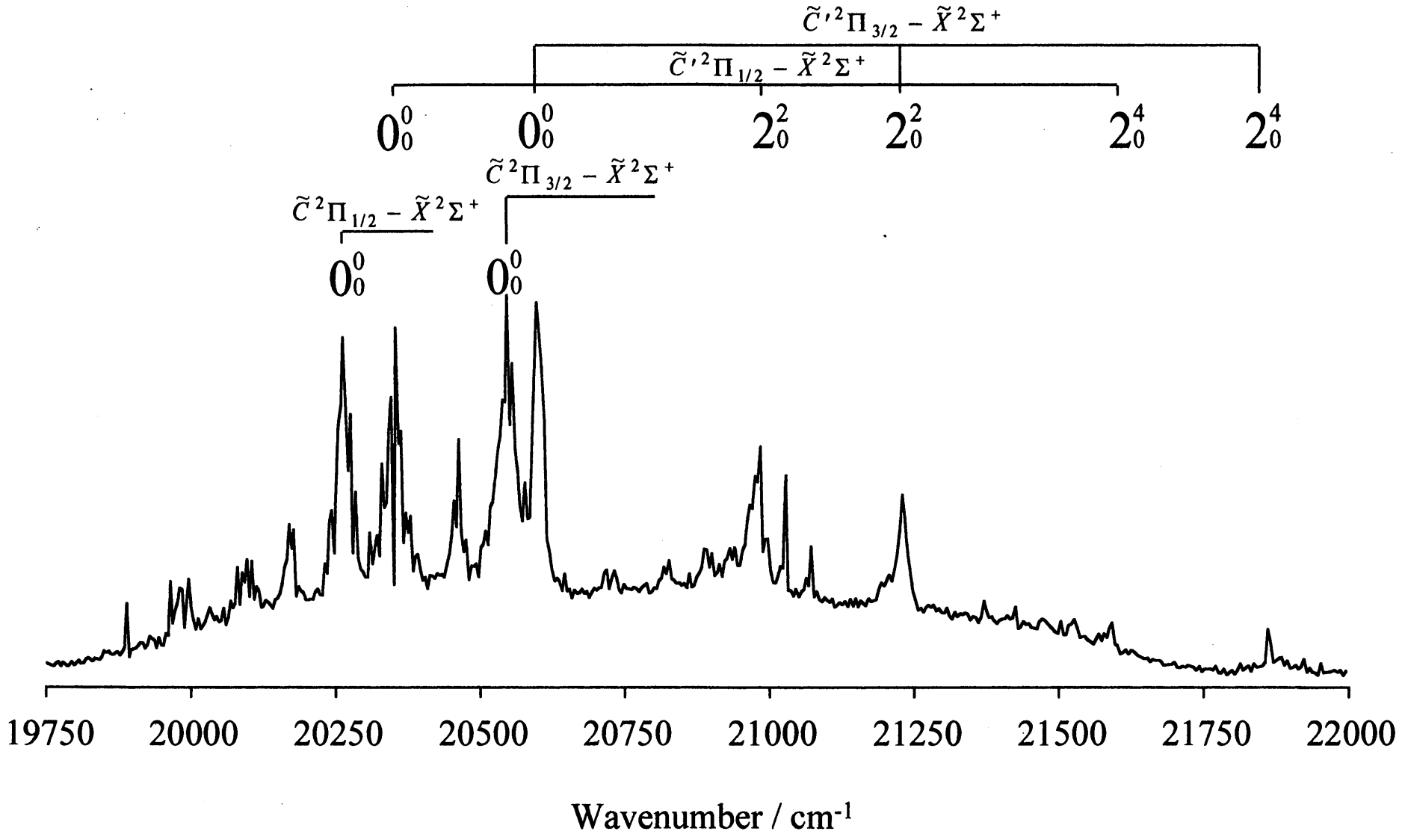

Figure 6.4 Excitation spectrum of the $'\tilde{C} - \tilde{X}'$ region of BaOH. This scan covers the full range of the Coumarin 480 laser dye, hence the variation in background intensity

in ν_3 in the $\widetilde{C}'^2\Pi - \widetilde{X}^2\Sigma^+$ system in Figure 6.4. There is also some evidence of a vibrational progression built upon the other pair of strong bands, namely the pair labelled as the $\widetilde{C}^2\Pi - \widetilde{X}^2\Sigma^+$ 0_0^0 transition. However these features, once again attributed to a progression in ν_3, are very weak and this must be viewed as a tentative assignment.

It is interesting at this point to compare the observations discussed here with those reported by other groups for this spectral region and with what would be expected from an analogy with BaF. Considering BaF first, a single observed excited state, the $C^2\Pi$ state, has been seen in the region under consideration. This state is well-isolated from the $B^2\Sigma^+$ and $D^2\Sigma^+$ states, as can be seen by inspecting Figure 6.3. The $C^2\Pi$ state has a T_e of 20091 cm^{-1} and a spin-orbit splitting constant of 195 cm^{-1} in the v=0 level.[7] Assuming that the analogy with BaOH is valid, it is difficult to reconcile this with the observations of the BaOH $\widetilde{C} - \widetilde{X}$ system by previous workers.[1-3] If there is only a single excited electronic state involved, the separation between the two prominent bands reported at 20534 cm^{-1} (487 nm) and 19531 cm^{-1} (512 nm) in emission spectra (and also seen in the LIF excitation spectrum of Haraguchi *et al.*[3]) must be due to either a vibrational interval or a spin-orbit splitting. If it is a spin-orbit splitting it would be dramatically different from that of the C$^2\Pi$ state of BaF. If it is a vibrational interval, it would be too large for the Ba-O stretch and the Ba-O-H bend, but far too low for the O-H stretch.

Although in this work a strong band near to 487 nm is observed, no trace of any band that might correspond to the 512 nm feature can been found in our excitation spectra, despite repeated attempts. Since we have already observed the strong $\widetilde{D} - \widetilde{X}$ system of BaOH under our experimental conditions, we are led to one of two conclusions: (i) the flame spectra contain one or more 'hot bands' of BaOH that are not seen in a supersonic jet, or (ii) that the bands reported by previous workers are not due to BaOH. Of these suggestions the first of these would seem more likely.

Comparison of the observations reported here with BaF is more favourable. The quartet of strong bands in the 20240-20620 cm^{-1} region are close to the BaF $C^2\Pi$-$X^2\Sigma^+$ origin. Furthermore, the two apparent spin-orbit splittings, although larger than

that in the BaF $C^2\Pi$ state, are not too dissimilar. This similarities are strong evidence that these bands are due to BaOH. However, there is clearly a problem with this assignment since there would appear to be *two* similar but distinct electronic transitions when comparison with BaF would lead us to expect only one. This apparent anomaly will be discussed in greater later in this chapter.

6.4.2 Vibrational structure

As mentioned above, a vibrational progression in the system labelled $\tilde{C}'^2\Pi - \tilde{X}^2\Sigma^+$ can be identified in Figure 6.4. The first member, consisting of the pair of bands at 20967 and 21225 cm^{-1}, are quite strong and correspond to an average vibrational interval of 615 cm^{-1}. This is most likely due to excitation of one quantum in the Ba-O stretching mode. If correct, the substantial increase in frequency over the Ba-O stretch in the ground electronic state of BaOH (495 cm^{-1})[5] implies a significant strengthening of the Ba-O bond on excitation to the $\tilde{C}'^2\Pi$ state. A further member of the $\tilde{C}'^2\Pi - \tilde{X}^2\Sigma^+$ ν_3 progression has been identified in Figure 6.4. Two weak bands, at 21585 and 21853 cm^{-1}, respectively, have the correct doublet splitting (268 cm^{-1}) and vibrational interval (average 623 cm^{-1}) to be feasible members of the ν_3 progression.

Vibrational structure in the $\tilde{C}^2\Pi - \tilde{X}^2\Sigma^+$ system is less prominent. A weak band at 20715 cm^{-1} may be the first member in a ν_3 progression associated with the $\tilde{C}^2\Pi_{1/2} - \tilde{X}^2\Sigma^+$ spin-orbit component, as identified in Figure 6.4. However, the other spin-orbit partner would lie under the much stronger $\tilde{C}'^2\Pi_{1/2} - \tilde{X}^2\Sigma^+$ 3_0^1 band and so this assignment cannot be confirmed. However, if correct, the excited state fundamental frequency obtained (445 cm^{-1}) is very close to that in the $C^2\Pi$ state of BaF (453 cm^{-1} from reference 9).

6.4.3 Rotational contour analysis

Rotational structure has not been fully resolved in the $\tilde{C} - \tilde{X}$ and $\tilde{C}' - \tilde{X}$ BaOH bands. However, the rotational contours of the four strongest bands, shown in Figure 6.5 (a), are revealing. The contour of each band shows four clear branches which are strongly reminiscent of the '+3*B*, +*B*, -*B*, -3*B*' structure seen in a $^2\Pi$-$^2\Sigma$ transition

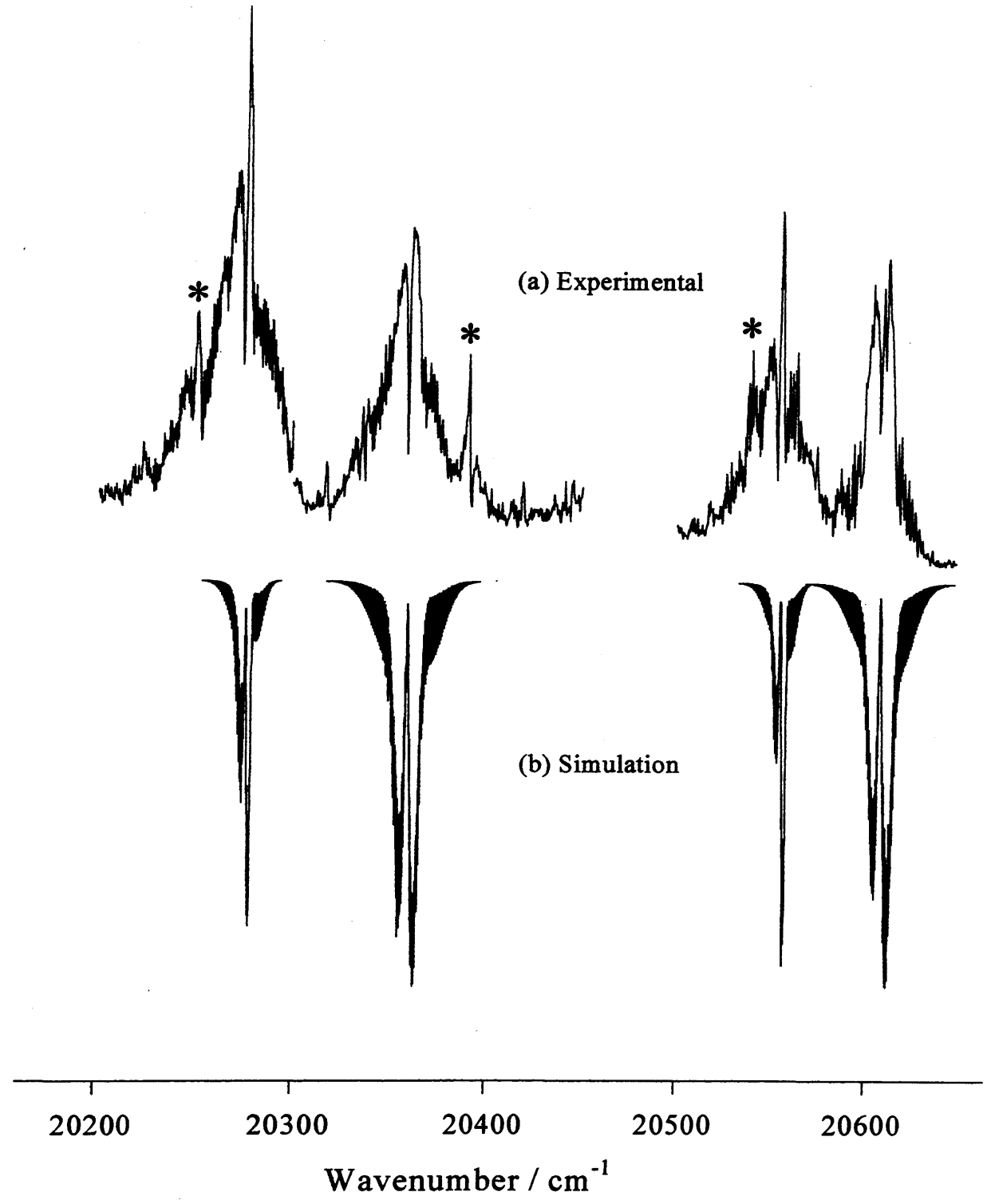

Figure 6.5 (a) Expanded view of the $\tilde{C} - \tilde{X}$ and $\tilde{C}' - \tilde{X}$ transitions. (b) Simulation assuming the constants shown in Table 6.1 and a rotational temperature of 50 K.

when the $^2\Pi$ state is close to the Hund's case (a) limit.[8] Indeed this precisely the situation seen in the high resolution spectra of ZnC_2H_5 described in chapter 5. The apparent spin-orbit splittings seen for these bands are more than large enough to satisfy the Hund's case (a) limit ($A>>BJ$) for the excited state and, since we expect a $^2\Pi$-$^2\Sigma^+$ transition by analogy with BaF, the rotational structure seems perfectly explicable.

Assuming $^2\Pi$-$^2\Sigma^+$ transitions, we have simulated the rotational structure in the two spin-orbit pairs and the result is shown in Figure 5(b). The program SpecSim, developed by Panov and Miller and containing models for $^2\Pi$ and $^2\Sigma$ states, was employed for the simulation. This program, described in more detail in Chapter 4, combines matrix diagonalisation of the appropriate rotational Hamiltonian with transition intensity calculations, non-linear least squares fitting, and plotting routines, all in a single standardised package. Given the low resolution of the present work, a least squares fit was not employed. Instead, the spin-orbit splitting and rotational constants in the excited electronic state, together with the temperature, were adjusted until reasonable visual agreement with experiment was obtained. Clearly, the general shape of the rotational contours is reproduced in the simulation. It is evident from the contours that there is no substantial change in rotational constant on electronic excitation since there is no significant shading of the bands to the red or blue. This is borne out by the rotational constants which, as can be seen on inspection of Table 6.1, are very similar to the ground state value. Once again, this is in line with BaF which shows only a small decrease in the rotational constant on C-X excitation.[9]

The rotational contour analysis above assumes that the BaOH molecule is linear in both the ground and $\tilde{C}^2\Pi$ states, but as will be seen later, the reverse polarisation nature of the equivalent state in the alkaline earth monohalides indicates that a bent configuration is feasible for the $\tilde{C}-\tilde{X}$ transition. If BaOH is bent upon excitaion, the molecular symmetry would be lowered from $C_{\infty v}$ to C_s making BaOH an asymmetric top molecule. The lowering of molecular symmetry would cause the doubly degenerate $C^2\Pi$ state in the linear molecule limit, to be split into an $^2A'$ and an $^2A''$ state when bent. As described in detail in Chapter 4 and 5 it is possible to observe a

Table 1. Molecular constants determined for BaOH compared to those for the analogous states in BaF. All values are in wavenumbers (cm^{-1}).

State	Molecular constants [b]	BaOH	BaF [c]
$\tilde{D}^2\Sigma^+$	B_0	0.255 ± 0.005	0.2273
Linear Model			
$\tilde{C}'^2\Pi$ [a]	B_0	0.216 ± 0.005	
	A	250 ± 3	
$\tilde{C}^2\Pi$ [a]	B_0	0.213 ± 0.005	0.2148
	A	279 ± 3	198.8
Asymmetric rotor Model			
$\tilde{C}'$ [a]	$B=C$		
	A		
	A^{SO}		
$\tilde{C}$ [a]	$B=C$		
	A		
	A^{SO}		
$\tilde{X}^2\Sigma^+$	B_0	0.216571(11) [d]	0.2158

(a) The assignments of these states are uncertain. See text for further details.
(b) B_0 is the rotational constant in the zero point vibrational level and A is the spin-orbit coupling constant.
(c) From references 7 and 11.
(d) From reference 5.

pseudo spin-orbit coupling caused by a large spin-rotation interaction (usually ε_{aa}) and if this occurs '+3*B*,+*B*,-*B*-3*B*' rotational structure would be expected.

As discussed in Chapter 5, the spin-rotation term is dominated by a second order term which couple two or more electronic states through molecular rotation. Equation 6.1 is taken from Chapter 5 and quantifies this second order interaction:[10]

$$\varepsilon_{aa}^{(2)} = \sum_{n\neq 0} \frac{4B_a \langle \psi_0 | \hat{\ell}_a | \psi_n \rangle \langle \psi_0 | \zeta_{4p} \hat{\ell}_a | \psi_n \rangle}{E_n^0 - E_n^0} \qquad (6.1)$$

where all the terms have the same definition as in Chapter 5.

From equation 6.1 and the theory discussed in Chapter 5, it can be seen that ε_{aa} will have a significantly greater magnitude than any of the other spin-rotation constants because:

(i) *A* will be much greater than *B* or *C* if, as suggested, the molecule is only slightly bent.

(ii) The two states that are though to interact strongly are the $^2A'$ and the $^2A''$ states. Like the corresponding excited states of ZnC_2H_5, these states can be thought of as metal-localised p_x and p_y orbitals. A rotation about the *z* axis will give the largest coupling. As the *a* inertial axis is nearly coincidental with the *z* axis the spin-rotation constant ε_{aa} will be significantly larger than ε_{bb} or ε_{cc}.

The rotational contour shown in Figure 6(b) was simulated assuming the that BaOH is bent in the excited state. The asymmetric top with spin-rotation (ASYMSR) model developed by the author (see Chapter 4) in conjunction with SpecSim was used to simulate the spectrum. As the model is designed to simulate transitions between $^2A'$ and/or $^2A''$ states in asymmetric top molecules, an approximate way of treating the linear $^2\Sigma$ ground state was needed. The linear $^2\Sigma$ state was described as an

asymmetric state with no spin rotation, The A rotational constant was made very large to approximate to infinity and B=C=0.2162 cm^{-1}.

Again the lack of spectral resolution did not make it appropriate to perform a linear least square fit to the experimental data. Instead the temperature, upper state rotational constants and ε_{aa} were varied until good visual agreement was observed. It was also not possible to determine whether the $\tilde{C}$ or the $\tilde{C}'$ state is the one with $^2A'$ symmetry.

An obvious question that arises is where are the expected K sub-bands if BaOH is bent in its excited state(s). K sub-bands are separated by a difference of ~$2\overline{A}$ (where $\overline{A} = ((A'' + A')/2)$. Since A'' is essentially infinite then only one K sub-band, the K'=1-K''=0, will be seen as only the K''=0 levelhas a signifficant population as $A'' \rightarrow \infty$. This make it impossible to determined A' directly from the spectrum but it is possible to obtain an approximate valueby using the spin rotation coupling constant, ε_{aa}', along with the energy separation of the two states, and equation 6.1. If we assume $\langle \psi_0 | \hat{\ell}_\alpha | \psi_n \rangle$ =1, and $\langle \psi_0 | \zeta_{4p} \hat{\ell}_\alpha | \psi_n \rangle$ = spin-orbit splitting of a theoretical linear molecule (the value used here is that of BaF) then A' can be calculated and are included in the table of rotational constant (Table 6.1).

In principle ε_{aa} should have the same magnitude, but oppersite signs for the $\tilde{C}$ and the $\tilde{C}'$ states. Our resolution is too low to determine the sign but the magnitudes are indeed similar, although they are not equal. This discrepancy could be due to:

(a) ε_{aa} is dependent upon A'.

(b) It has been assumed in this simplistic approach that the second-order spin-rotation interaction arises due to the interaction of just two electronic states, but in reality more electronic states or more likely, vibrational levels of the same electronic states contribute.[10] These contributions need not be the same for $\tilde{C}$ and $\tilde{C}'$ states.

6.4.4 BaOH $\tilde{C}$ state: linear or bent?

Finally, attention is turned to the surprising observation of two nearly isoenergetic excited electronic states (the separation is only 71 cm^{-1} measured from the mid-points of the spin-orbit components). The different spin-orbit splittings and the slight differences in rotational structure are consistent with two distinct $^2\Pi$-$^2\Sigma^+$ systems. We have labelled these as the $\tilde{C}^2\Pi - \tilde{X}^2\Sigma^+$ and $\tilde{C}'^2\Pi - \tilde{X}^2\Sigma^+$ transitions in the discussion above to distinguish between them. However, comparison with BaF leads us to expect only one $^2\Pi$-$^2\Sigma^+$ transition in this region. To try and find a possible explanation for this apparent discrepancy, the $C^2\Pi$ state of BaF must be considered in a little more detail.

In the two lowest optically accessible excited states of all the alkaline earth monohalides, the $A^2\Pi$ and $B^2\Sigma^+$ states, the unpaired electron is located primarily on the metal atom *but in orbitals polarised away from the halide*. These orbitals are essentially metal $np/(n\text{-}1)d$ hybrid orbitals.[11,12] In the $C^2\Pi$ state the unpaired electron is once again mainly metal-localised *but the hybrid orbitals are now polarised towards the halide*; this state is said to be reverse-polarised.[12,13] For the alkaline earth monohalides, this confers more electron density on the halide ion than is the case for the lower electronic states and leads to a strong variation in spin-orbit coupling constant as a function of the halide identity.[13]

In BaOH the reverse polarisation may have an additional effect. With the electron density in a π orbital pointing towards the OH group, there may be some tendency for the molecule to deviate from linearity. As shown in Figure 6, this would allow the hydrogen 1*s* orbital to overlap with one of the lobes of the metal-centred π orbital creating a bonding interaction. If correct, the resulting lower symmetry would resolve the reverse-polarised $^2\Pi$ state into two distinct electronic states, a $^2A'$ state and a $^2A''$ state.

The deviation from linearity, if it occurs, must be small for two reasons. First, since BaOH is known to be linear in its ground electronic state, we would have to observe a long progression in the Ba-O-H bending mode if there was a significant change in the equilibrium Ba-O-H angle. No such progression is observed. Second, the

observation of a large pseudo-spin-orbit splitting would be inconsistent with a strongly bent molecule. However, with a slight deviation from linearity the high speed of the nuclear rotation about the *a* inertial axis, which corresponds approximately to the Ba-O axis, results in a breakdown of the Born-Oppenheimer approximation. In essence, there is some coupling of the unpaired electron to the nuclear rotational motion about this axis generating, in effect, electronic orbital angular momentum.[10,15] This is only significant if the $^2A'$ and $^2A''$ states are close in energy *and* rotation about the *a* axis is fast (i.e. the *A* rotational constant is large). These criteria will be met for slightly bent BaOH and the resulting rotational structure, as seen earlier, would be indistinguishable from that of the linear molecule at the current spectral resolution.

6.5 Conclusion

Possibly the simplest explanation for the electronic states in the 22700-24400 cm^{-1} region, where only one is expected from analogy with BaF, is that BaOH is bent in these states. A bent geometry would cause the degeneracy of the $^2\Pi$ state to be resolvedinto two states, of $^2A'$ and $^2A''$ symmetry respectively. The '+3*B*, +*B*, -*B*, -3*B*' rotational structure observed in the spectra can be explained in terms of a large spin-rotation interaction about the *a* inertial axis. The hypothesis that BaOH is bent in these states is not unreasonable as they are expected to be reverse-polarised and this could confer a favourable interaction between the H atom and the unpaired electron if the molecule is bent.

6.5 References

1 C.G. James and T.M. Sugden, *Nature*, **175**, 133 (1955)

2 M. Charton and A.G. Gaydon, *Proc. Phys. Soc.* A, **7**, 520 (1956)

3 H. Haraguchi, S.J. Weeks and J.D. Winefordner, *Spectrochim. Acta A*, **35**, 391 (1979)

4 P.F.Bernath, Advances in Photochemistry, in press.

5 R. Pereiria and D.H. Levy, *J. Chem. Phy.*, **105**, 9733 (1996)

6 S. Kinsey-Nielson, C.R. Brazier and P.F. Bernath, *J. Chem. Phys.*, **84**, 698 (1986)

7 W.T.M.L. Fernando, M. Douay and P.F. Bernath, *J. Mol. Spec.*, **144**, 344 (1990)

8 Huber and G. Herzberg, *Spectra of Diatomic Molecules*, Van Nostrand, New York (1950)

9 A. Bernard, J. Verges and R.F. Barrow, *J. Mol. Spec.*, **152**, 174, (1992)

10 Z. Morbi, C. Zhao and P.F. Bernath, *J. Chem. Phys.*, **108**, 8891 (1997)

11 T. Torring, W. E. Ernst, and J. Kandler, *J. Chem. Phys.*, **90**, 4927 (1989)

12 S. F. Rice, H. Martin, and R. W. Field, *J. Chem. Phys.*, **82**, 5023 (1985)

13 P. Bungden, B. Engels, and S. D. Peyerimhoff, *J. Chem. Phys.*, **176**, 407 (1991)

14 N. A. Harris and R. W. Field, *J. Chem. Phys.*, **98**, 2642 (1993)

15 C. J. Whitham and Ch. Jungen, *J. Chem. Phys.*, **93** 1001 (1990)

Chapter Seven

Conclusion

7.1 Introduction

The aim of the work described within this thesis was to investigate some electronic states of some group 2 and group 12 metal-containing free radicals. The two groups generally give rise to molecules with similar electronic structures since both metals possess an s^2 valence shell electronic configuration. The particular states studied are the ground and first two excited states of ZnC_2H_5 and the $\widetilde{C}$ and $\widetilde{D}^2\Sigma^+$ states of BaOH.

At first glance these molecules may appear not to be very closely related, although as stated above the electronic structure of both is similar, with the electronic transitions to low lying states being expected to be metal localised in both cases. However, in addition to this the author has shown there may be evidence of a bent structure for BaOH in the $\widetilde{C}$ excited state giving this molecule nominally the same symmetry C_s as ZnC_2H_5. Consequently, BaOH in its $\widetilde{C}$ electronic state may join ZnC_2H_5 by being an asymmetric rotor containing an unpaired electron. There is some evidence that, like Zn_2H_5, BaOH has a large second order spin-rotation interaction which manifests itself in the $\widetilde{C}-\widetilde{X}$ spectrum.

All of the electronic states detailed above have been studied using LIF spectroscopy at both vibrational and rotational resolution giving, to varying degrees. In addition, where appropriate *ab initio* calculations coupled to isotope shift data and spectral simulations have been performed to aid assignment.

7.2 SpecSim

The simulations of rotational structure in the LIF spectra were performed using the SpecSim package developed by the laser spectroscopy group at Ohio State University.[1] A new asymmetric top model which included spin-rotation was developed to simulate rotational structure in the spectra of ZnC_2H_5. This also turned out to be useful in simulating the rotational structure in the $\widetilde{C}-\widetilde{X}$ spectrum of BaOH. The new model, called ASYMSR, was initially tested on $CaNH_2$ and CaSH, two asymmetric free readicals with published high resolution LIF spectra which have been

fully assigned. These tests were successful and demonstrated that the new model is error free.

7.3 ZnC_2H_5

The starting point for the studies of ZnC_2H_5 was the LIF work of Povey *et al.*[2] In that earlier work the first LIF excitation spectrum of ZnC_2H_5 was reported in the 22500-24000 cm^{-1} range. However, due to its complexity, *Povey et al.* were unable to confidently assign any of the features. A more detailed study was carried out in the present work. In particular, the following three studies were performed:

i) A LIF dispersed fluorescence spectroscopic study.
ii) Analysis of rotationally-resolved LIF spectra recorded by Terry Miller's group at the Ohio State University.
iii) A combined *ab initio*/high resolution study of the zinc isotope splitting.

The aim of the first and third investigation was primarily to gain vibrational information, while in the second an explanation of the rotational structure was the goal.

7.3.1 Vibrational structure

The dispersed fluorescence spectra recorded in the present work have allowed vibrational frequencies of several modes in the ZnC_2H_5 ground electronic state to be obtained for the first time, especially the Zn-C stretch and the Zn-C-H bend (ν_{10} and ν_{11}). In addition, this data has made it possible to make assignments, some firm and others tentative, of several bands in the excitation spectrum. Once again these have been assigned mainly to transitions involving ν_{10} and ν_{11}.

The isotopic shift data added weight to the assignments made in the dispersed fluorescence study, but in addition it was useful in assigning features arising from the methyl torsional vibration, ν_{18}. Table 5.1 summarises the vibrational assignments made.

7.3.2 Rotational structure

Although a full rotational analysis was not performed, the preliminary analysis carried out provides valuable information. A good estimate of the rotational constants have been ascertained for the ground electronic state and for various excited vibronic levels. A detailed discussion of the magnitude of the second-order spin-rotation was also given. Studies of band C, which has been assigned as 2 quanta in the methyl torsion (ν_{18}), showed unexpected splitting which has tentatively been assigned to a methyl tunnelling splitting.

7.3.3 Future work

Although this work greatly adds to the knowledge of the ground and low lying states of ZnC_2H_5, there is potential for further work. An LIF study using ZnC_2D_5 might prove interesting, although it is debatable that it would provide any helpful new information since greater congestion at both the rotational and vibrational level of resolution would be expected. The area which would benefit greatly from an further work are rotationally-resolved studies studies. The spectral congestion caused by the three main zinc isotopes made assignment difficult in the present work. Potentially, rotationally-resolved spectra of the bands described within this thesis could also be obtained using resonance-enhanced multiphoton ionisation (REMPI) spectroscopy. With the opportunity for mass selection this presents, it could be possible to record the spectrum of a single isotopomer.

Another area that may be of interest is further investigation of the unusual splittings observed in Band C, possibly through extending the ASYMSR model to include a effects caused by the methyl torsion.

7.4 BaOH

Several previous spectroscopic studies of BaOH[3-5] have concentrated on the 18500 – 21000 cm^{-1} region and have mainly been flame studies. They have shown broad structure that has been tentatively assigned to a $\tilde{C}-\tilde{X}$ electronic transition. However, the low resolution of previous studies coupled to the high temperature conditions made detailed interpretation of these spectra impossible. This prompted the jet cooled LIF study reported in this thesis.

Two excited electronic states of BaOH were studied in this work. The $\widetilde{D}^2\Sigma^+$ state was observed for the first time and it proved possible to extract both vibrational and rotational information from the $\widetilde{D}^2\Sigma^+ - \widetilde{X}^2\Sigma^+$ LIF spectrum.

More interesting was the $\widetilde{C} - \widetilde{X}$ region. Previous studies of the isoelectronic molecule BaF indicated that there is only one electronic transition in this region. However, the spectra in this work showed structure that could not easily be explained in terms of a single excited electronic state. The spectra appeared to arise from two similar but distinct electronic states which is at odds with analogy with BaF.

The author has suggested that that this apparent anomaly could due to a tendency for BaOH to become non-linear upon excitation. Analogy with alkaline earth monohalides indicates the $\widetilde{C}$ state is reversed polarised, that is the electron density is polarised towards the ligand. If the molecule is bent then the reverse polarised orbital may interact with the $1s$ orbital of the hydrogen atom, possibly giving rise to a lower energy configuration. This would resolve the nominally degenerate $^2\Pi$ state at the linear configuration into two states of $^2A'$ and $^2A''$ symmetry, respectively. These states are expected to be close in energy and, as for ZnC_2H_5, interaction between them via a large spin-rotation effect is likely.

In order to substantiate this suggestion rotational contour analysis was performed on the origin peaks of both electronic states assuming a bent configuration in the excited state. The ASYMSR rotation model and SpecSim were used to simulate the spectra and good visual agreement was achieved.

The other plausible explanation for the complication seen the '$\widetilde{C} - \widetilde{X}$' region is that the BaOH is linear in the states in this region which are two $^2\Pi$ states. This would not fit with analogy with BaF but was investigated. The observed rotational structure was simulated and good visual agreement could be achieved assuming both transitions are $^2\Pi$-$^2\Sigma^+$ transitions.

7.4.1 Future work

The rotational structure observed in this work was not fully resolved. A fully rotationally-resolved study would make it possible to establish beyond any doubt the acctual symmetries of excited electronic states in the $\widetilde{C}-\widetilde{X}$ region.

7.5 References

1 S.I. Panov, *Ph.D. thesis,* Ohio State University (1997)

2 I.M. Povey, A.J. Bezant, G.K. corlett, and A.M. Ellis, *J. Phys. Chem.*, **98**, 10427 (1997)

3 C.G. James and T.M. Sugden, *Nature*, **175**, 133 (1955)

4 M. Charton and A.G. Gaydon, *Proc. Phys. Soc.* A, **7**, 520 (1956)

5 H. Haraguchi, S.J. Weeks and J.D. Winefordner, *Spectrochim. Acta A*, **35**, 391 (1979)